MINISTRY OF EDUCATION

TECHNICAL UNIVERSITY
OF CLUJ-NAPOCA, ROMANIA

FACULTY OF ELECTRICAL ENGINEERING

PhD THESIS

High-Frequency Modelling of Rotating Electrical Machines

PhD Student:
José Enrique Ruiz-Sarrió

PhD Supervisor:
Prof. Dr. Eng. Claudia Steluţa Marţiş

Examination committee:

<u>Chair:</u> Prof. Dr. Eng. **Teodor Pană**, PhD – Technical University of Cluj-Napoca, Romania

<u>PhD Supervisor:</u> Prof. Dr. Eng. **Claudia Steluţa Marţiş**, PhD – Technical University of Cluj-Napoca, Romania

Members:

Prof. Eng. **Jose A. Antonino-Daviu**, PhD – Universidad Politécnica de Valencia, Spain

Prof. Eng. **Elena Lomonova**, PhD – Eindhoven University of Technology The Netherlands

Prof. Eng. **Lorand Szabo**, PhD – Technical University of Cluj-Napoca Romania

– Cluj-Napoca –
2022

.

ACKNOWLEDGMENTS

Special acknowledgement to my partner Mevr. Kirsten Van Elsen. Thank you for standing my good and bad moments all over this PhD journey. "*Dank u voor uw onvoorwaardelijke steun, Ik hou van jou*". Every journey has an end point and yet, the initial point will always determine wether you will reach the goal or not. A person must never forget her or his roots if success is pursued. Special thanks to my dear father and mother, Enrique Ruiz and Eva María Sarrió who are the major contributors to the success of my many professional and personal journeys.

This dissertation is dedicated to:

The scientists that fought the Covid-19 pandemy in the first line under extreme pressure and stress conditions.

TABLE OF CONTENTS

5

6

ABBREVIATIONS

ACC   Air Conditioning Compressor
BEV   Battery Electric Vehicle
CE   Conducted Emission
CISPR   Comité International Spécial des Perturbations Radioélectriques
CM   Common-mode
DM   Differential-mode
DP   Distributed Parameter
DSP   Doubly Salient Pole
DUT   Device Under Test
EDM   Electric Discharge Machining
EMC   Electromagnetic Compatibility
EMD   Electrical Machines and Drives
EMI   Electromagnetic Interference
EU   European Union
FEM   Finite Element Method
ICE   Internal Combustion Engine
IGBT   Insulated Gate Bipolar Transistors
IM   Induction Machine
LISN   Line Impedance Stabilization Network
LP   Lumped Parameter
MTL   Multi-conductor Transmission Line
PCB   Printed Circuit Board
PEV   Plug-in Electric Vehicle
PM   Permanent Magnet
PMSM   Permanent Magnet Synchronous Machine
PS   Power Steering
PWM   Pulse Width Modulation
RE   Radiated Emission
RF   Radio Frequency
SPICE   Simulation Program with Integrated Circuit Emphasis
TEM   Transverse Electromagnetic
TL   Transmission Line

1. Introduction

1.1.   Research context

A European Green Deal for the European Union (EU) and its citizens was released at the end of 2019 [1]. It poses the commitment to tackle climate and environmental-related challenges during the next years. One of the main challenges is associated to the amount of greenhouse gas emissions. Transportation accounts for a 25% of the EU's emissions and still growing. Thus, a solution for the transportation sector is needed to reduce this emission up to 90% by the end of 2050 as stated in the abovementioned European document. The road transportation sector embodies the largest contribution to the emissions of the ground mobility [2]. Even after the latest technological advances in the automotive industry towards a more electrified vehicle, the emission objectives are far from being achieved.

Some contradictions are still present around electrification of vehicles [3]. However, the capabilities towards the CO_2 neutrality that this technology brings are evident and well proven. Electric motor drives are inherently more efficient in powering vehicles than Internal Combustion Engines (ICEs). These engines typically convert 15%-30% of the primary energy while electric motors can reach efficiencies of around 90%. In addition, electrification enables the usage of electricity from renewable sources such as eolic and photovoltaic generation [4].

Electrification in the automotive sector is known since the XIX century, when steam powered cars required a large water deposit and long start-up times. Even with the emergence of ICEs powered by gasoline, a cranck was needed to start the engine while electric motors had an inmediate start. With the popularization of the cars during the early 1900s, electric traction enjoyed some success during the 1920s [5]. The long-distance journeys, the emergence of the electric starter and the mass production techniques, lead to the fall of the electric powered vehicle in favor of the ICE. During the last 30 years, electrified systems started to become popular in the classical ICE cars since most mechanisms could be enhanced this way. This is the case of power steering, antilock-breaking or active suspension systems [6]. Hybrid vehicles started to be produced in the late 90s offering a more efficient

and clean traction possibility. From there on, a wide variety of alternatives have been developed for the vehicle traction such as Fuel-Cell Electric Vehicles (FCEVs) and Battery Electric Vehicles (BEVs) [7]. Nowadays the sales of Plug-in Electric Vehicles (PEVs) (i.e., vehicles with rechargeable battery packs that can be charged from the electric grid), are increasing globally. *Fig. 1-1* shows the monthly and year-to-year growth of light duty PEVs. Despite of COVID-19 crisis, which had a huge impact in the global world economy it is possible to appreciate that from a year-to-year perspective the growth is outstanding, reaching a 239% increase during April 2021. This growth is expected to increase even more during the coming years [8].
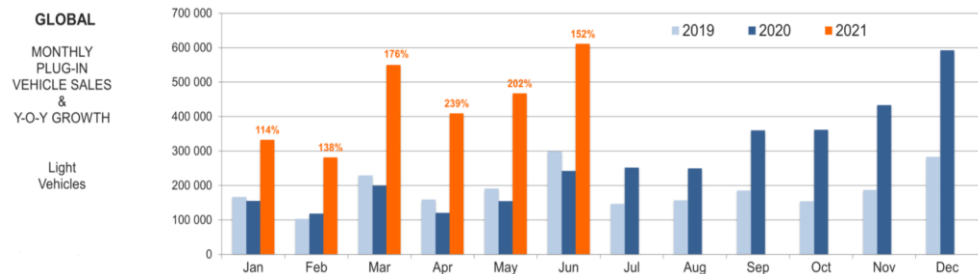
Fig. 1-1-Monthly and year-to-year PEVs global sales, 2021 *[8]*

The trend towards a more electrified vehicle and the increased demand of electric traction asks for a new generation of automotive electrical actuation, enabling a more efficient and environmentally friendly mobility. The INTERACT (European Industrial Doctorate on Next Generation for sustaINable auTomotive ElectRical ACtuaTion) project represents an example of EU funded research programm aiming to tackle the research & development of automotive electrical machines and drives. This dissertation is enclosed inside INTERACT and it is intended to tackle Electromagnetic Interference (EMI) and high-frequency phenomena of rotating electrical machines used in automotive applications.

1.2. Rotating electrical machines and drives fundamentals

This subsection is aimed to describe the basic principles of operation of rotating electrical machines from a system-level perspective. Electric energy stored in batteries or extracted from the

grid must be transformed into controlled mechanical traction to power a vehicle. This is achieved by using electrical machines together with modern power electronics and controllers. *Fig. 1-2* shows a general architecture utilized in BEVs [9]. The set formed by the power converter and the electric motor is the hardware core of the electrical actuation. These elements together with the control method and signal acquisition sensors are the main actors of the Electrical Machines and Drives (EMDs) engineering field.
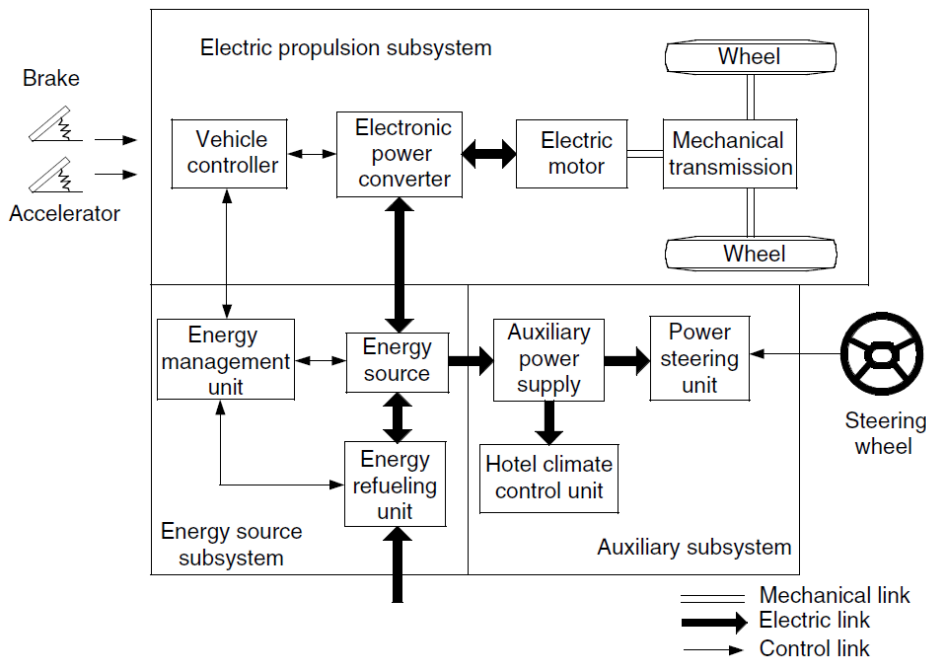
Fig. 1-2 - BEV conceptual architecture *[9]*

The working principle behind AC motor drives is to control the frequency and the amplitude of the electric signals feeding the motor to achieve controlled torque and speed. The controller is the algorithm defining the objective signals based on user defined inputs and sensor data. The electronic power converter is the hardware executing the controller output and the motor is the device in charge of the electromechanical conversion. *Fig. 1-3* describes a typical motor drive configuration in a three-phase system.

13
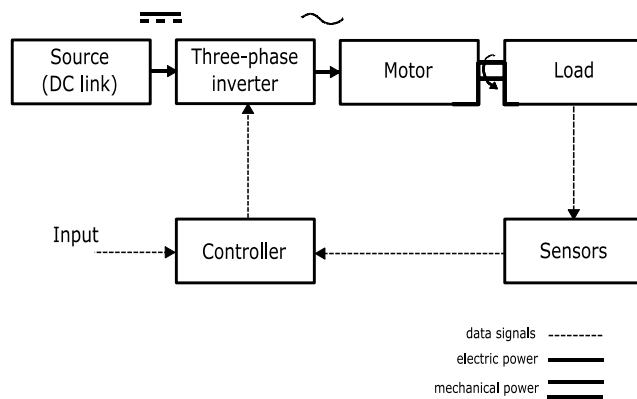
Fig. 1-3 - EMD configuration example for a three-phase system

The electrical power link between the inverter and the motor is of great interest for the aim of this dissertation. The input for the inverter is the DC link voltage level provided by a DC power source or a rectifier module, and the controller output. The objective is to control the amplitude and the frequency of the AC motor input voltage by using controllable semiconductor switches. A standard three-phase inverter is composed by three legs and six power modules. A power module is defined as a one-way switch with an antiparallel diode. *Fig. 1-4* shows the equivalent circuit of a three-phase inverter coupled with a star-connected motor. The switch typology depends on a wide number of
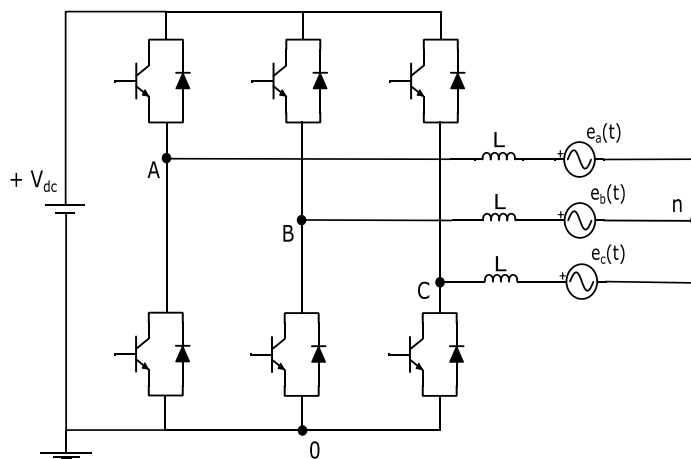
Fig. 1-4 - Three-phase voltage source inveter coupled to motor equivalent circuit

14

factors such as the switching frequency and the power capabilities. Some of the most used types are Metal-Oxide-Semiconductor Field Effect Transistors (MOSFETs) and Insulated Gate Bipolar Transistors (IGBTs) [10].
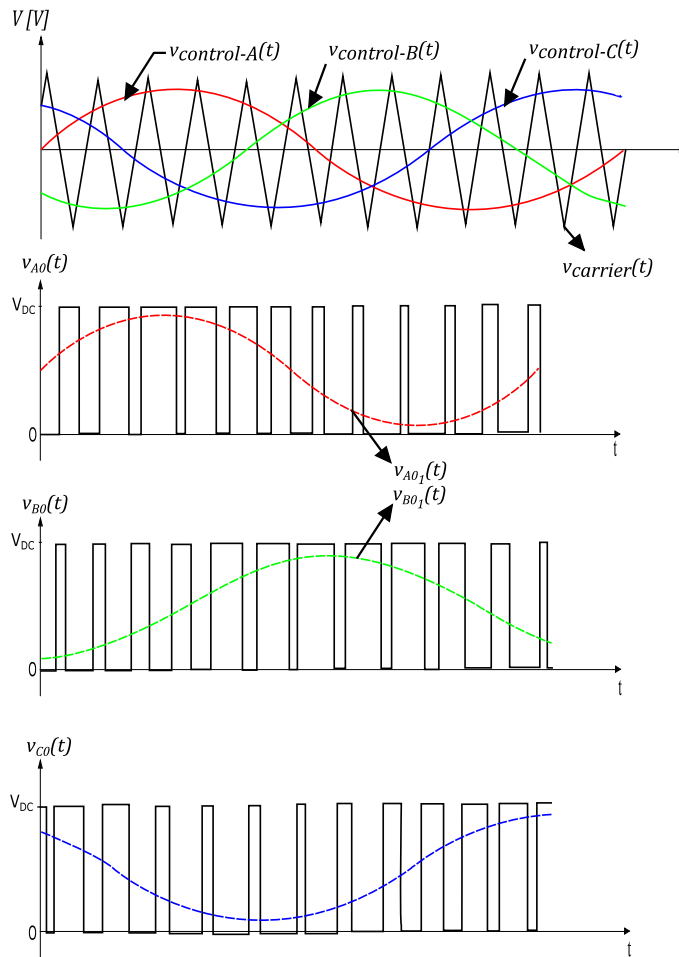
Fig. 1-5 - PWM technique for a three-phase voltage source inverter working in the linear region

A widespread technique to operate the inverter is the Pulse Width Modullation (PWM), where a control signal is intersected with a carrier signal to define the switch state (i.e., conducting or blocking current). The transistors are controlled by feeding their gates with a small amplitude signal. The antiparallel diodes conduct the inductive current flowing back during the off state. *Fig. 1-5* shows the working

15

principle of a three-phase voltage source inverter using PWM, where $v_{control}\,(t)$ represents the output signals from the control algorithm, $v_{carrier}\,(t)$ is the carrier signal, and $v_{A0}\,(t)$, $v_{B0}\,(t)$ and $v_{C0}\,(t)$ are the phase-to-ground voltages.

The pulsed voltage signals feed the electrical machine which transforms electrical into mechanical power. Rotating electrical machines are formed by a fixed part known as stator, and a moving part denoted as rotor. The stator core is composed by magnetically permeable steel formed by a large number of thin laminations with insulation material between them. Copper conductors are generally wound around the core forming the stator winding, which carries the current creating the stator magnetic field [11]. The rotor is composed by a laminated core and windings, Permanent Magnets (PMs) or both, creating a different magnetic field. The operating principle is based on the interaction between the magnetic fields and the currents flowing in the windings of the machine. The rotor can also be PM-less or winding-less for some types of rotating electrical machines (e.g., switched reluctance and pure synchronous reluctance machine).
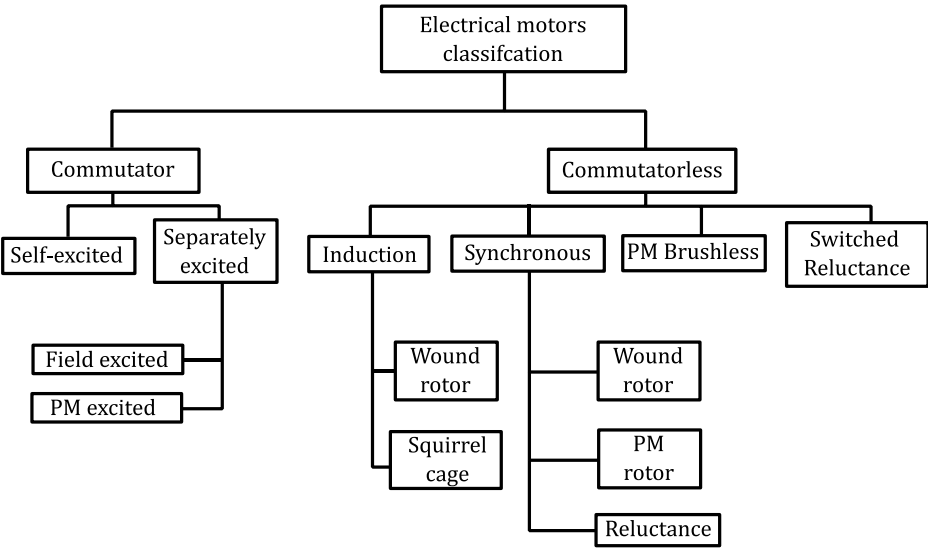
Fig. 1-6 - Rotating electrical machines general classification *[7]*

16

Electrical machines can be classified according to several constructional and operational characteristics. *Fig. 1-6* shows a basic classification of the main types of rotating electrical machines [7]. Some of the most important types of rotating machines are described below:

- *DC machines (with commutator):* They are based on the contribution of two different windings, a rotational or armature winding and a stationary field winding. The drawback of such a machine lays on the commutator and the brushes used to feed the rotating field. They need regular maintenance making the operation of the drive more expensive than other types of machines. However, the control is easy to implement, and it offers a reliable and fast speed and torque control.

- *Induction or asynchronous motor:* It is a wide-spread motor in many industrial applications. The rotor has embedded conductive bars or a winding. It rotates at a speed Ω_r while the stator magnetic flux rotates at an agular speed Ω_s. The relative difference between stator and rotor speeds is called slip. Induction machines are robust and reliable, but they present less efficiency than synchronous machines at the same ratings and low power factor at light load conditions.

- *Separately excited synchonous machines:* The rotor of this machine posess a DC separately excited winding, which rotates synchronously with the sator magnetic field. They are normally used for high power applications.

- *Permanent Magnet Synchronous Machines (PMSMs):* The main difference compared with separately excited synchronous machine is that the rotor field is non-controllable and originated within the magnets embedded in the rotor. Because of the low losses inherent of this type of machines it is normally used for high power density applications. However, the rare earth magnets are expensive, brittle, and they can be demagnetized during operation. *Fig. 1-7* shows an exploded view of a Permanent Magnet Synchronous Machine [12].

- *Synchronous Reluctance Machine (SyRM):* The principle of operation for this type of machine is based on the inductance differences between the two axes of the rotating reference frame (i.e., direct and quadrature axis). It is the simplest of the synchronous type since no field in the rotor is required. The main drawbacks are related to its lower power factor and efficiency when compared with PMSMs.

17

- *Switched Reluctance Machines (SRM):* The torque is also produced by reluctance difference with no field in the rotor. It is formed by salient poles with concentrated windings and the principle of operation differs from the synchronous reluctance type. High torque ripple, and noise and vibrations issues are the main drawbacks of this machine type.
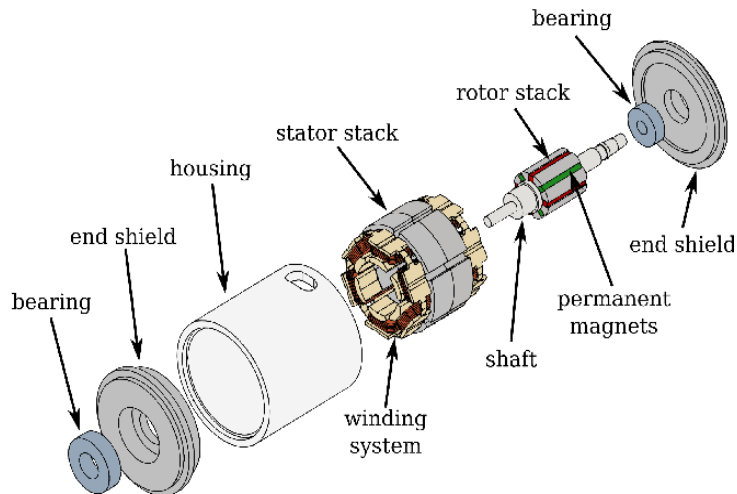
Fig. 1-7 – Exploded view of a PMSM *[12]*

1.3. High-frequency phenomena in EMDs

Electrical machinery has always suffered from signals oscillating at high frequencies, typically occurring for transient scenarios. Switching overvoltages caused by circuit breakers or protection sytems have been a field of study over many years for high-voltage applications [13]. With the development of semiconductor technology, power electronics converters started to become popular around the 80s decade. The development of such devices led to an increase of operation switching frequencies and voltage gradients (dv/dt), which is translated into an improvement in efficiency and power quality [10]. However, many secondary issues derived form this improvement turned into primary concerns when designing converters and electrical machinery [14]. Three main undesired phenomena derived from the

switched excitation of rotating electrical machines can be found in literature: over-voltages in the machine terminals, leackage and bearing currents, and EMI. They are closely related between them since they are due to the interaction of the high-frequency signal spectrum and the different impedance responses of the elements within the EMD system. This section analyzes the high-frequency signal sources and their main consequences.

1.3.1. High-frequency source

High switching frequencies, voltage (dv/dt) and current gradients (di/dt) during the transistor commutation action, are the major causes of high frequency phenomena on variable frequency drives. This can be analytically deduced from a series of periodic trapezoidal waveforms, which can represent an oscillator clock signal, a string of data signals or the pulsed voltage resulting from PWM

(a)

(b)
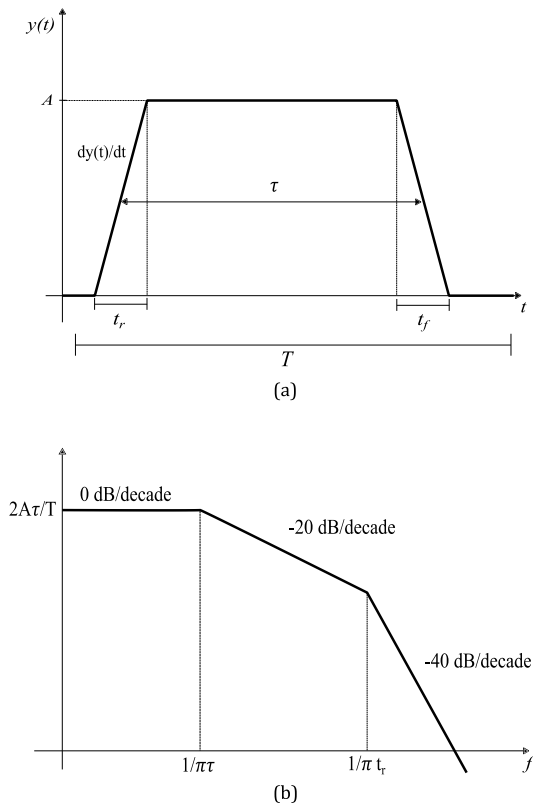
Fig. 1-8 - (a) Symetrical trapezoidal signal, (b) Symetrical trapezoidal signal spectral bounds

19

operation. Real switches are characterized by a trapezoidal voltage signal during the switching action with rise (t_r) and fall times (t_f), where their slopes contribute to the high frequency spectra of the signal. *Fig. 1-8* shows a symmetric trapezoidal waveform and its spectral bounds. The cut-off frequency for -40dB/dec attenuation is located at higher frequencies for reduced rise and fall times. The analytical Fourier decomposition for a symmetrical trapezoidal signal provides the spectral bounds or envelope defined by [15]:

$$20 \log_{10}(envelope)$$
$$= 20 \log_{10}\left(2A\frac{\tau}{T}\right) + 20 \log_{10}\left|\frac{\sin(\pi\tau f)}{\pi\tau f}\right| \qquad \textbf{(1-1)}$$
$$+ 20 \log_{10}\left|\frac{\sin(\pi t_r f)}{\pi t_r f}\right|$$

where A is the amplitude of the trapezoidal signal, τ is the time when the transistor is on conducting state, T is the switching period and f represents the frequency axis. Analytical expressions and their frequency envelopes for real case voltage spectra when unsymmetrical trapezoids and sinusoidal modulation are applied can be found in [16].

1.3.2. Machine terminal over-voltages

This effect was reported during the early 90s when IGBTs became popular in commercial applications [17]. Critical over-voltages take place when long cables are used between the converter and the machine. A mismatch between the cable and motor impedances causes
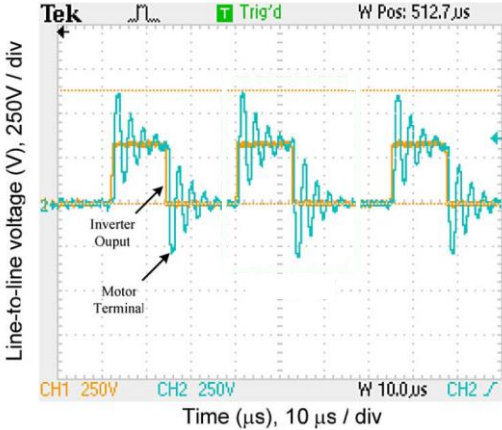
Fig. 1-9- Measured voltage waveforms for an inverter-motor setup with a 100m cable *[20]*

the voltage waves to be partially reflected back to the cable. If a new incident wave starts travelling along the cable when the reflected wave is not yet damped, the overshoot in the load (i.e., the motor) terminals increase [18]. Values higher than twice the bus voltage were reported in [19]. *Fig. 1-9* shows an oscilloscope measurement placed in the inverter output and the motor terminal voltages for a 100 m cable between inverter and motor [20]. The continued operation under this circumstance can lead to the electrical breakdown of the cables and the stator winding insulation if the partial discharge inception voltage of the insulation is overcome.

1.3.3. Leakage and bearing currents

Bearing currents due to magnetic asymmetries in line-operated machines are known for decades [21]. Since power converters started to be utilized, converter-induced leakage and bearing currents became the main object of study. These currents flow as a consequence of the Common-mode (CM) voltage or zero-sequence voltage of the inverter, which is not negligible due to the switching action. In three-phase systems the CM voltage can be defined as [10]:

$$v_{CM}(t) = \frac{v_{A0}(t) + v_{B0}(t) + v_{C0}(t)}{3}$$

(1-2)
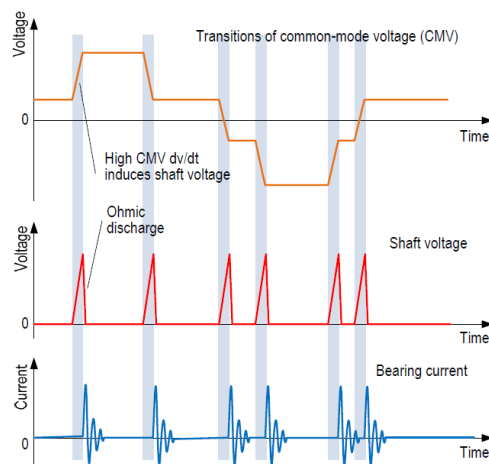
Fig. 1-10 – Relationship between CM voltage, shaft voltage and bearing currents *[23]*

where $v_{A0}(t), v_{B0}(t), v_{C0}(t)$ are the instantaneous value of the three-phase to ground voltages in the inverter. The CM voltage with high voltage gradients interacts with the parasitic capacitances inside the machine [22]. *Fig. 1-10* shows the CM voltage waveform and its effect on the bearing currents and shaft voltage [23].
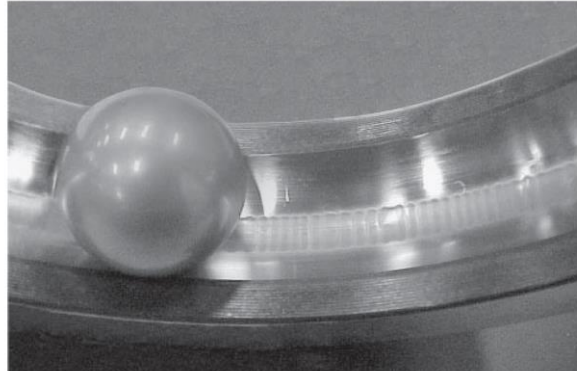
Fig. 1-11 – Bearing race with fluting patterns *[22]*

Currents flowing towards ground during normal operation are known as leakage currents and they do not necessary flow through the machine bearings. Bearing currents can cause machine failure since current flowing through them can damage their inner and outer races in the shape of corrugated patterns known as pitting and fluting [22], [24]. *Fig. 1-11* shows a bearing race with fluting derived from converter-induced bearing currents.

According to Müetze [25], four different types of converter-induced bearing currents can be distinguished. Two of them depend directly on the voltage across the bearing while the remaining two depend on the CM voltage and the current flowing through the parasitic capacitance between the machine winding and the frame. Fig. *1-12* shows a schematic describing the different types of bearing currents. Capacitive bearing currents flow through the bearing capacitance, which is built when the lubricating film completely insulates the races and the balls. This event only take place at high speed and low temperatures of operation. It is considered as not harmful since it has small amplitude. Electrostatic discharge currents are created when the

22

lubrication film´s discharge voltage threshold is surpassed. It discharges causing Electric Discharge Machining (EDM) pulses. These currents are particularly harmful since they can achieve high peak amplitudes. Circulating bearing currents are caused by a voltage difference along the shaft known as shaft voltage. This voltage difference is created by the ground current flowing circularly in the stator iron, which is uneven in the axial direction. If the shaft voltage overcomes the lubricating film withstand capabilities, a circulating bearing current will flow in the loop "stator frame - nondrived end - shaft - drived end" [24]. *Fig. 1-13* shows the principle of the circulating bearing currents mechanism. Rotor ground currents only occur if the motor is grounded via the driven load.
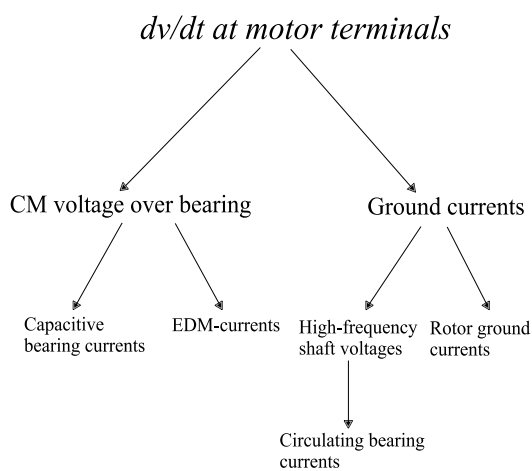
Fig. 1-12- Bearing current classification *[23]*
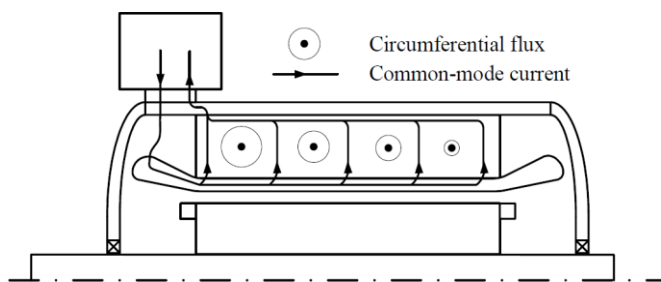
Fig. 1-13 – Shaft voltage origination principle *[24]*

23

1.3.4. Electromagnetic Interference (EMI)

EMI is defined as an unwanted electrical signal that produces undesirable effects in an electrical system such as communication errors, disturbed performance, or malfunction [25]. Electromagnetic Compatibility (EMC) is defined as the engineering field addressing the generation, transmission, and reception of these unwanted electrical signals (i.e., electromagnetic energy). Regulations imposed by EMC standards ensure a device´s ability to operate as intended in its shared operating environment also accounting for any other equipment within the same space. There exist two types of EMC requirements for electric systems [26]:

- *Those mandated by governmental agencies:* These are strict legal requirements that cannot be avoided. They are aimed to reduce the product emisisons and they do not guarantee that the product will not cause any interference. However, they are intended to control the so called „electromagnetic pollution". For a product to be sold in a country, it must comply with these regulations. Examples of governmental agencies regulating EMC are the Federal Communications Commision (FCC) operating in the United States of America, or the Comité International Spécial des Perturbations Radioélectriques (CISPR), which is part of the International Electrotechnical Comission (IEC).
- *Those imposed by the product manufacturer:* These are intended to fullfil the customer satisfaction and to maintain a good reputation in the marketplace. As an example, automotive Original Equipment Manufacturers (OEMs) will need certain emission levels for complying with the vehicle standards. They will ask the electrical equipment suppliers to comply with these emission levels before signing the supply agreements.

Two types of emissions are normally regulated by EMC regulations. Conducted Emissions (CEs) are those transmitted out of the product power cord. The frequency range of such emissions spans from 150 kHz to 30 MHz [15]. Radiated Emissions (REs) exist in the shape of electromagnetic waves that unintentionally propagate away from the

device´s structure. In this case, the frequency spans the gap between 30MHz and 1GHz. These two types are the main subject of measurement to ensure the compliance with EMC regulations.
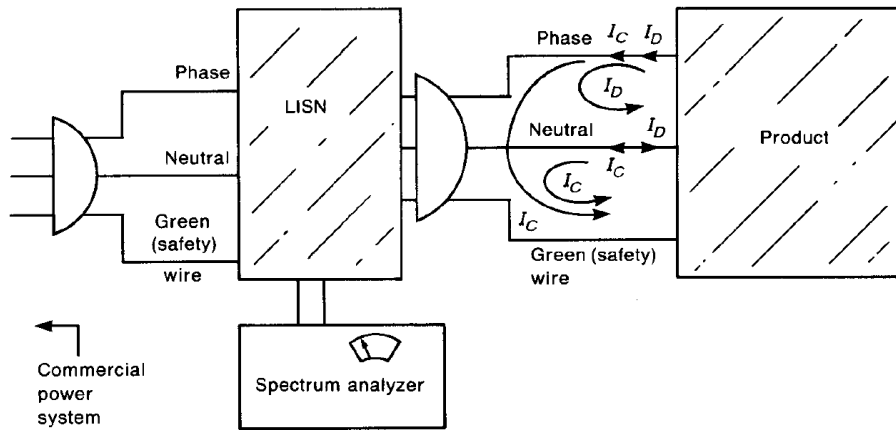
Fig. 1-14 - CEs generic test setup *[26]*

The generic measurement setup for CEs is depicted in *Fig. 1-14* [26]. The Line Impedance Stabilization Network (LISN) is the device used to keep a constant reference impedance over the frequency range of the CEs test. A spectrum analyzer is attached to the constant impedance of the LISN to measure the emissions of the product. Depending on the application, different limits and positioning of the test elements are utilized. As an example, CISPR25 standard assess electromagnetic emissions measurement for on-board equipment in vehicles as well as boats powered by ICEs and devices also powered by ICEs. *Fig. 1-15* shows the CEs test layout for on-board alternators and generators from CISPR25 [27]. The emission limits are tabulated in tables (e.g., frequency over amplitude limits in dB) and graphs in the standards.

For the REs similar principles are used with the difference that in this case, antennas are used to capture the propagating electromagnetic waves. They are normally associated to the CEs, since the radiated energy is derived from the current flowing in the power cords. The assessment of this type of emissions is out of the scope of

25

this dissertation.

1. Load (battery and resistor)
2. Artificial mains network
3. Measuring equipment
4. Equiptment Under Test (EUT)
5. Ground plane
6. Test harness (power leads 200 mm maximum length)
7. Coaxial cable (50 ohm)
8. Indicator lamp/control resistor (where applicable)
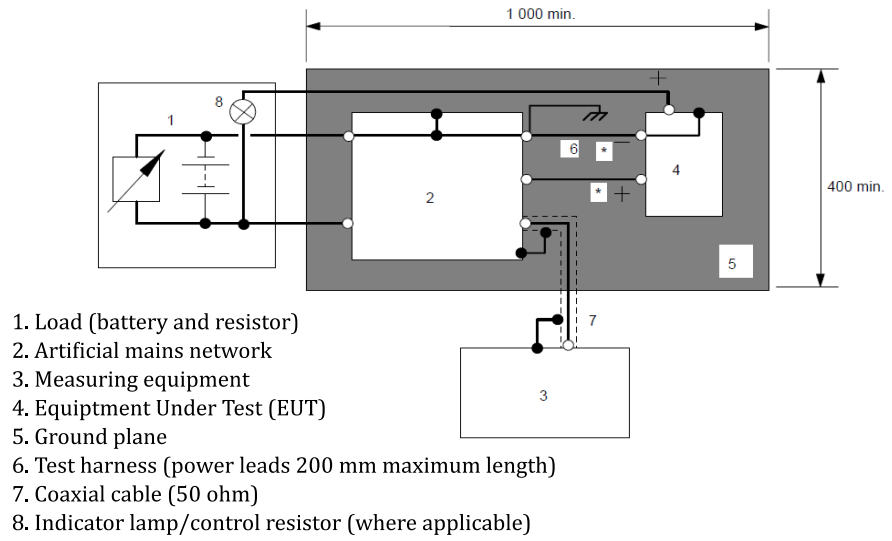
Fig. 1-15 - CISPR25, CEs layout for on-board alternators and generators *[27]*

Rotating electrical machines are subjected to EMC testing. The power converter feeds the machine through cables, plates or directly using Printed Circuit Boards (PCBs). The switching of the transistors will cause a rich harmonic spectrum in the range of the CEs and REs that will propagate along the cables, plates, PCBs, and the rotating electrical machine. These high-frequency components will propagate in two different modes know as CM and Differential-mode (DM). *Fig. 1-16* describes the current mode decomposition for a three-wire system, where cable three acts as a return conductor (equivalent to the circuit shown in *Fig. 1-14)*. The relationships between total and modal currents is given by [15]:

$$\begin{cases} I_1 = I_C + I_D \\ I_2 = I_C - I_D \end{cases} \rightarrow \begin{cases} I_C = \dfrac{I_1 - I_2}{2} \\ I_D = \dfrac{I_1 + I_2}{2} \end{cases} \tag{1-3}$$

where I_C and I_D represent the CM and DM currents respectively and I_1 and I_2 are the total currents of the system in the input ports. In three-phase EMDs the modal currents are distributed as shown in *Fig. 1-17.* The CM is referred to the electric signals flowing in the same direction

26

in a pair of lines (or three in case of three-phase systems) while the DM refers to signals flowing in opposite directions.
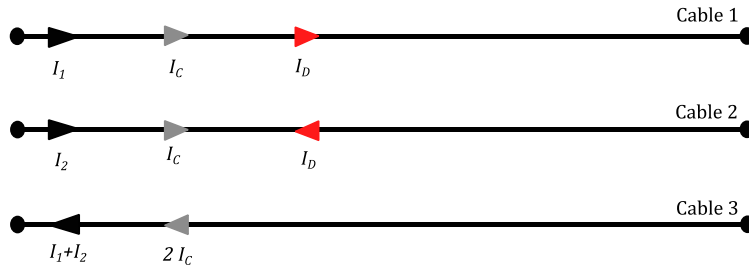
Fig. 1-16 - Modal decomposition of currents on a three cables system, where cable 3 is the return conductor
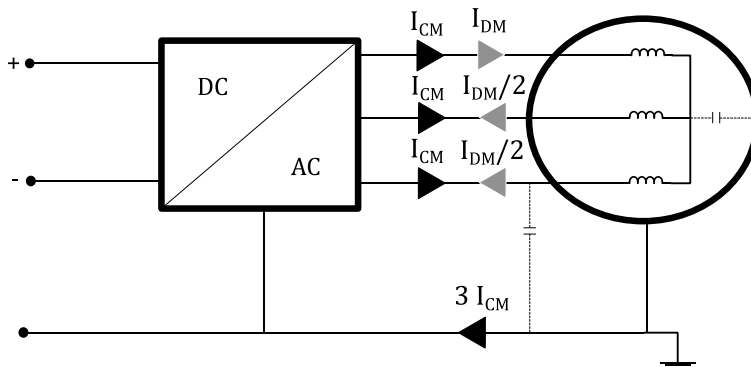
Fig. 1-17- Three-phase machine drive modal currents distribution

1.3.5. High-frequency phenomena prediction

Electrical machines can suffer from failure and malfunction due to high-frequency harmonics present in the input signal spectrum. The prediction of such phenomena is generally tackled at a system level including cables, filters, power electronics and machine models [29]. Some works are focused on the modelling of EMI in EMDs in the frequency domain [30], [31], [32], [33]. On the other hand, some modelling approaches in the literature are oriented towards machine terminal overvoltage, winding voltage distribution [34], [20], and

27

leakage and bearing currents [25], [26] prediction in the time domain. *Fig. 1-18* shows a schematic where all elements forming the system-level simulation are included [34]. The high-frequency modelling of power electronics modules and cabling is not discussed in the present dissertation.

The rotating electrical machine model plays a key role on this prediction since it is one of the main sources of failure [30]. In addition, it represents a path for CM and DM components that can jeopardize EMC compliance in CEs and REs tests [15]. Thus, the design of the rotating electrical machine is directly involved with high-frequency phenomena and their prediction should be tackled as soon as possible in the design process to avoid expensive design iterations in advanced phases.
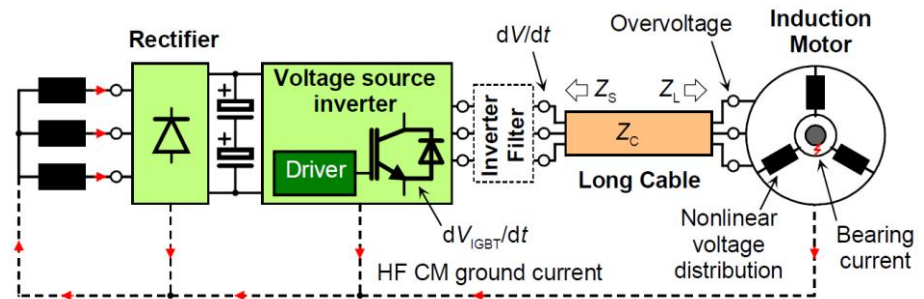
Fig. 1-18 - Inverter-cable-motor set for system-level high-frequency phenomena prediction *[34]*

1.4.　　Thesis objectives and contributions

The objective of the present dissertation is to study the high-frequency response of rotating electrical machines. The study of the physical phenomenom is initially tackled by performing a comprehensive analysis of different modelling methodologies and trends. The main core of the thesis focusses on developing and validating a deterministic modelling method that provides an estimation of the machine impedances in a high-frequency band (i.e., from tenths of kHz to thenths of MHz depending on the objective). This prediction is aimed to favor an EMI-aware design of the rotating machine at early stages when a physical prototype is not yet available.

The developed modelling method is implemented and validated for two different PMSMs utilized in the automotive industry. These two machines are selected taking into account the INTERACT project boundaries and partners.

The work presented in this dissertation gave rise to some original contributions shared in peer reviewed international conferences and journals. These research documents are already published or in process of publication. Further information about published material is provided in the section 'List of publications'. The most important contributions developed in this dissertation are:

- The development and validation of a high-frequency impedance model oriented towards early prediction for PMSMs

- The detailed experimental investigation of the effect of PMSM rotor and housing on the high-frequency impedance response

- The detailed experimental investigation of the rotor DC field effect on the high-frequency impedance response in PMSMs

- A thorough numerical investigation of the effect of the machine configuration, geometry and material characteristics on the high-frequency impedance response.

1.5.   Dissertation outline

This dissertation is organized in four main parts. The first block reviews the different methodologies for high-frequency phenomena prediction focusing on the rotating machine model. The second block presents a deterministic modelling method aimed to forecast high-frequency machine impedance. This second block includes the detailed description of all the numerical methods and input data required and presents the main simulation results. The third part embodies the experimental section of the dissertation, where the main measurement principles and investigations are discussed. The fourth block presents a sensitivity analysis of the model inputs. This study is aimed to demonstrate the main utility of the developed modelling method and to quantify the model uncertainties. Finally, the main conclusions of the

research developed in this dissertation are presented and discussed. The chapters of the thesis are organzided in the following manner:

Chapter 1 introduces the topic and provides the framework for the research. The main objectives and outline are also defined in this chapter.

Chapter 2 presents a comprehensive analysis of different modelling methodologies for high-frequency phenomena emphasizing on the role of the rotating electrical machine. In addition, the necessity of further investigation on rotating machine models is justified.

Chapter 3 develops an original deterministic modelling method to forecast the high-frequency impedance in PMSMs. This chapter analyzes the input data in detail, poses the initial assumptions and considerations, discusses the utilized numerical methods and procedures, and presents the main results. Two different PMSMs are utilized as case study samples to implement the modelling method; results for both of them are provided.

Chapter 4 is aimed to experimentally validate the developed modelling approach and to experimentally investigate the contribution of some constructional and configurational features of the studied PMSMs. Particularly, the effect of rotor and housing insertion, and the effect of the rotor position on the high-frequency impedance curves are experimentally studied. The simulation and experimental results are compared for both case study PMSMs.

Chapter 5 presents a sensitivity analysis for different model inputs. The study is separated into three parts. The first one deals with the variation of the so-called primary parameters, which are defined as the basic passive circuit elements (i.e., resistances, capacitances, inductances). The second part studies the effect of variation of the machine geometry parameters, while the third part is focused on the type of stator winding connection. The last section analyses the effect of different material properties.

Chapter 6 poses the main conclusions of the dissertation and highlights future work directions on the topic.

2. High-frequency modelling methods for rotating electrical machines

High-frequency induced machine failure and EMI have been the object of study for many researchers over the last decades. The prediction of such phenomena is intended to provide engineers with insights that allow the design of better filtering devices, better machines and, in definitive, to bring a better product to the market. The chapter is organized in four main parts. The first block provides an overview of early modelling methods for electrical machines and the context for the the model categorization. The second part analyses the test-based models, which at the same time can be split into two different trends: behavioural models and physics-based circuits. The third part studies the numerical approach, which includes an overview of the most important methods followed by a detailed analysis of parameter extraction methodologies and modelling nuances of relevant works. Finally, an overview of the research topic and the perspective for developing new modelling methods are provided.

The first high-frequency electrical machine models were aimed to predict the voltage distribution caused by surge phenomena in large electrical machinery [34] [35], [36]. With the appearance of fast and more efficient variable frequency drives, high-frequency phenomena required a broader perspective and new predictive models arose. The work of Chen [37] during the middle 90s addressed issues such as bearing currents and EMI under different switching operations. Consoli et al. [38] developed a predictive model for an induction motor drive based on Park transform in 1996, and Grandi et al. [39] presented a modelling approach based on induction motor impedance measurement and lumped parameter circuits, in 1997. At the same time, Boglietti et al. [40] developed a different machine model also based in lumped parameter circuits, in 1999. *Fig. 2-1* shows the three machine models described in [38] , [39] and [40]. Other remarkable works during the same period were developed by the former Allen-Bradley company (nowadays Rockwell Automation) engineers such as Skibinski, Kerkman, Schlegel and Erdman [17], [25], [41], [42], [43]. They dealt with every high-frequency issue related to power converter operation in EMDs (i.e., EMI issues, leakage and bearing currents, and machine terminal overvoltage). During the last years of the 90s, Ran et

al. presented a collection of two articles dealing with time and frequency domain models for EMI prediction of the full induction motor drive set [44], [45]. All these models included motor representations based on measured impedance data. Suresh et al. [46] introduced one of the first numerical approaches for estimating induction motor voltage distribution in the stator winding by using the Finite Element Method (FEM), in 1999. From the 2000s on, a larger number of modelling methods and representations appeared.
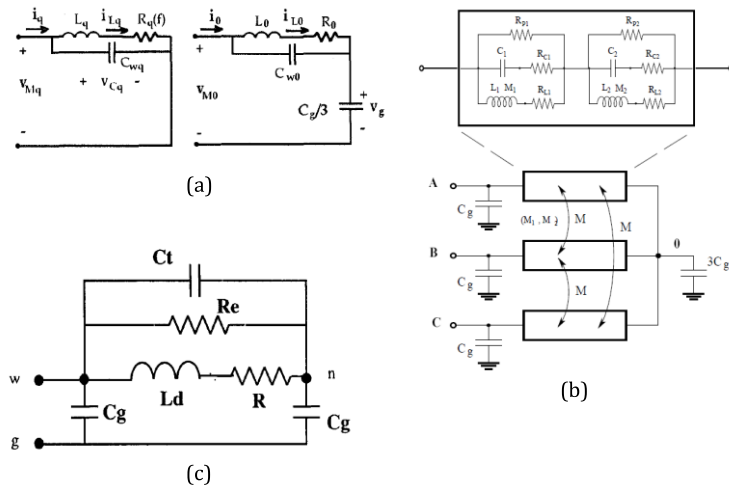
Fig. 2-1- Early lumped parameter high-frequency rotating electrical machine models described in (a) *[38]*, (b) *[39]*, (c) *[40]*

The rotating electrical machine models developed during the last two decades are very diverse regarding their parametrization and construction. According to their parametrization, two main groups can be differenciated through the analysis of literature, test-based and numerical models. The former aims to exploit the broadband impedance measurement to experimentally tune a lumped equivalent circuit that matches the measured response. The later type utilizes numerical methods such as the FEM, to estimate the equivalent circuit parameters. Both types of models are oriented to address the simulation of EMI, voltage distribution within machine windings, machine terminal overvoltages or leakage and/or bearing currents.

2.1. Test-based models

Test-based models have been thoroughly studied by many researchers over the last years becoming the most popular way to model the high-frequency phenomena. The common procedure consists of measuring two impedances (CM and DM) by using an impedance analyzer or a LCR meter. From the impedance measurement, the circuit parameters can be extracted by using different strategies. Depending on the physical meaning of the utilized equivalent circuits, two types of test-based models can be identified. The first are black-box or behavioural models with no correlation with the physical phenomena. The second method emulates the physical behaviour of the motor by utilizing equivalent lumped circuits where their parameters attempt to represent the physical reality of the phenomena.

2.1.1. Behavioral models

Behavioral models are based on impedance fitting using different techniques. In [52] simple RLC circuits with no physical meaning were used to map the measured impedance response, where two different methods are introduced to represent the measured data. The first one is based on the observation of the motor impedance trends (i.e., frequency bands where the impedance has inductive, capacitive or resistive behaviour) and the latter utilizes analytical expressions to fit the response over the considered frequency band. In [53] and [54] the authors utilized the vector fitting technique [55], [51], [52] to map the CM and DM impedances of the motor, and circuit synthesis to estimate and implement the lumped parameter circuit elements in a circuit simulator. A similar approach is found in [56], where impedance and admittance representations were utilized instead of passive circuits. In [57] a multistage RLC lumped parameter circuit was utilized, with a stage for each resonance point. The accuracy of these methods is very high with a reduced computational cost. The major drawback of behavioral models lays on the lack of physical meaning and on the need of measurement equipment and physical prototypes.
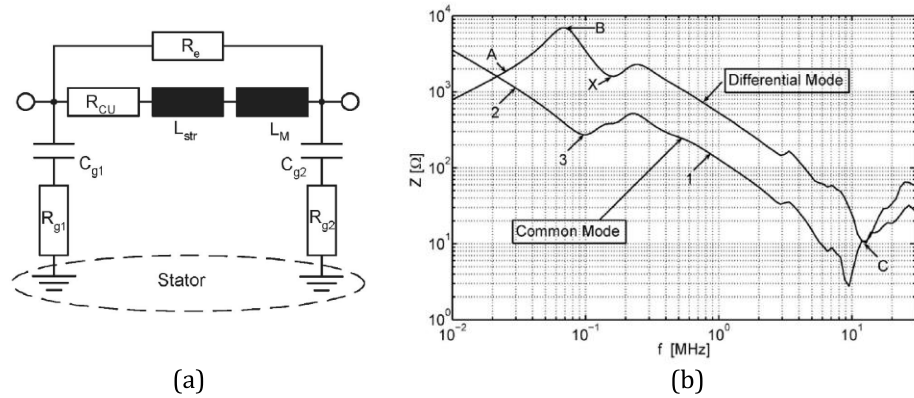
33

(a)   (b)

Fig. 2-2- (a) Per-phase equivalent circuit and (b) impedance measurement results identifying resonant points *[55]*

2.1.2. **Physical circuits**

The parametrization of the lumped parameter circuits utilizes simpler methods in terms of algorithm complexity than the behavioral models but, on the other hand, it can be more computationally expensive depending on the number of circuit elements. A common approach to obtain the circuit parameters is to identify the resonant frequencies of the measured impedance response and to compute the RLC parameters of the circuit using these frequency points. *Fig. 2-2* shows the equivalent per-phase circuit and the measured impedance curves in [58], where R_{cu} represents the conductor's resistance, R_e the eddy currents losses, L_{str} the stray inductances, L_M the inductive coupling of the phase including mutual inductances, C_g the phase-to-ground capacitance, and R_g is the resistance of the leackage current path. From the resonant points and dominant slopes (A, B, C, X and 1,2,3) the different circuit parameters are obtained.

The circuit proposed in [59] and [60] added additional parasitic elements to the classic T equivalent circuit of an induction machine to map the measured impedance. In [61] the same type of circuit was used for a PMSM. These three works utilized measured data in combination with some analytical expressions to compute the lumped circuit elements. In [62] a lumped parameter circuit was parametrized utilizing a genetic algoritm and experimental data. Vidmar et al. [63] presented a per-phase lumped parameter circuit considering different

34

machine connections. Similarly, an induction machine model taking into account different connections was proposed in [64], where the parameters of the circuit were modified depending on the winding connection. In [65] simple circuits were proposed to map the impedance response, where simplicity is claimed as main contribution. The model presented in [66] utilizes simple per-phase belt winding models to successfully map CM and DM impedances up to more than 10 MHz. In [67] the CM impedance was targeted by isolating the paths of the current flowing towards ground, where time domain results are obtained from the measured CM impedance and validated experimentally. Ryu et al. [69] utilized per-unit-length parameters to map the input impedance of a machine winding. The novel contributions of this work lay on the utilization of a vector network analyzer to obtain the frequency characteristics and the consideration of transmission line principles to estimate the equivalent circuit architecture. Further interesting contributions utilizing physical circuits can be found in [68], and [70].

The utilization of equivalent circuits derived from the physical phenomena occurring at high frequencies is extensively present in the literature. Regarding system-level simulation they represent one of the simpler ways to represent the machine behaviour. However, a machine prototype and measurement equipment are necessary to parameterize them and thus, their applicability is not feasible in pre-prototyping stages of EMDs design.

2.2. Numerical models

The numerical parametrization can overcome the limitations from test-based models since no machine prototype is, a priori, needed. A common procedure to build a numerical model is to build an equivalent circuit with several RLC components and to estimate their value by using analytical formulae and/or solving electromagnetic partial differential equations on a discrete space (e.g., electromagnetic FEM solvers). Once the circuit is built and parametrized, Kirchhoff laws are solved to obtain the different outputs of the model. This is normally performed by using a Simulation Program with Integrated Circuit Emphasis (SPICE) or custom scripts solving the circuit nodal equations. The main challenge of the numerical methods is the limited accuracy

and the computational effort required to estimate the circuit parameters.

The equivalent circuit can be shaped in different ways. The most common method is to use Distributed Parameter (DP) equivalent circuits, which are defined as simplified circuits from multiconductor Transmission Line (TL) expressions. Some authors utilize simplification methods to reduce the circuits to a Lumped Parameter (LP) version, which utilizes a reduced number of passive elements in the equivalent circuit. These circuits can represent single slot conductors, turns or machine phases. However, if accuracy of the model is targeted, inter-turn terms must be considered.

TABLE 2-I provides an overview of the most relevant numerical models for rotating electrical machines found in the literature. The studied publications are listed in chronological order. In first place, the type of equivalent circuit (i.e., TL, DP, or LP) is analyzed. The model parameters can be obtained by using FEM or analytical formulae. The FEM is commonly acknowledged to provide an increased degree of accuracy compared with the analytical approach. Thus, the difference between analytical extraction of the different RLC parameters is also anlyzed in the table, differencianting between capacitances and frequency-dependent parameters (i.e., resistances and inductances). The frequency-dependent nature of the resistive and inductive parameters is also analyzed in the table. Then, the domain of the model is indicated. Time-domain models are normally oriented towards the study of overvoltages and voltage distribution in machine windings, while frequency domain models are more suitable for EMI prediction. The presence or absence of experimental validation is also analyzed in the table. The last aspect is related to the applicability to real machine samples. Some modelling approaches were implemented and validated for few turns on a stator structure or for single coils.

The numerical parameter estimation is separately analyzed by some authors without including any machine model. The solely computation of parasitic capacitances attracted increased research attention due to their utility on predicting shaft voltages and bearing currents. In [87] and [88] the FEM computation of capacitances at a

36

TABLE 2-I – Numerical modelling approaches overview

| Publication	Year	Circuit type	L & R extraction	C extraction	Freq. dependency?	Domain	Experimental validation?	Real machine?
[68]	2004	LP	✗	Analytical	✗	time & freq.	✗	✓(DSP)
[69]	2005	DP	FEM	FEM	✗	time	✓	✓(PMSM)
[70]	2005	TL/LP	FEM	FEM	✓	time & freq.	✓	✓(IM)
[71]	2006	LP	FEM	FEM	✗	time	✗	✓(PMSM)
[72]	2008	TL	Analytical	FEM	✓	freq.	✓	✓(IM)
[73]	2009	DP	FEM	FEM	✓	freq.	✓	✓(PMSM)
[74]	2010	TL	FEM	FEM	✓	freq.	✗	✓(PMSM)
[75]	2010	LP	FEM	FEM	✗	time	✓	✓(PMSM)
[76]	2011	DP	Analytical	Analytical	✗	freq.	✓	✓(DC)
[77]	2011	DP	Analytical	FEM	✗	time	✓	✗
[78]	2012	DP	FEM	FEM	✓	freq.	✓	✗
[79]	2013	DP	FEM	FEM	✗	time	✗	✗
[80]	2015	LP	FEM	FEM	✓	freq.	✓	✓(IM)
[81]	2016	DP	FEM	FEM	✗	freq.	✓	✗
[82]	2016	LP	Analytical	FEM	✗	time & freq.	✓	✓(SPSM)
[83]	2016	DP	FEM	FEM	✗	time & freq.	✓	✗
[84]	2019	DP	FEM	FEM	✗	time	✓	✗
[85]	2019	DP	Analytical	FEM	✗	time	✓	✗
[86]	2020	LP	FEM	FEM	✓	freq.	✓	✓(PMSM)

<div align="center">(a)   (b)</div>
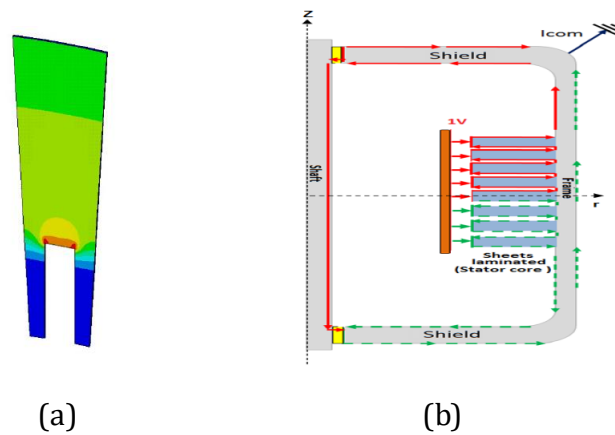
Fig. 2-3 - (a) CM current distribution on a single lamination *[103]*, (b) CM current path *[102]*

machine scale including experimental validation is presented. The computation of bearing capacitances oriented towards bearing voltage and current prediction can be found in [89] and [90]. The capacitance between the active parts and the stator frame is closely analyzed in [91] and [92] by using FEM. The study of the end-winding capacitances is presented in [93] and [94]. In [95] a comparison among different methods including analytical formulae for inter-turn capacitances is provided. In [99] analytical expressions to compute inter-turn and turn-to-ground capacitances are provided together with experimental validation. Works also including the computation of R and L parameters can be found in [97], [98]. The computation of end-winding frequency-dependent RL parameters is closely analyzed in [99].

Works aimed to predict circulating bearing currents and shaft voltages analyze the impedance and the propagation path of the CM current and the creation of the CM flux. It is the case of the work of Maki-Ontto [26], who defined the analytical expressions for the determination of the CM flux (e.g., see Fig. 1-13). Extended formulation for this phenomenom considering radial cooling ducts and teeth was provided in [100]. The same problem was analyzed by using FEM in [101], [102], and [103], where the propagation of the CM current causing the CM flux is studied in detail. Magdun et al. [103] focuses on obtaining an expression for the iron core impedance, while Boucenna et

al. [102] explores the CM current paths towards ground. *Fig. 2-3* exemplifies the CM current propagation causing circulating bearing currents.

Further discussion on the available rotating machine numerical modelling methods is provided in the following lines. Emphasis is placed around the computation of frequency-dependent resistances and inductances. In [73] a 3D model was built to take into account eddy currents within single laminations with arbitrary iron permeability, which was proven to affect the inductive and resistive parameters. The main contribution of this work lays on the effect of eddy currents flowing within single laminations on the inductance and resistance of single conductors. Mihaila et al. [77] developed a full machine model to predict inter-turn voltage spikes with a SPICE simulated circuit, where only the capacitive couplings were precisely computed by using the FEM. In [78] a simplified coil was modelled and validated, which considers skin and proximity effects in single conductors where the iron core was modelled in 2D assuming that flux do not penetrate the core at high frequencies. In [104] a 3D model was developed focusing on the magnetodynamic solver for resistance and inductance computation, but no experimental validation was provided. In [80] both CM and DM impedances of a full induction machine were modelled including frequency dependent permeability, which allows to account for high-frequency eddy currents within single laminations at a reduced computational cost. Measured data was utilized to estimate the eddy-current associated losses which adjusts the damping of the simulated curves. Boucenna et al. [81] developed a model for CM impedance prediction, where dielectric loss was accounted by performing an experimental tuning. This model was tested and validated on a simplified stator sample with few conductors per slot. Radja et al. [84] focused on the usage of FEM to predict the transient voltage distribution in machine windings. The method considers skin and proximity effects in single conductors but no data about the influence of laminated iron cores was found. In [85] voltage stress and current distribution prediction in individual conductors by utilizing FEM methods was targeted. Randomness of the conductor distribution was studied, and the model was fully validated on a simplified stator sample. End-winding sections and laminated iron core behavior were neglected in this work. The work presented in [105] describes a simplified method to predict machine terminal over-voltages by utilizing a 2D

39

FEM approach, with no experimental validation. Ryu et al. [106] developed a method for induction machine CM impedance estimation at pre-prototyping design stages including the study of the variation of some slot design parameters. Results about the extraction of the different multiconductor transmission line parameters were not presented and discussed in this work.

2.3. High-frequency modelling perspective

This section is conceived to provide the general overview on the research topic and to further frame the presented research in this dissertation. High-frequency models for electrical machines are formed by a circuit containing several passive elements, connected to resemble the machine winding and constructive parts, and parameterized by using measured data or numerical methods (i.e., analytical formulae or FEM). The equivalent circuit is solved node-by-node to obtain an output response, that can vary depending on the aim of the model. For time-domain models, the output can be the voltage transient on a determined machine turn, the leakage current flowing through a bearing or the terminal overvoltage signal. Frequency-domain models provide the impedance (amplitude and phase) over frequency within a determined frequency band that can vary depending on the model objective. These models are aimed to predict EMI or to predict the general distribution of the current paths in the different propagation modes (i.e., CM and DM).

The parametrization of the model is defined by the availability of physical prototypes and measurement equipment. Thus, in pre-prototyping design stages the numerical approach is the only available methodology. The prediction of high-frequency phenomena at early development phases is an asset for every machine manufacturer that pursues an EMI-aware design and to forecast potential machine failure modes.

The complex physical phenomena in high-frequency operation, makes the numerical approach challenging in terms of computational cost and accuracy. Through the analyzed literature, some critical points while modelling high-frequency phenomena have been identified:

- Skin and proximitty effects in single conductors
- Eddy-currents flowing within single laminations at high-frequencies
- Iron core material magnetic behaviour at high-frequencies
- Dielectric losses in insulation at high-frequencies
- Frequency dependency of resistances and inductances
- The effect of end-winding sections
- Randomly wounded machines where the conductor distribution within the slot is not precisely known

New modelling methodologies are expected to deal totally or partially with the abovementioned phenomena to predict high-frequency phenomena with some degree of accuracy. For numerical methods aimed to early development, a dependency on the available data (i.e., detailed geometry, accurate material characteristics, etc.) is added to the traditional trade-off between accuracy and computational cost. The presented research in the frame of INTERACT is conceived to adress EMI-aware design at early design stages of a real PMSM, when a reduced amount of data is available. In addition, some degree of accuracy at an affordable simulation time is pursued. The main applicability of the model lays on the evaluation of early design decisions on the CM and DM impedance response of a real electrical machine. *Fig. 2-4* depicts the targeted trade-off for early design modelling.
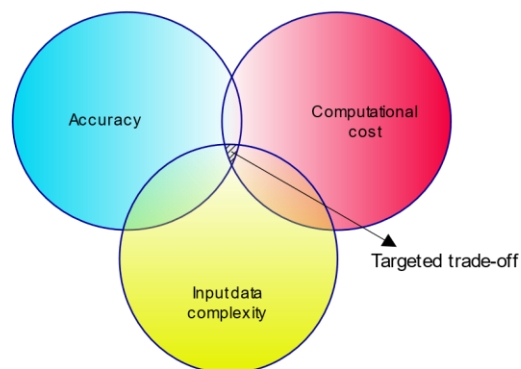
Fig. 2-4 - Targeted trade-off for a high-frequency impedance model aimed for early-stage prediction

41

3. Novel early-stage high-frequency impedance modelling applied to PMSMs

This chapter describes the numerical modelling method developed in this dissertation. It is aimed to predict the impedance response of a rotating electrical machine in both CM and DM modes during pre-prototyping stages of the machine design. This is achieved by using the 2D geometry, material characteristics and basic configuration of the machine under study. The modelling is conceived to satisfy a trade-off between accuracy, computational speed, and data simplicity.

Two different PMSMs in the frame of INTERACT are utilized as a case study to implement the method. The applications of the two studied machines are a power steering (e-PS) and an Air Conditioning Compressor (ACC) unit (e-ACC) respectively. Both machines are three-phase PMSMs with concentrated winding and double-layer slots. One of them is a 0.5 kW, 10/12 machine with 8 turns per coil and the second machine is a 4kW, 8/12 machine with 28 turns per coil. *TABLE 3-I* summarizes the main characteristics and *Fig. 3-1* shows the cross-section for both machines.

TABLE 3-I- Machines under study characteristics

	Machine 1 (e-PS)	*Machine 2 (e-ACC)*
Number of slots	12	12
Number of poles	10	8
Nominal power (kW)	0.5	4.7
Base speed (rpm)	1000	6000
Magnet remanence (T)	1.345	1.345
Turns/coil	8	28

The chapter is structured as follows. First the equivalent circuit topology is selected based on multi-conductor transmission line theory (Section 3.1). Then, the different machine parameters are extracted by using FEM (Section **Error! Reference source not found.**). An electrostatic solver is utilized to obtain parasitic capacitances in the machine slots (Section 3.2.1) while frequency-dependent resistances and inductances are obtained by using a magnetodynamic solver

(Section 3.2.2). Once the parameters are obtained, they are integrated within the equivalent circuit following the frequency-dependent nature of resistances and inductances (Section 3.3). Finally, DM and CM impedances over frequency are obtained by using a SPICE tool (Section 3.4). *Fig. 3-2* shows a block diagram of the presented modelling method.
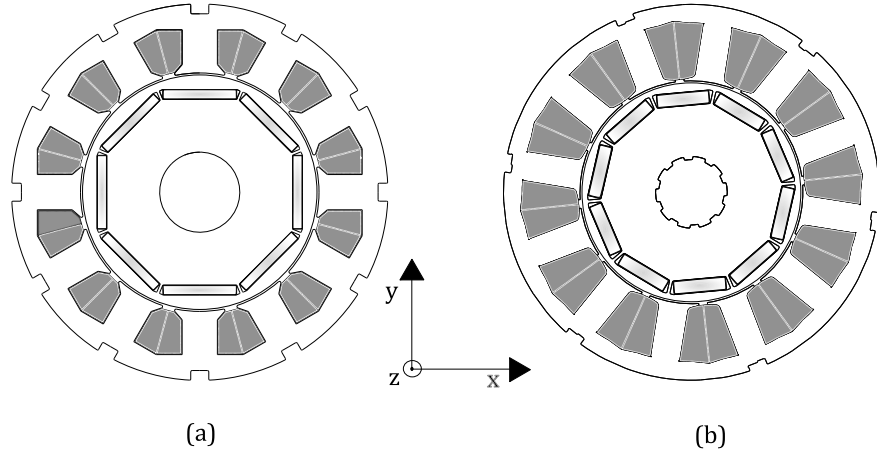
Fig. 3-1 - PMSMs under study cross-sections, (a) 8/10 e-ACC, (b) 10/12 e-PS

3.1.   Equivalent circuit representation

This section is aimed to describe the basic circuit topology and to pose the physics behind equivalent circuit representation. High-frequency modelling of electromagnetic devices is based on equivalent circuit representations, where the behaviour of the electrical signals travelling along the conductive parts is emulated. The nature of every electrical signal travelling along a conductor is distributed in space. TL structures serve as a guide for these electrical signals, which generally consist of two field components, one magnetic and one electric (laying on the xy-plane), which flow totally transverse to the direction of propagation (z-axis). TLs with their electromagnetic components geometrically distributed in this manner are known as Transverse Electromagnetic (TEM) transmission lines. This is the case of a pair of parallel conductive cables. If a wiring structure is formed by multiple conductors instead of a single pair, a Multi-conductor Transmission Line (MTL) is formed. The conductors located in a rotating machine slot can be characterized as a MTL system since they are parallel and
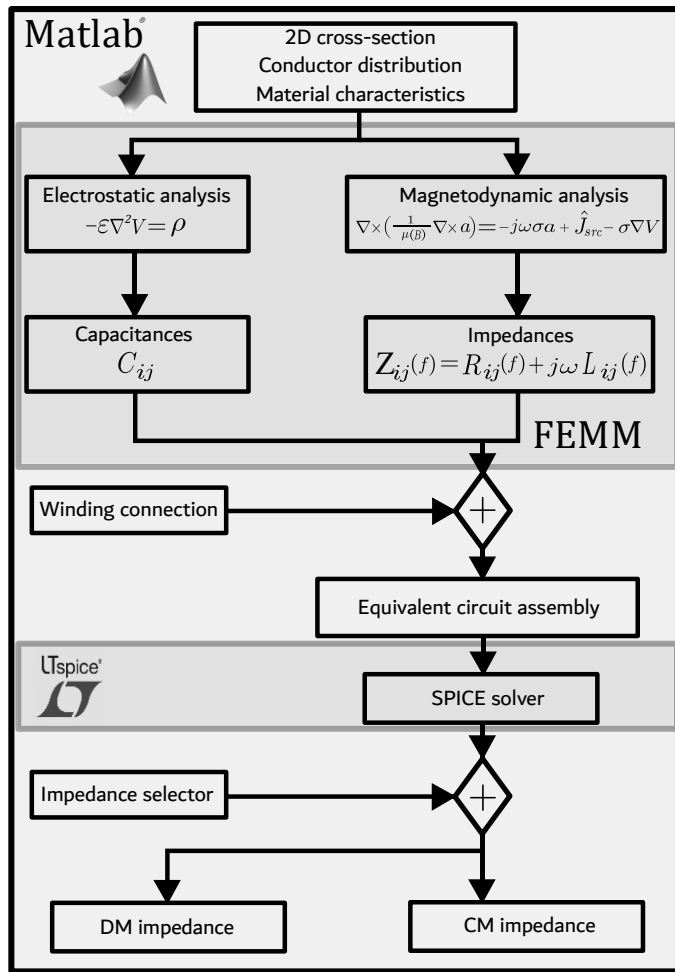
Fig. 3-2- Modelling method block diagram

insulated from each other, with different electrical signals travelling through them.

TLs with TEM behaviour induce some undesired effects on the voltage and current signals. A *time delay* is imposed in the signals as they travel along the conductors. A fraction of the travelling signal can be *reflected* at the ends of a line if the characteristic impedance of the line differs from the load and/or source impedance. The conductors have a lossy behaviour by nature due to their finite conductance and thus, the signal amplitudes are *attenuated* as they travel through the conductor. Finally, since the signals travel down the line at different

speeds (because of the rich harmonic spectrum), they can reach the end of a line at different times; this phenomenom is known as *dispersion*. At high-frequencies all these effects alter the behaviour of electromagnetic and electromechanical devices.

The derivation of the so-called *Telegrapher's equations* is necessary to understand the equivalent circuit representation of the TLs behaviour. A pair of conductors parallel to the z-axis are used to derive the expressions and circuits [15], [107]. By applying a voltage difference between the conductors, an electric field is induced with components in the xy-plane. Similarly, if current flows through the conductors, a magnetic field is induced around them in the xy-plane. These fields following TEM-TL principles suggest that a capacitance and an inductance between conductors exist when they are excited. According to this interpretation, TLs can be modelled as a series of capacitances and inductances connected in series. *Fig. 3-3* shows the induced electromagnetic fields and the distributed equivalent cicuit of series connected capacitances and inductances [107]. In addition to the inductances and capacitances, transmission lines have losses. These arise from the finite non-zero conductance of the conductive materials and from the lossy behaviour of the dielectric medium surrounding the conductors. Including these resistive losses, the distributed parameter circuit adopts the shape shown in *Fig. 3-4,* where r, l, c and g represent the per-unit length (Δz) resistance, inductance, capacitance, and conductance respectively. By applying Kirchoff's current and voltage law (i.e. KCL and KVL) in a per-unit length section of the circuit, it is possible to find the equations describing the current and voltage behaviour:

$$V(z + \Delta z, t) - V(z, t) = -r\Delta z\, I(z, t) - l\Delta z \frac{\partial I(z, t)}{\partial t}$$
$$I(z + \Delta z, t) - I(z, t) = -g\Delta z\, V(z + \Delta z, t) - c\Delta z \frac{\partial V(z + \Delta z, t)}{\partial t}$$

(3-1)

by dividing by Δz in the right and left part of the equations and taking the limit $\Delta z \to 0$, the telegrapher's equations are found:

$$\frac{\partial V(z, t)}{\partial z} = -r\, I(z, t) - l \frac{\partial}{\partial t} I(z, t)$$
$$\frac{\partial I(z, t)}{\partial z} = -g\, V(z, t) - c \frac{\partial}{\partial t} V(z, t)$$

(3-2)

These partial differential equations represent the time and space dependency of the current and voltage signals travelling through a TL.

46

Note that the circuit per unit length parameters (i.e., *r, l, c, g*) contain the information about the line (i.e., wire radii, distance between conductors, material characteristics, etc.).

(a)   (b)

(c)
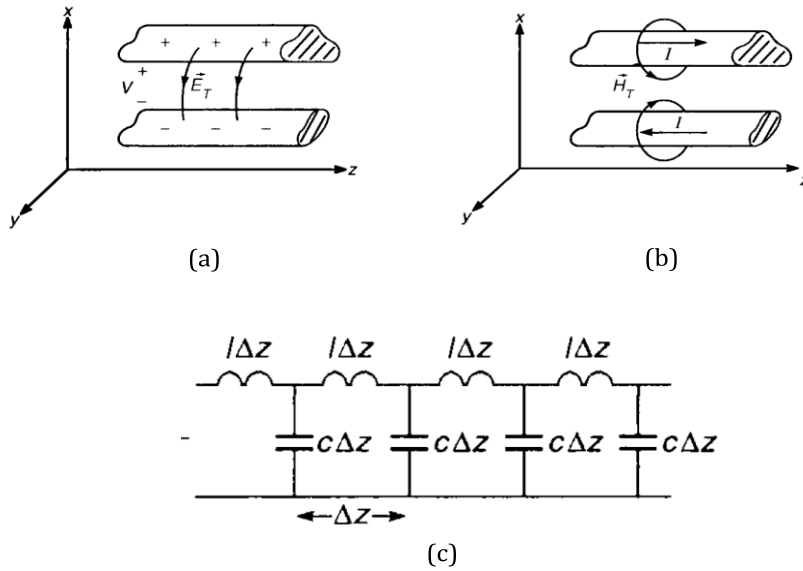
Fig. 3-3- (a) electric field in a conductor pair (b) magnetic field in a conductor pair, (c) distributed parameter circuit [26]
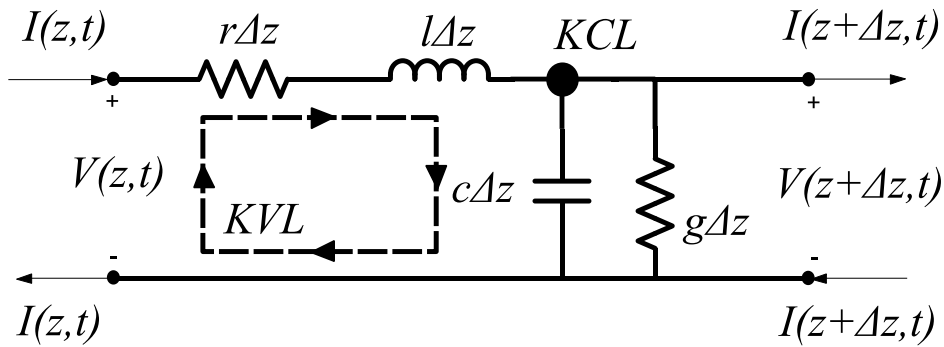

Fig. 3-4- TL section equivalent circuit with voltage and current variables and Kirchhoff laws application

47

Once the basic behaviour of a TL is understood, it is possible to apply simplifications to the circuit representation. According to Paul [26], the space dependency can be neglected if the line is electrically short at the highest frequency of interest. In other words, the lumped-circuit models will correctly process only those frequency components of the input source that are below the frequency where the line length becomes a significant fraction of a wavelength. The signal wavelength depends on the medium surrounding the conductors and on the signal frequency [26]. It is given by:

$$\lambda = \frac{v}{f} = \frac{1}{\sqrt{\mu_r \varepsilon_r}} \frac{v_0}{f} \ [\text{m}] \qquad \textbf{(3-3)}$$

where λ is the wavelength, f is the signal frequency, v is the signal speed, v_0 is the speed of light, and μ_r and ε_r are the relative permeability and permittivity of the surrounding medium respectively. A common rule of thumb states that when the signal wavelength is ten times bigger than the line length, it can be considered as electrically short ($length/\lambda > 1/10$) and it can be represented by a lumped-parameter circuit. Two types of lumped-parameter circuits are commonly used in practice, the pi-equivalent and the T-equivalent circuits. *Fig. 3-5* shows two lumped-parameter circuits and their passive elements, where $\mathcal{L}$ represents the line length in meters.

(a)   (b)
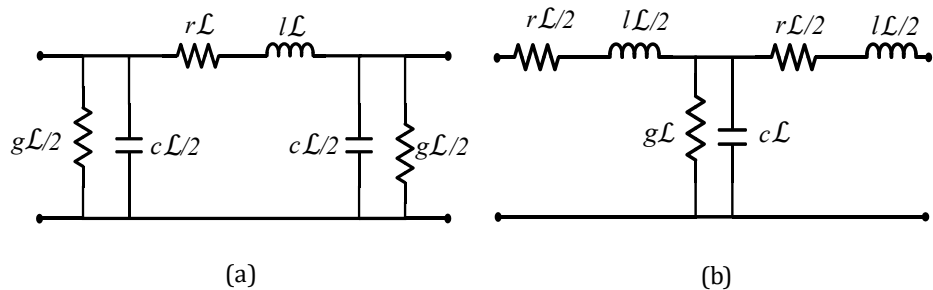
Fig. 3-5 - Lumped-parameter equivalent circuits, (a) pi-equivalent, (b) T-equivalent
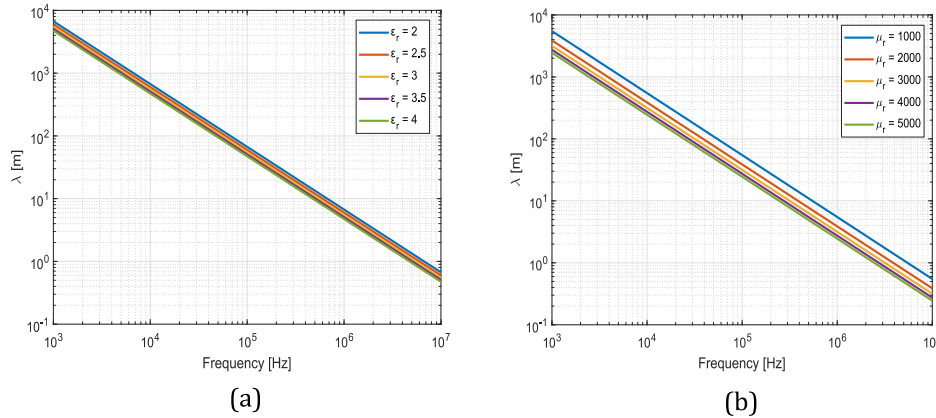
Fig. 3-6 - Wavelength for different values of the medium relative permittivity and permeability, (a) fixed permeability, (b) fixed permittivity

For a rotating electrical machine, the medium surrounding the conductors is defined by the slot insulation elements and the iron core containing the magnetic flux. In radial flux machines the conductor length ($\mathcal{L}$) equals the stack length of the stator. *Fig. 3-6* shows the wavelength of the electrical signals depending on different values of relative permeability and permittivity. From *Fig. 3-6* it is possible to confirm that lumped-parameter accuracy will decrease above 10MHz for machines with a stack length of 40/50 mm, since the stack length will be less than ten times the wavelength at those frequencies. However, the lumped equivalent circuit is considered the best option for the presented modelling method since it provides a good compromise between accuracy and computational cost. In addition, a pi-equivalent topology is chosen over the T-equivalent since frequency dependent parameters such as inductance and resistance are modelled just once. This represents a modelling advantage which will be addressed in following sections. Each conductor in the machine slots is represented by a pi-equivalent section since they all have different parameters.

3.2.   Parameter estimation

This section addresses the estimation of the equivalent circuit parameters based on 2D geometry, material characteristics, and the stator winding connection. This is achieved by using FEM and solving low frequency electromagnetic equations with planar geometry. The utilization of numerical methods allows to discretize the space to easily solve a set of partial differential equations. Four parameters are required to fully characterize the equivalent circuit: resistance, inductance, capacitance and conductance.

The conductance of the material is derived from the lossy dielectric material surrounding the slot conductors. The frequency-dependent parameters are heavily influenced by factors such as temperature, moisture, and pressure [108]. In addition, its estimation utilizing numerical methods is complex since FEM simulations are not commonly used to obtain it. A different way to estimate this type of parmeter is by using analytical formulae as shown in [109]:

$$G = 2\pi f\, C\, tan(\delta)\ \ [S] \qquad\qquad\qquad \textbf{(3-4)}$$

where C is the capacitance and $tan(\delta)$ is the loss tangent or dissipation factor of the dielectic medium. Tabulated data about dielectric material material characteristics can be found in [110]. Unfortunately, this parameter heavily changes with temperature and the type of polymer, which makes the prediction highly uncertain. Another way to estimate conductance is by using experimental methods, which is the most utilized and accurate approach. Experimental conductance tuning is utilized in works such as [84], [111], [112] and [113]. The aim of the presented model is to avoid experimental tuning. In addition, the insulation materials utilized for electrical applications are characterized by a low loss performance and the effect of the conductance is expected to slightly affect the damping of the resonance points in the impedance response as reported in [84]. Due to the above laid out reasons, the conductance is considered as zero valued for the developed model.

The per-unit length capacitances, resistances and inductances can be estimated by using FEM. The capacitances are obtained by using an electrostatic solver, while a time-harmonic or magnetodynamic solver is utilized to obtain the resistances and inductances. The open-

50

source software package FEMM [114] coupled with Matlab scripts is utilized to perform the parameter estimation.

3.2.1. Electrostatic FEM analysis

This subsection describes the electrostatic FEM analysis and the computation of parasitic capacitances in a machine slot. In addition, the geometry and input data utilized to obtain the single conductor capacitances is presented and described.

The capacitive couplings inside the machine act as a low impedance path for stray currents towards ground or the different conducting parts. Several parasitic capacitances exist between different parts of the machine (i.e., stator-to-rotor, winding-to-rotor, endwinding coupling, etc.) [96], [115]. Among all these elements, the highest capacitance values are normally associated to the coupling between winding and stator iron [90], [94]. The focus of this model is thus, placed on the parasitic slot capacitances (i.e., turn-to-ground and inter-turn).

The governing equation for this type of solver is derived from two of the fundamental Maxwell equations [114] (i.e., Gauss' law and the static version of Faraday´s law):

$$\nabla \cdot D = \rho \tag{3-5}$$
$$\nabla \times E = 0$$

where D represents the electic displacement ρ is the charge density and E is the electric field. The constitutive relationship for the electrical displacement is given by:

$$D = \varepsilon E \tag{3-6}$$

where ε is the permittivity of the dielectric material. To simplify the computation of fields, the equation is simplified by introducing the electrical potential (V) in the equation, given by:

$$E = -\nabla V \tag{3-7}$$

By combining equations (3-5), (3-6) and (3-7), the governing equation for the electrostatic solver is obtained:

$$-\varepsilon \nabla^2 V = \rho \tag{3-8}$$

51

The slot geometry of the studied machines is presented in *Fig. 3-7* and *Fig. 3-8*. Each conductor in the slots is tagged with an index. In this way, every estimated parameter can be assigned to a particular slot conductor. Note that the conductor distribution for the e-PS machine slots varies depending on the slot position. This will be taken into account when assembling the equivalent circuit of the full machine winding.

(a)   (b)
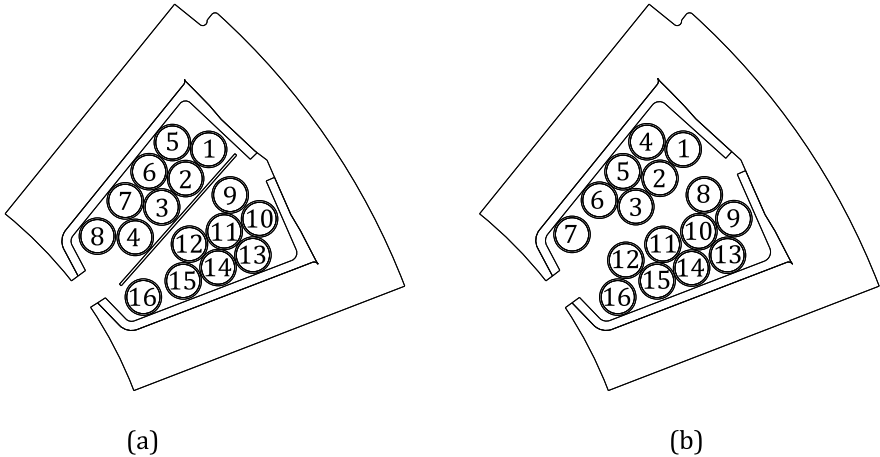
Fig. 3-7 - e-PS slot geometry and conductor indexes, (a) 8/8 slot, (b) 7/9 slot
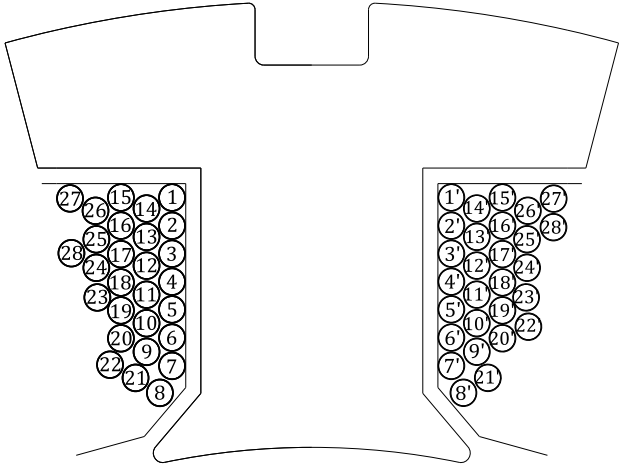
Fig. 3-8 - e-ACC single tooth geometry and conductor indexes

Regarding material characteristics, the real relative permittivity ($\varepsilon_r{}'$) or dielectric constant defines the electric field behaviour through the insulation material in the slots. Polymeric materials are utilized in the machines under study to model the slot insulation elements. The most accurate method to define the relative permittivity of the material is to perform experimental masurements of a sample of insulation material. However, the necessary equipment to perform these experiments is not easily available. The estimation from database is more feasible than for the loss tangent since the real relative permittivity has low deviation for different polymeric materials [116]. The dielectric constant or relative permittivity of each type of polymer depends on their chemical composition and on the frequency of the excitation electric field. For a static field the relative permittivity value is constant over frequency. Typical dielectric constant values for polymers utilized for electrical insulation range from 2 to 5.

The capacitance computation can be addressed by using two different approaches. The first approach is based on the stored energy in a volume. The capacitance between two electrodes is thus, obtained by using:

$$C = \frac{W_{stored}}{V^2} \, [\text{F}]$$

(3-9)

where W_{stored} is the energy stored in a volume and V represents the voltage difference between two conductive parts. The second approach and the most utilized one for parasitic capacitance computation is based on the surface charge induced in the conductors. The capacitance is thus is given by:

$$C = \frac{q}{V} \, [\text{F}]$$

(3-10)

where q is the surface charge density of the conductors.

A parallel plate capacitor model is built to check the coherence of the results by comparing FEM extracted results with analytical formulation. The geometry is defined in a simple way to compare the analytical formulation with the FEM results. The plates are infinitely thin with a surface of 10x10 mm and a dielectric thickness of 10 mm between them. *Fig. 3-9* shows the modelled capacitor and the contour plot of the voltage density.

53
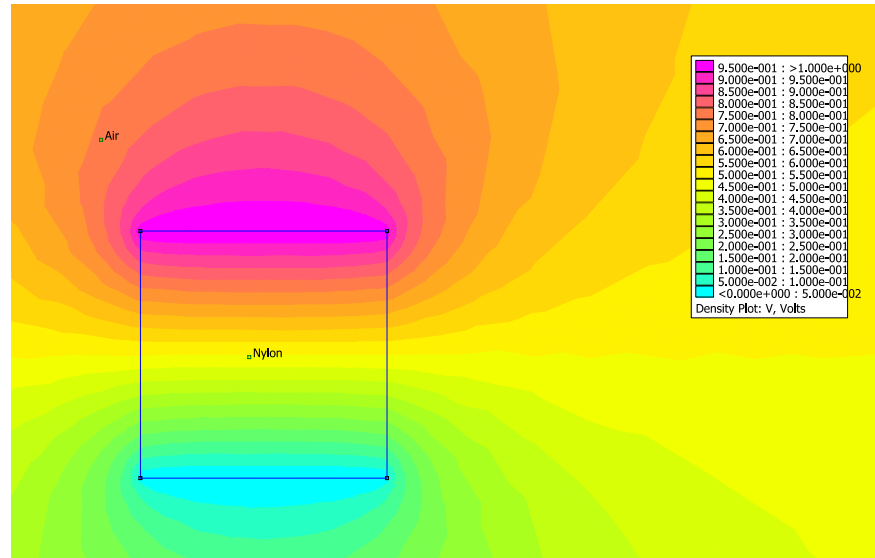
Fig. 3-9- Parallel plate capacitor geometry and electric potential density contour plot

The well-known analytical expression for a parallel plate capacitor is:

$$C = \varepsilon_r \, \varepsilon_0 \frac{A}{d} \, [\text{F}] \tag{3-11}$$

where A is the plate surface in mm^2, d is the dielectric thickness between plates and ε_0 is the permittivity of vacuum ($8.85\text{e}^{-12} \, [F \, m]$). The comparison between the two capacitance computation methods and the analytical formula for the parallel plate capacitor is shown in *TABLE 3-II*. In addition, the effect of the relative permittivity of different insulation dielectric materials is studied. The two methods using FEM provide identical values, while the analytical formulae result on a very close agreement in the capacitance value. However, when a more complex geometry is analyzed the analytical formulae lacks accuracy when compared with FEM. From this point on, the surface charge technique is utilized for capacitance estimation.

54

TABLE 3-II - Capacitance values for different computation methods

Dielectric material	Computation method		
	Stored energy	Surface charge	Analytical
Air ($\varepsilon_r = 1$)	0.092 pF	0.092 pF	0.089 pF
Polypropilene ($\varepsilon_r = 2.2$)	0.198 pF	0.198 pF	0.195 pF
Paper ($\varepsilon_r = 3$)	0.268 pF	0.268 pF	0.266 pF
Nylon ($\varepsilon_r = 3.8$)	0.338 pF	0.338 pF	0.336 pF

The FEM mesh is defined to have at least two rows of nodes within each geometric domain. The material characteristics of each domain are considered isotropic. Boundary conditions can be applied to the domain edges. In the case of electrostatic analysis, these are related to the voltage excitation of each body. *Fig. 3-10* shows an example for a e-ACC machine slot, where the mesh density, boundary conditions and material characteristics are shown. The mesh inside the conductors is not created since the excitation and the induced surface charge densities are placed in the conductor edges.

The different parasitic capacitances within the slot are organized in matrices. In this way, for each slot with a particular conductor distribution, a *NxN* matrix is obtained, where *N* represents the number of conductors in the slot. Each entry of the matrix is computed by setting the *i-th* conductor with a unitary voltage while the remaining *j-th* conductors and the slot walls are set to zero voltage. In this way, one analysis per conductor is carried out with each of the *i-th* conductors under 1V excitation. The surface charge on the *j-th* conductors and the iron walls represent the capacitance according to equation (3-10). *Fig. 3-11* illustrates the capacitance estimation method. The capacitance matrices for the case study machines are presented in *Fig. 3-12* and *Fig. 3-13*.
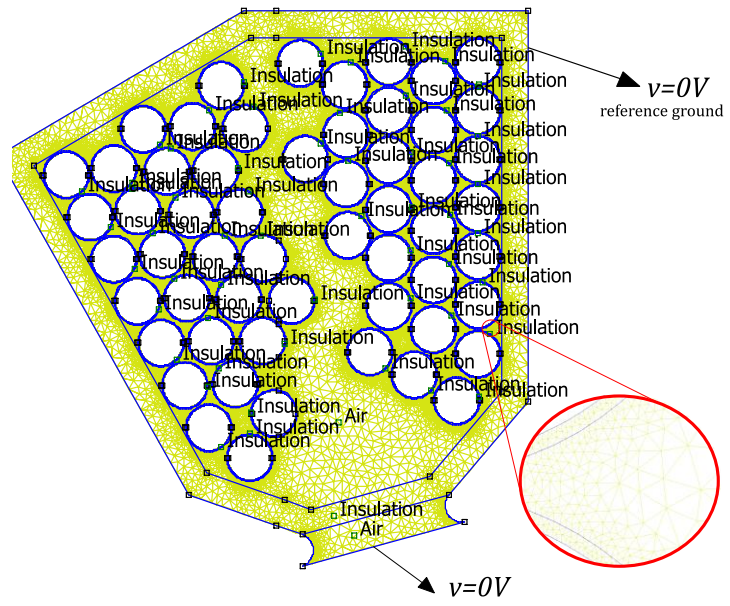
Fig. 3-10 - e-ACC machine slot with mesh density, boundary conditions and material characteristics for electrostatic FEM analysis
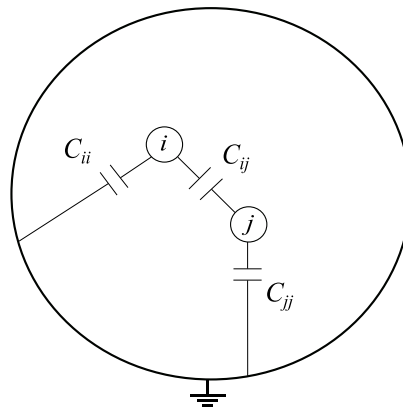
Fig. 3-11 - Capacitance extraction schematic

56
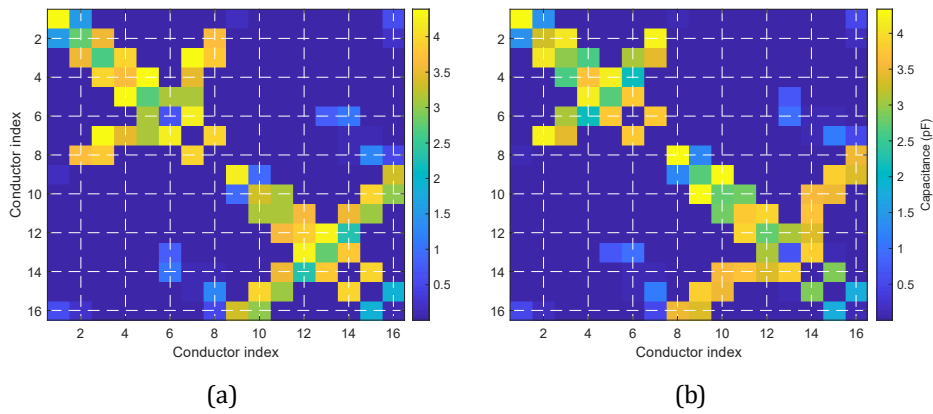
Fig. 3-12 - e-PS capacitance matrices ($\varepsilon_r = 3.5$), (a) 8/8 slot, (b) 7/9 slot
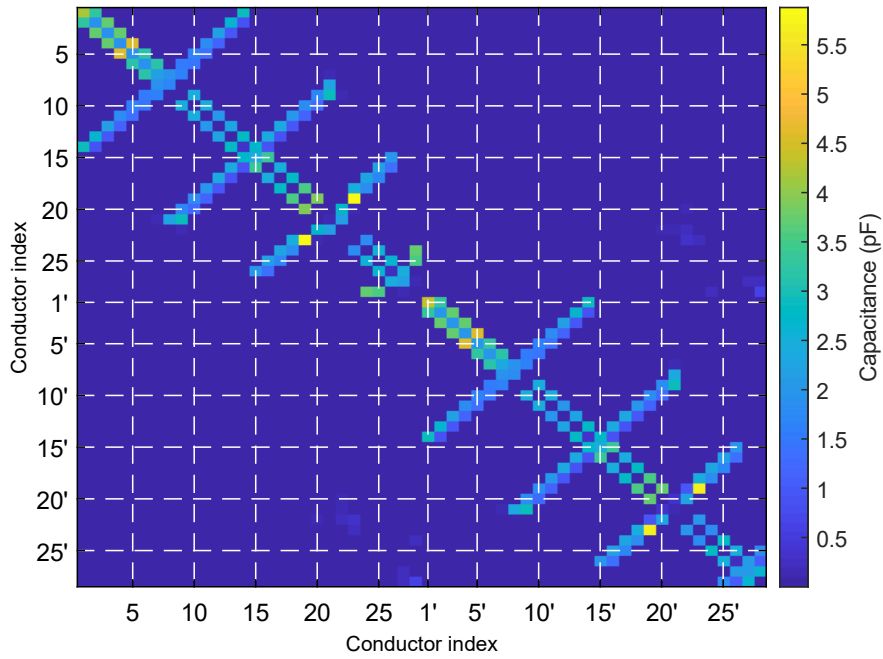
Fig. 3-13- e-ACC capacitance matrix ($\varepsilon_r = 3.5$)

57

Fig. 3-12 and Fig. 3-13 show the strongest capacitive couplings in the slot. The highest capacitance values are located between neighboring turns and between the iron and the turns facing the slot walls. Weak capacitive couplings are observed for distant turns and conductors not facing the iron. The voltage contour plot of a single conductor excitation shows how the potential isolines are confined between neoighbouring elements. Fig. 3-14 and Fig. 3-15 show these contour plots for the two machines under study.
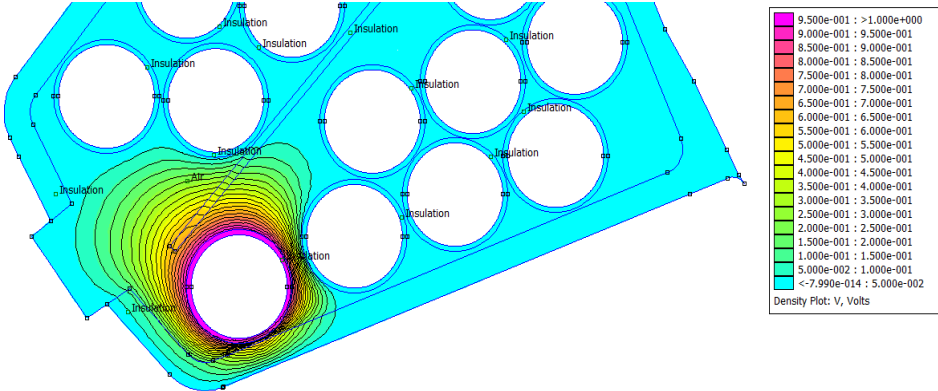
Fig. 3-14 - e-PS voltage density plot when conductor 1 is excited
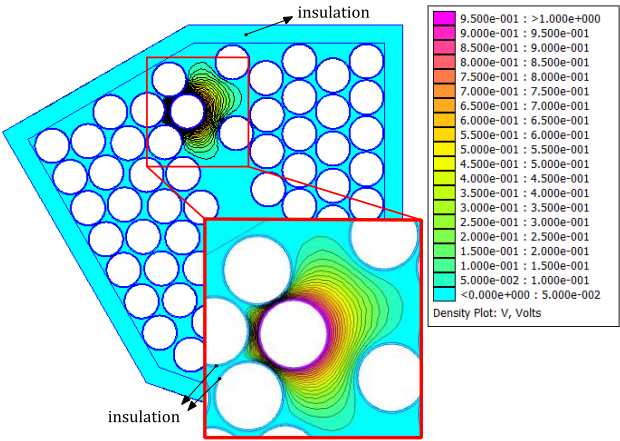
Fig. 3-15 - e-ACC voltage density plot when conductor 28´ is excited

58

3.2.2. Magnetodynamic analysis

This subsection describes the magnetodynamic analysis and the computation of frequency-dependent resistances and inductances in a machine coil. Three main effects take place at high frequencies: limited flux penetration in the iron core, and skin and proximity effects. These phenomena affect the inductance and resistance of each conductor in the slots. Thus, these parameters will possess an inherent frequency dependency that must be taken into account. By using 2D FEM and the proper assumptions all these phenomena can be accounted for and the frequency dependent resistances and inductances can be accurately estimated.

The governing equation of the magnetodynamic solver is based on the magnetic vector potential formulation:

$$B = \nabla \times A \qquad \text{(3-12)}$$

where B is the magnetic flux density and A is the magnetic vector potential. This can be integrated in the Ampere´s loop law ignoring the electric displacement, and the magnetic field constitutive equation:

$$\nabla \times H = J \qquad \text{(3-13)}$$
$$B = \mu H$$

where H is the magnetic field strength, J is the current density and μ represents the magnetic permeability of the media. Note that in case of nonlinear magnetic characteristics (e.g., saturated soft magnetic material), the magnetic permeability is function of the flux density ($\mu(B)$). By grouping equations (3-12) and (3-13), the following expression is obtained:

$$\nabla \times \left(\frac{1}{\mu(B)} \nabla \times A \right) = J \qquad \text{(3-14)}$$

To account for induced electric fields, equation (3-14) is integrated in the Faraday´s law equation in its non-stationary shape. The considered equation and the current density constitutive expression are given by:

$$\nabla \times E + \frac{\partial B}{\partial t} = 0 \qquad \text{(3-15)}$$
$$J = \sigma E$$

where σ represents the material conductivity. By using the magnetic vector potential instead of B (i.e., equation (3-12)), the electric potential from equation (3-7) and substituting the constitutive equation in the Faradaýs law, it is possible to write:

$$J = -\sigma \dot{A} - \sigma \nabla V \qquad \text{(3-16)}$$

Substituting equation (3-14) into (3-16), the governing equation for the magnetodynamic solver is found:

$$\nabla \times \left(\frac{1}{\mu(B)} \nabla \times A \right) = -\sigma \dot{A} + \dot{J}_{src} - \sigma \nabla V \qquad \text{(3-17)}$$

where J_{src} represents the applied current sources in the FEM solver. For simulations where the fields oscillate at a fixed frequency or in frequency-domain, all the AC quantities and the magnetic vector potential are expressed in phasorial notation.

The main challenge of the 2D FEM analysis is related to the flux penetration in the iron core. At high enough frequencies, eddy currents will start flowing within single lamination. These will create an increased reaction field that will confine the main magnetic field within the slot boundaries. Thus, at high-frequency excitations each single lamination in the iron core must be modelled to accurately map the inductance and resistance of each conductor. This is not a feasible implementation in practice since it would require a computationally expensive 3D simulation with a very fine mesh. To overcome this limitation and to enable the utilization of a coarse 2D mesh in the iron core, a homogenized iron core model is built.

3.2.2.1. Iron core model

The iron core model is based on the correlation of the laminated anisotropic block to a solid isotropic non-conducting material with an effective frequency-dependent magnetic permeability [108]. *Fig. 3-16* shows a single lamination geometry and the magnetic field and current density distribution. The frequency-dependent complex permeability is derived from the 1D magnetic field solution along the axial direction of a lamination (z-axis) [117]:

$$\frac{\partial^2 H_x(z)}{\partial z} = k^2 H_x(z) \qquad \text{(3-18)}$$

whose general solution is provided by:
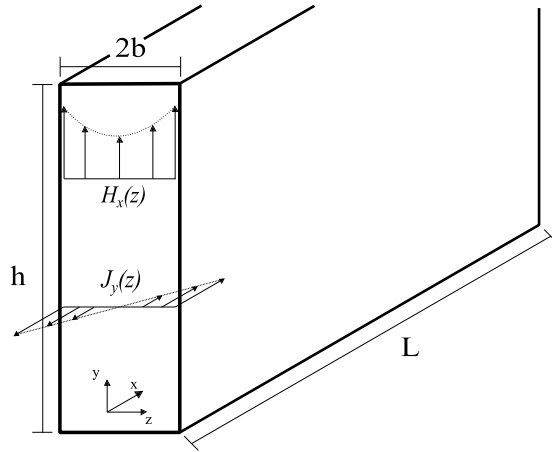
Fig. 3-16 - Single lamination geometry, and magnetic field and current density distribution

$$H_x(z) = H_1 e^{kz} + H_2 e^{-kz} \qquad \text{(3-19)}$$

The particular solutions are obtained by equalizing the magnetic field strength in the lamination edges ($H_x|_{(z=b)} = H_x|_{(z=-b)}$)

$$\begin{cases} H_0 = H_1 e^{kb} + H_2 e^{-kb} \\ H_0 = H_1 e^{-kb} + H_2 e^{kb} \end{cases} \qquad \text{(3-20)}$$

solving this system and grouping terms, the following expression is obtained:

$$H_1 = H_2 = \frac{H_0}{\cosh(kb)} \qquad \text{(3-21)}$$

where H_0 represents the magnetic field strength in the lamination edges. Substituting equation (3-21) in (3-19) the solution for the magnetic field along the lamination z-axis is obtained:

$$H_x(z) = H_0 \frac{\cosh(kz)}{\cosh(kb)} \qquad \text{(3-22)}$$

Note that k represents the complex term defined by $k = \frac{(1+j)}{\delta}$ where δ is the field penetration depth ($\delta = \sqrt{\frac{2}{\omega \sigma \mu}}$). *Fig. 3-17* shows the normalized magnetic field strength along a lamination thickness of 1mm. The thickness value is selected to better identify the effect of the frequency on the normalized magnetic field distribution.

61
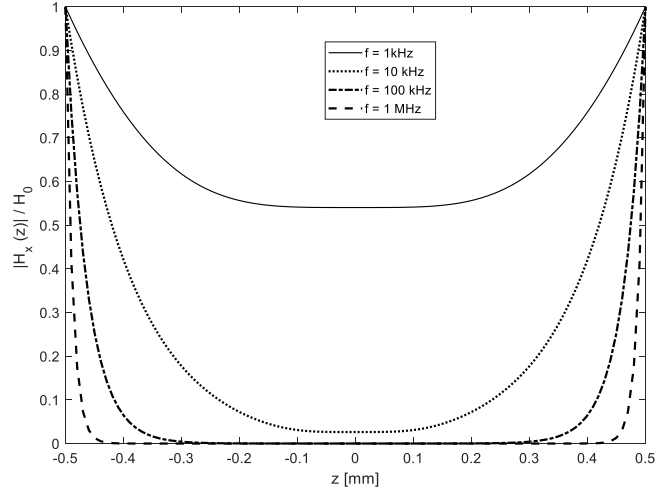
Fig. 3-17 - Normalized magnetic field strenght along a 1mm lamination for different oscillating frequencies

The effective complex permeability is defined as the average magnetic-flux density in a lamination normalized to the surface magnetic field:

$$\mu_{eff} = \frac{1}{H_0} B_{avg} = \frac{1}{H_0 2b} \int_{-b}^{b} (\mu_{DC} H) dz \tag{3-23}$$

where μ_{DC} is the low frequency relative magnetic permeability. Substituting equation (3-22) into (3-23) and integrating along the lamination thickness, the frequency dependent effective magnetic permeability expression is found:

$$\mu_{eff}(f) = \mu_{r,DC} \, \mu_0 \, \frac{\tanh(kb)}{kb} = \mu_0(\mu' - j\mu'') \tag{3-24}$$

where $\mu_{r,DC}$ is the relative pemeability at low frequencies. The real and imaginary parts of the effective permeability are defined as:

$$
\begin{cases}
\mu' = \dfrac{\mu_{r,DC} \, \delta}{2b} \left(\dfrac{\sinh\left(\frac{2b}{\delta}\right) + sin\left(\frac{2b}{\delta}\right)}{\cosh\left(\frac{2b}{\delta}\right) + cos\left(\frac{2b}{\delta}\right)} \right) \\[4mm]
\mu'' = \dfrac{\mu_{r,DC} \, \delta}{2b} \left(\dfrac{\sinh\left(\frac{2b}{\delta}\right) - sin\left(\frac{2b}{\delta}\right)}{\cosh\left(\frac{2b}{\delta}\right) + cos\left(\frac{2b}{\delta}\right)} \right)
\end{cases}
\tag{3-25}
$$

The frequency dependent functions defining the two terms of the effective pemeability are shown in *Fig. 3-18*.

62
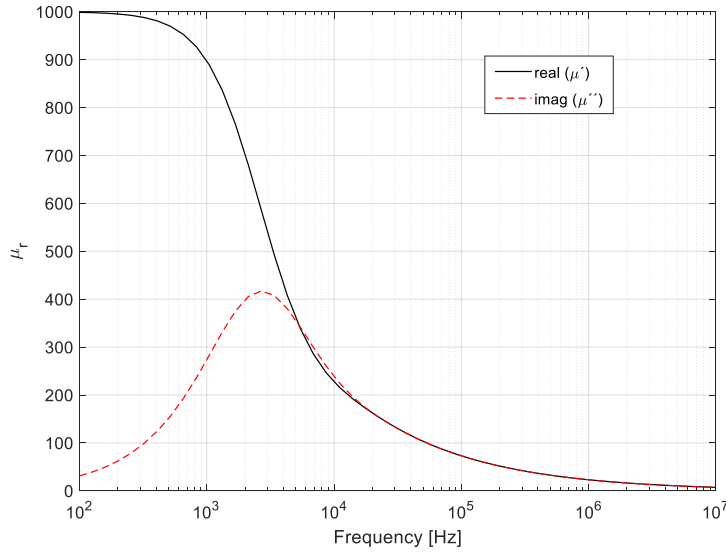
Fig. 3-18 - Complex effective permeability (μ_{eff}), $\mu_{r,DC} = 1000$, $\sigma = 1.9\frac{MS}{m}$, $2b = 0.5\ mm$

The real term of the magnetic permability is associated to the capability of the magnetically permeable material to store magnetic field while the imaginary term is linked to the dissipative losses in the same material. From *Fig. 3-18* it is possible to observe that an attenuation of the real term takes place at a certain frequency. This occurs when the ratio $2b/\delta$ equals to one and it indicates that the main flux encounters increased penetration resistance from that frequency on. That frequency is commonly known as cut-off frequency and it is defined by:

$$\frac{2b}{\delta} = 1 \xrightarrow{yields} f_{cutoff} = \frac{1}{4\pi\mu\sigma b^2} \tag{3-26}$$

Thus, depending on the lamination thickness and the material characteristics the effect of the laminated iron core on the winding impedance will differ. *Fig. 3-19* shows the real term of the effective complex permeability depending on the lamination thickness.

The effect on the winding impedance by the action of the laminated iron core can be analyzed analytically. This mathematical explanation is provided to justify the increase of the impedance when

63
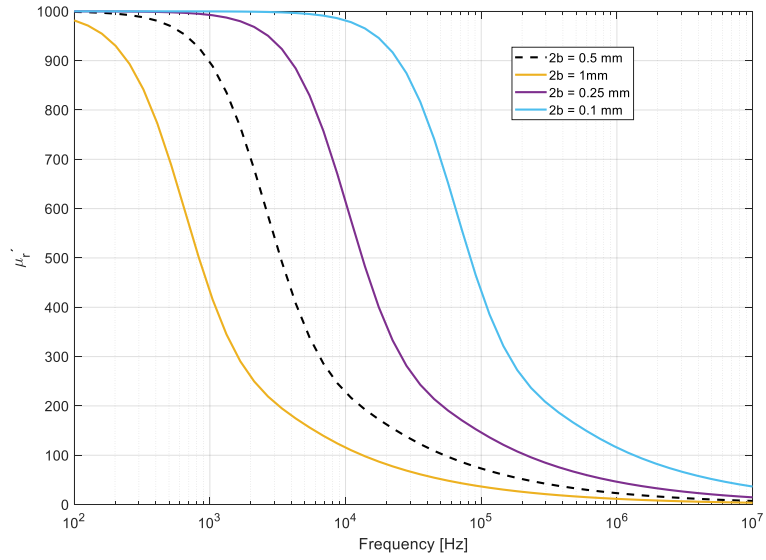
Fig. 3-19 - Effect of the lamination tickness on the effective complex permeability real term (μ'), $\mu_{r,DC} = 1000, \sigma = 1.9 \frac{MS}{m}$

the core homogenized model is taken into account [117]. Assuming a closed core with infinitely thin insulation layers between laminations, the magnetic field strength caused by a winding with N turns is given by:

$$H_0 = \frac{IN}{l}$$

(3-27)

where l represents the mean length of a flux line in the xy-plane. On the other hand, the voltage induced in the windinding for AC oscilation is:

$$U = j\omega N \Phi_c$$

(3-28)

where Φ_c is the sum of partial fluxes in individual laminations, which is defined as:

$$\Phi_c = \int_{-b}^{+b} h \, B \, dx = \frac{2\delta h\mu}{1+j} \, H_0 \, tanh(1+j)\frac{b}{\delta}$$

(3-29)

For a packet of laminations of axial length d containing $d/2b$ laminations, the sum of partial fluxes is defined as:

$$\Phi_c = \frac{\delta dh\mu}{(1+j)b} \, H_0 \, tanh(1+j)\frac{b}{\delta}$$

(3-30)

64

If voltage and the current expressions are known, the impedance of a winding surrounded by a packet of thin laminations can be obtained by using equations (3-27), (3-28) and (3-30) in the impedance definition.

$$Z = \frac{U}{I} = \frac{j}{(1+j)} \frac{\delta dh\mu\omega}{lb} N^2 \tanh(1+j)\frac{b}{\delta} \tag{3-31}$$

For low frequencies (i.e., far below the cutoff value) equation (3-31) is simplified:

$$Z = j\omega \frac{dh\mu}{l} N^2 \xrightarrow{yields} L_0 = \omega \frac{hd\mu}{l} N^2 \tag{3-32}$$

where L_0 is defined as static inductance. Substituting the static inductance value in the impedance expression and separating its real and imaginary terms, the increased AC winding inductance and resistance values are obtained:

$$\begin{cases} L_{AC} = L_0 \dfrac{\delta}{2b} \dfrac{\sinh\left(\frac{2b}{\delta}\right) + \sin\left(\frac{2b}{\delta}\right)}{\cosh\left(\frac{2b}{\delta}\right) + \cos\left(\frac{2b}{\delta}\right)} \\[4ex] R_{AC} = \omega L_0 \dfrac{\delta}{2b} \dfrac{\sinh\left(\frac{2b}{\delta}\right) - \sin\left(\frac{2b}{\delta}\right)}{\cosh\left(\frac{2b}{\delta}\right) + \cos\left(\frac{2b}{\delta}\right)} \end{cases} \tag{3-33}$$

From equation (3-33) it is possible to conclude that when a closed laminated iron core is inserted in a coil of N turns, the resistance and inductance values at high frequencies increase. Thus, by using an iron core model with a frequency-dependent effective complex permeability this effect is accounted for in the FEM simulations. For each simulation frequency the complex permeability is re-calculated and input in the software. To account for the complex nature of this permeabily, the module and the argument are used as an input. The conductivity value in the iron region is set to zero since eddy currents are already accounted in the complex permeability. Every material characteristic is considered as isotropic.

3.2.2.2. Iron core model validation

The homogenized iron core model presented previously is now validated by comparing impedance values with results obtained from a more complex 3D model. 3D models properly map the magnetic field and current density distribution within a lamination. A geometry

representing a closed iron lamination surrounding three round conductors is buit to simplify the analysis. The geometry of the simplified model is shown in *Fig. 3-20*. TABLE 3-III shows the main characteristics of the model.
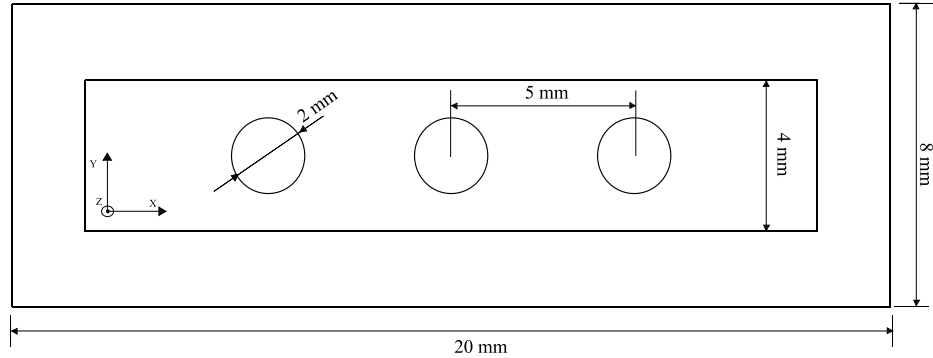
Fig. 3-20 – Simplified slot geometry for iron core model validation

TABLE 3-III - Validation model input data

Copper conductivity [MS/m]	58
Iron conductivity [MS/m]	1.9
Lamination thickness [mm]	0.1
$\mu_{r,DC}$	1000

Three modelling approaches are implemented utilizing the same geometry. The first method utilizes an extruded 3D mesh implemented in a commercial electromagnetic software since FEMM package does not include 3D capabilities. The software utilizes a magnetic vector potential notation for the electromagnetic solver, and it incorporates the possibility of including a user defined 3D mesh. The second method is a 2D approach with adjusted iron core mesh to account for the iron core penetration depth. The model takes into account the limited flux penetration in the iron core in 2D, where the current density and magnetic flux cannot be mapped properly. The third approach utilizes the homogenized iron core model described previously in a 2D simulation with a coarse mesh in the iron region. *Fig. 3-21* shows the extruded 3D mesh and *Fig. 3-22* shows the two considered 2D meshes in FEMM. The mesh in the conductors is adapted to account for the skin depth in all three models.

66
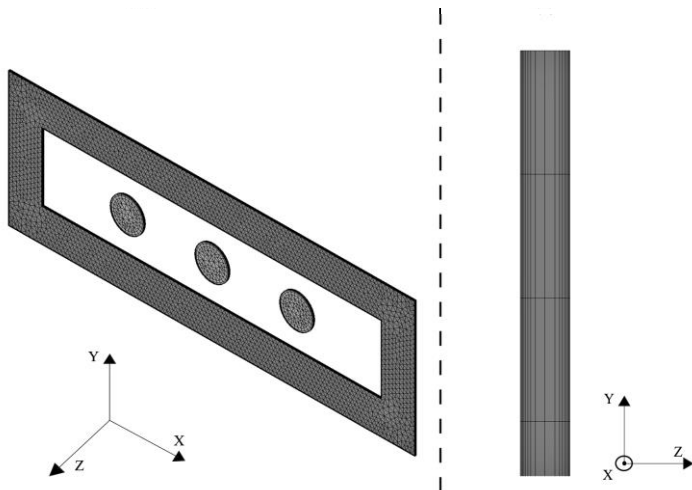
Fig. 3-21 - Extruded 3D mesh for simplified geometry
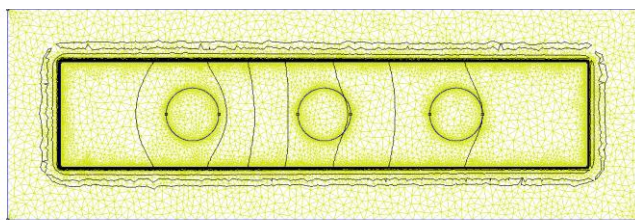
(a)
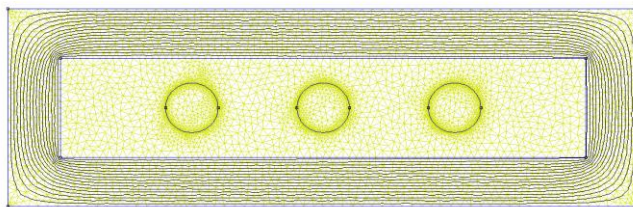
(b)

Fig. 3-22 - 2D simplified model approaches showing the mesh and real flux density lines when the left conductor is excited, (a) method 2, adjusted mesh in the iron limits ($\mu_r = 1000$), (b) method 3, homogenized iron core model ($\mu_r = \mu_{eff}(f)$),

67

By analyzing the 3D model, it is possible to verify if the current density and the magnetic field strength are properly mapped. The eddy currents flowing within the single laminations will start to have a meaningful value around the cut-off frequency. *Fig. 3-23* shows a current density vector plot for a single conductor excitation of 10 kHz. The current flowing within the lamination form closed loops around it, since it is assumed that the lamination is perfectly insulated. *Fig. 3-24* shows the comparison between the normalized field strength in the 3D model and the analytical expression for the considered lamination thickness and material characteristics at 100 kHz. Both current density and magnetic field strength show realistic characteristics, which means that the impedance of the conductors within the slot will have higher value than the ones extracted form the 2D model without homogenized core.
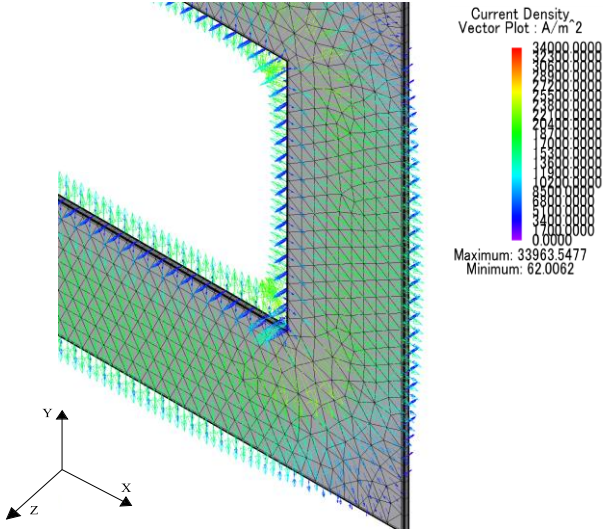
Fig. 3-23 - 3D model current density vector plot (phase=0) when left conductor is excited (I=1+0j)

The impedances in the three types of model are calculated by exciting the left conductor with a unit real-valued current ($I = 1 + 0j$) and analyzing the voltage drop on each conductor. By using the well-known impedance expression ($Z = U/I$), the voltage drop extracted from the FEM software represent the impedance on the conductors. *Fig.*

68

3-24 shows the self-impedance (i.e., the impedance of the excited conductor) comparison between the three analyzed models. As predicted analytically, the impedance under realistic conditions is greater than for a 2D model not considering the real eddy currents in the lamination. The homogenized model closely follows the trend of the obtained 3D results and, in this way, it is possible to verify the efectiviness of the homogenization method.
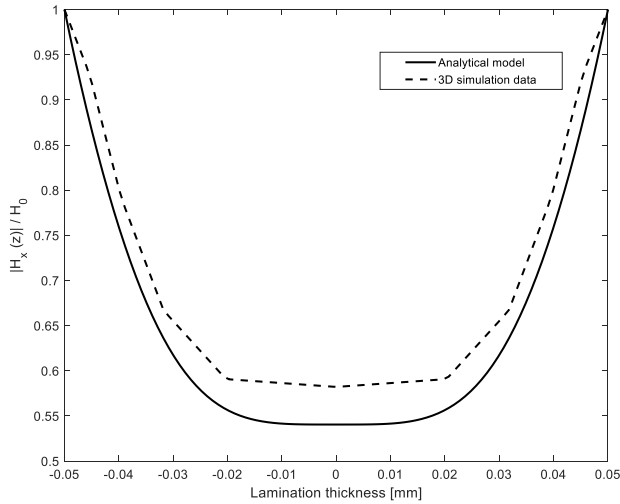
Fig. 3-25 - Normalized H field distribution over a 0.1mm lamination at 100 kHz, 3D simulation vs analytical solution
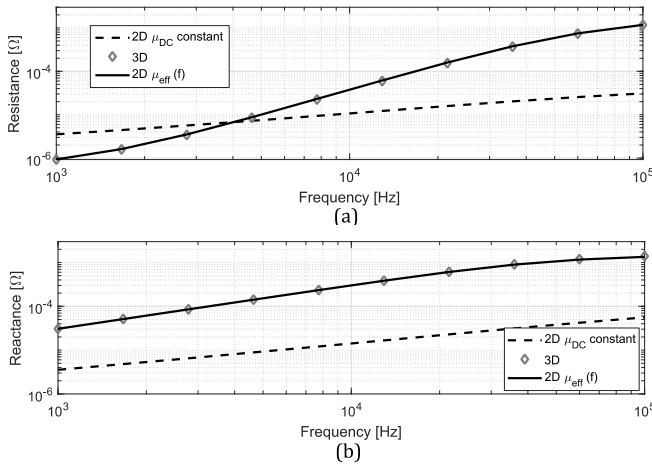
Fig. 3-24 - Self-impedance real (a) and imaginary (b) terms, comparison between three different modelling approaches

69

3.2.2.3. Low-frequency permeability estimation

The low-frequency permeability estimation for a real case study machine is explained in this subsection. The iron core of rotating electrical machines is commonly made of soft magnetic material with ferromagnetic behaviour. The most representative parameter of these materials is the magnetic permeability (μ) which relates the magnetic field strength with the magnetic flux density as described by the constitutive law from equation (3-13). The real behaviour of the relationship between magnetic field and flux density is non-linear. When the material is saturated an increment in magnetic field strength will not produce any change on the flux density due to the saturation of the material.

It is necessary to understand the ferromagnetic material microscopic physics to properly address the estimation of the low-frequency permeability. Ferromagnetic materials are formed by small regions known as Weiss domains (or magnetic domains) separated between them by transition regions known as Bloch Walls (BW). Each magnetic domain is oriented towards a different direction when no external magnetic field is applied. *Fig. 3-26* shows how magnetic domains and BWs are organized in a small piece of ferromagnetic material when no external magnetic field is applied.
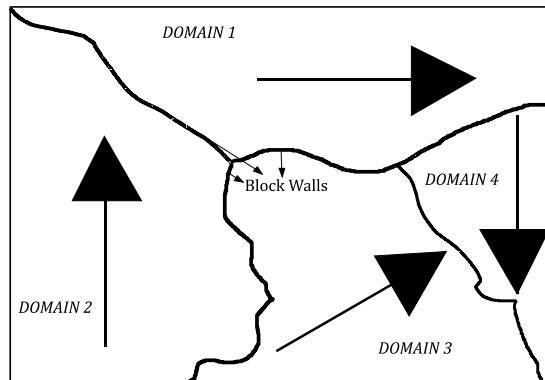
Fig. 3-26 - Magnetic domains and block walls example in ferromagnetic materials with no external magnetic field

70

When an external magnetic field is applied to a totally demagnetized iron sample, the BH characteristic will follow the initial magnetization curve. This curve has different stages depending on how the magnetic domains and BWs react to this external field. *Fig. 3-27* shows the initial magnetization curve for a ferromagnetic material [118]. The external magnetic field (H) is applied gradually from zero to an infinite value. At very low amplitudes, the magnetic domains remain unchanged (a) and, with increasing magnetic field, the domains that are better aligned with the external field will start growing at the expense of others (b). For small vaued external magnetic fields, the material returns to its previous state without hysteresis. At higher values of the magnetic field, the magnetic domain movement becomes irreversible (c), and the material will start showing hysteretic behaviour. Around the knee region a single domain is present (d) and further magnetization is only produced by the magnetic domains fully aligning with the external field (e). When an AC field is applied, the full hysteresis loop is followed, as shown in *Fig. 3-28*, where B_r is the remanent flux density and H_c is the coercive magnetic field strength.
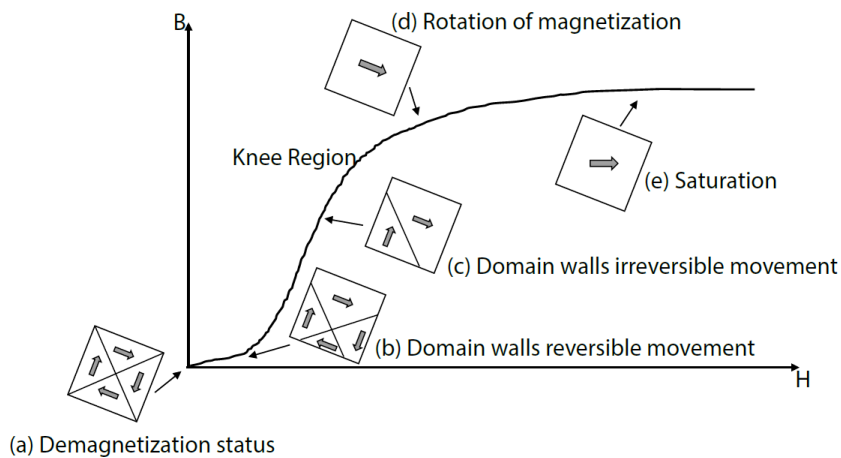
Fig. 3-27 - Magnetization process in ferromagnetic materials *[118]*

71
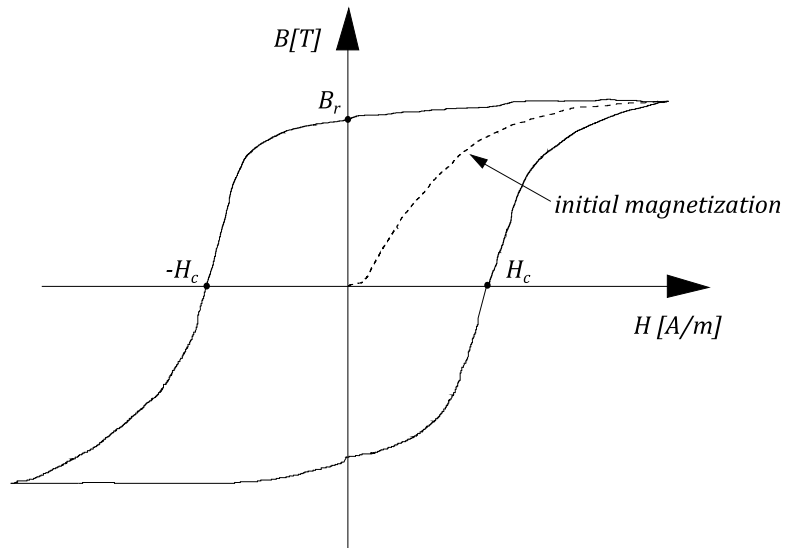
Fig. 3-28 - Hysteresis loop for a ferromagnetic material
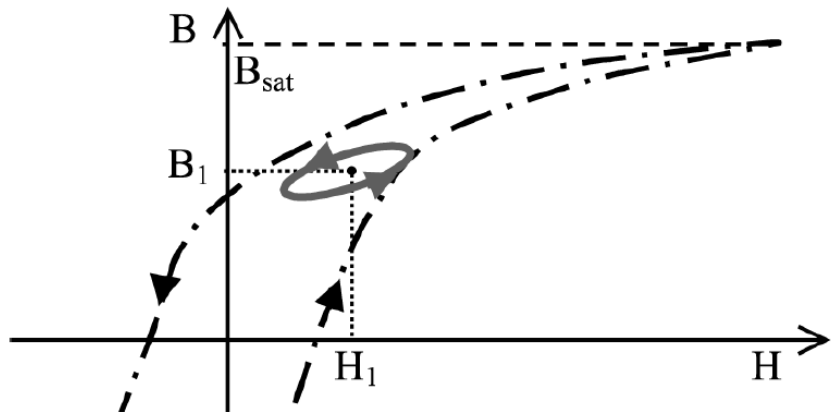
Fig. 3-29 - Minor loop around the instantaneous working point *[119]*

The broadband impedance obtained from the high-frequency analysis of a real rotating machine is based on the injection of low-amplitude signals swept in frequency. These small amplitude signals will follow minor hysteresis loops around the instantaneous working point, which moves on the main loop at the basic frequency [119]. *Fig.*

72

3-29 describes these local minor hysteresis loops. For a machine in absence of an external magnetic field, the minor loops will be located around the remanence point at standstill conditions. In the case of a PMSM, the magnets of the rotor will excite the magnetic domains of the iron core and these loops will be located somewhere in the BH characteristic.

To estimate the relative permeability of the instantaneous working point of the material characteristic, it is assumed that the iron core characteristics are located in the initial magnetization part of the BH curve. In this way, it is possible to use the low-frequency BH curve provided in the material data sheet. This is a commonly available characteristic provided by electrical steel manufacturers. The low frequency B-H curve, the magnets attributes, and the machine cross-section are utilized to obtain the average flux density in the stator nodes at a fixed rotor position. By using the average flux density (B_{avg}), the equivalent average magnetic field strength (H_{avg}) is found, and the equivalent low-frequency permeability can be estimated by using:

$$\mu_{r,DC} = \frac{B_{avg}}{H|_{B_{avg}}\mu_0} \tag{3-34}$$
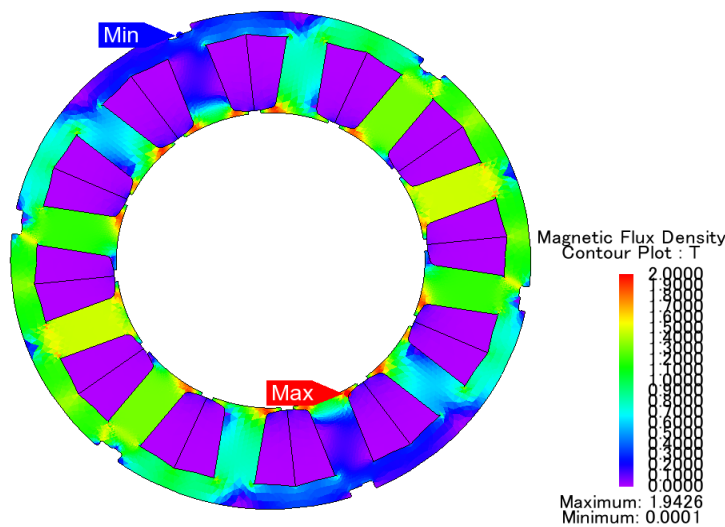
Fig. 3-30 – e-PS stator flux density contour plot at a fixed rotor position
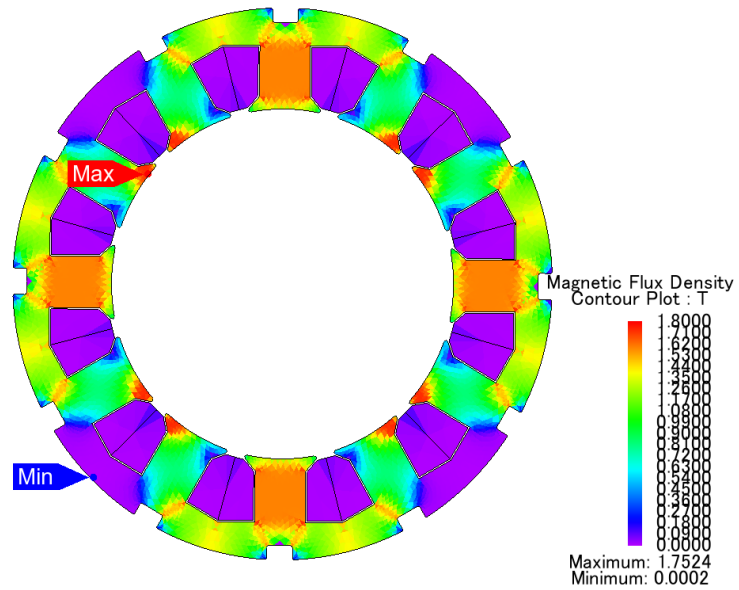
Fig. 3-31 – e-ACC stator flux density contour plot at a fixed rotor position

Fig. *3-30* and *Fig. 3-31* show the contour plot of the stator flux density at a fixed rotor position for both studied machines. From the FEM software it is possible to export the B-field in the stator nodes. A Nastran file is generated showing each stator node and their B-field values in x and y components (B_x and B_y), from which the absolute value is easily obtained ($|B| = \sqrt{B_x^2 + B_y^2}$). The utilized magnets have a remanence of 1.345 T. The material used to build both machines is a M330-50A electrical steel [120]. *Fig. 3-32* shows the BH curve at 50 Hz for the utilized electrical steel, highlighting the average flux densities obtained for both machine stators.
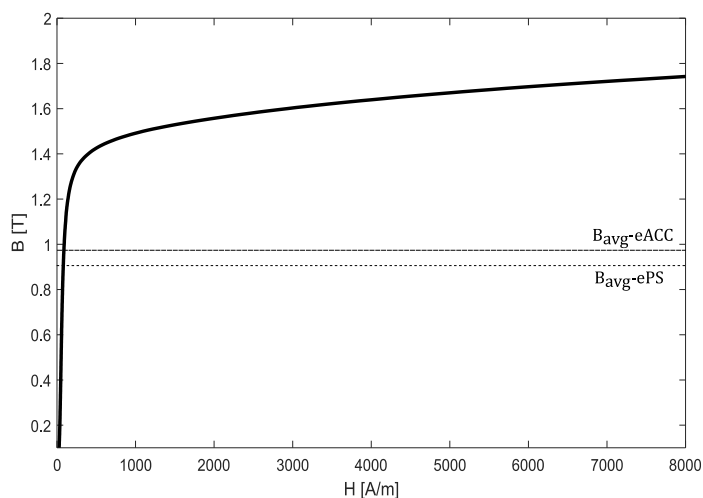
Fig. 3-32 - M330-50A BH characteristics at 50 Hz and machine stator average flux density values

3.2.2.4. Slot impedances calculation

The impedances for each conductor in the slot are computed in this subsection. The utilized geometry for the magnetodynamic analysis is the same as the presented in *Fig. 3-7* and *Fig. 3-8* without including insulation material, since the conductivity of these materials is very low, and their relative permeability can be neglected.

Three phenomena arise as effect of the high-frequency excitation. The *limited flux penetration* in the iron core is emulated by the homogenized iron core introduced in previous subsections of this chapter. The *skin effect* in single conductors is defined as the tendency of AC current to concentrate near the conductor surfaces. The skin depth (δ) is defined as the distance between the outer surface of the conductor and the layer when the current density tends to zero. The expression for the skin depth is similar to the magnetic field penetration depth expression. The skin depth is inversely proportional to frequency, reaching very small values for very high frequencies. If the skin depth is larger than the conductor radius, the current density will be evenly distributed within the conductor. *Fig. 3-33* shows the current density disctribution for a 1mm diameter conductor where the skin

75

depth is analyzed at different frequencies and *Fig. 3-34* shows the corresponding countour plot.
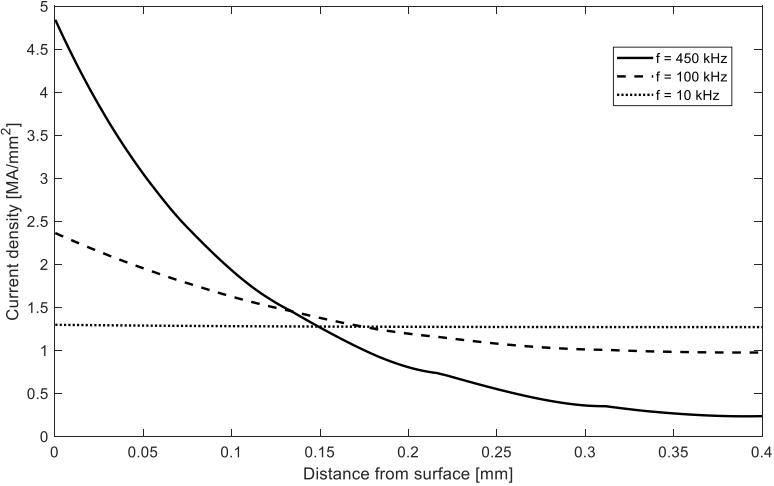
Fig. 3-33 - Current density distribution within a 1 mm round conductor for different excitation frequencies
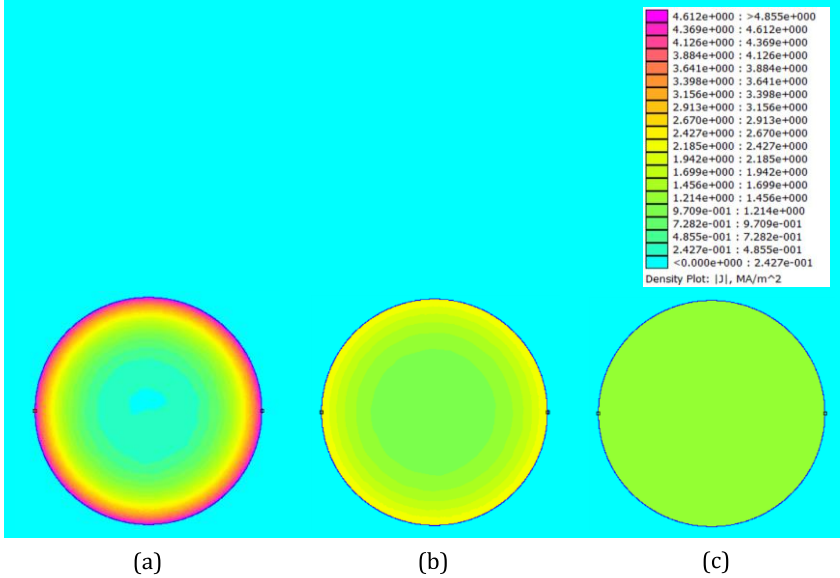
Fig. 3-34 - Round conductor absolute current density contour plot with skin effect ($\sigma = 59.6\ MS/m$), (a) 450 kHz, (b) 100 kHz, (c) 10 kHz
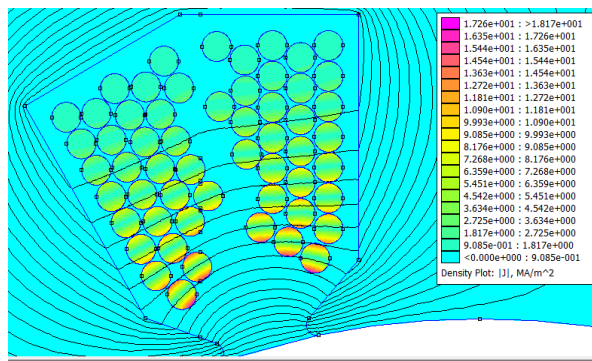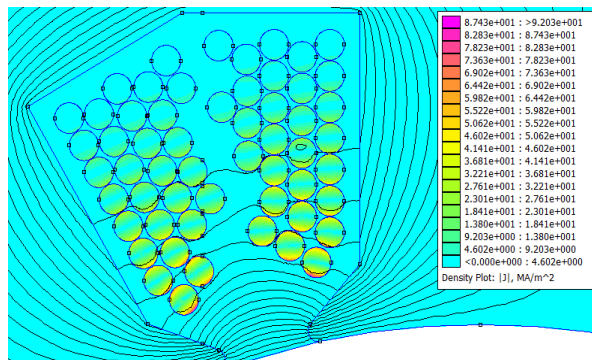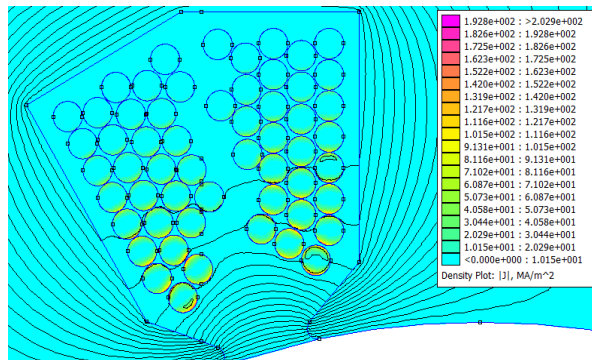
Fig. 3-35 - Current density absolute value contour plot and real flux lines of a machine slot with skin and proximity effects, (a) 10 kHz, (b) 100 kHz, (c) 450 kHz

The *proximity effect* is defined as the uneven AC current

distribution within a conductor as effect of the current flowing in the nearby conductors. It takes place when more than one conductor are placed together in a coil such as the ones in rotating electrical machines. This phenomenom causes the impedance of each conductor within the slot to be different for each other. *Fig. 3-35* depicts a machine slot current distribution when skin and proximity effects take place for different excitation frequencies. Note that the real flux density lines are not confined in the edges of the slot since the conductivity of the homogenized iron core is zero.
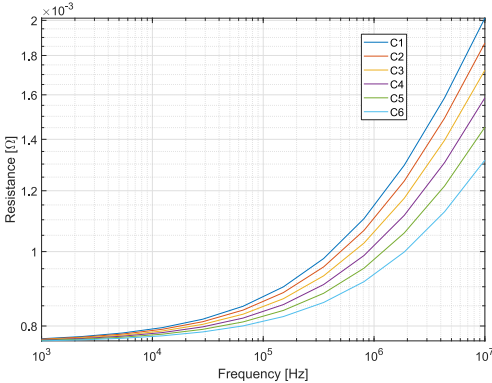
(a)
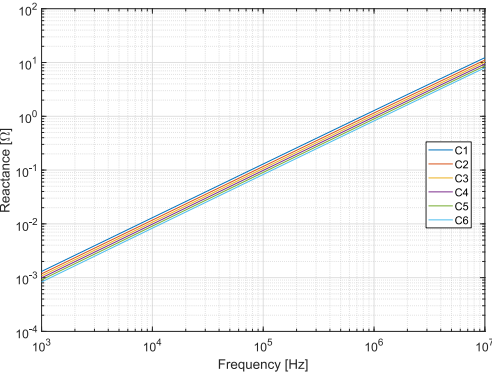
(b)

Fig. 3-36 - Real and imaginary terms of the self-impedance for six conductors within the e-ACC machine slot, (a) resistance (R), (b) reactance (X)

To accurately account for the skin and proximity effects, the conductors mesh is adapted to the skin depth in the copper. For each simulation frequency the geometry is remeshed and all the simulation

78

parameters (e.g., complex effective permeability, copper conductivity, etc.) are input in the model. Dirichlet boundary conditions ($A = 0$) are set in the external edges of the iron core and on the slot bottom edge in contact with the air gap.

The frequency dependent impedances for each conductor in the slot are computed by separately exciting each single conductor with a real-valued unitary current. The voltage drop on the excited conductor is the self-impedance and the voltage drops on the other slot conductors are the mutual impedances. Mutual effects between conductors of different slots are not considered since the flux penetration depth at high frequencies is smaller than the tooth width. The real part of the frequency-dependent impedances represents the resistive term (R), and the imaginary part is the reactance (X), from which the inductance value can be extracted by using the reactance definition ($X = j\omega L$). Thus, the real and imaginary terms of the machine impedances can be organized in matrices, where the diagonal entries represent the self-terms, and the off-diagonal entries represent the mutual couplings between conductors. *Fig. 3-36* shows the frequency dependency of the impedance for different self-terms. *Fig. 3-37* shows the matrix representation for the resistances and the inductances of the e-ACC machine slot for different frequencies of excitation.

The resistance clearly increases with the frequency, while the inductance slightly decreases in the studied frequency range. The reactance value is utilized instead of the inductance to ease the practical implementation of the frequency dependency. The largest inductive terms are observed in the self-inductances for the conductors close to the slot walls. Resistance values follow the same trend. The weakest terms are the mutual couplings between distant conductors. The matrices follow similar trends than for the capacitive coulpings with the exception that the mutual couplings are stronger in the impedance matrices. Thus, mutual couplings are expected to greatly contribute to the full impedance response and cannot be neglected. By analyzing the matrix patterns, it is possible to identify the terms within the same layer and between conductors in different layers.
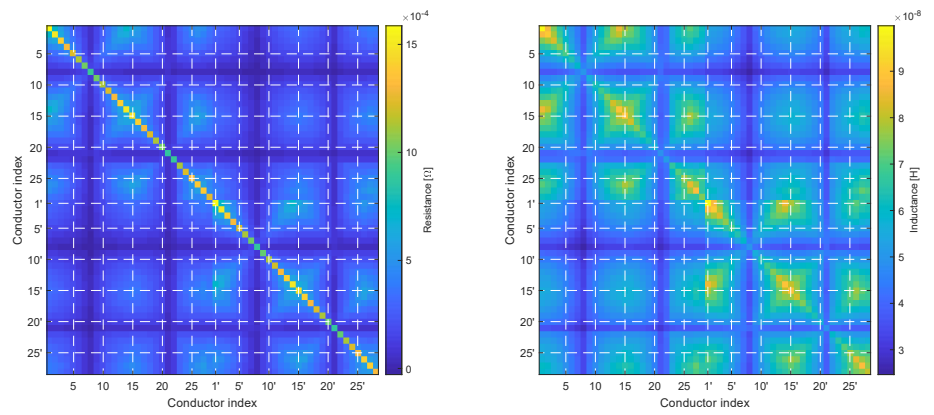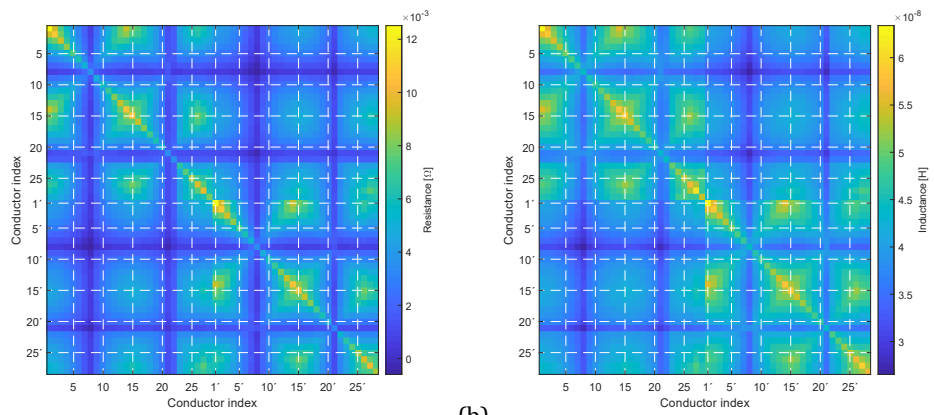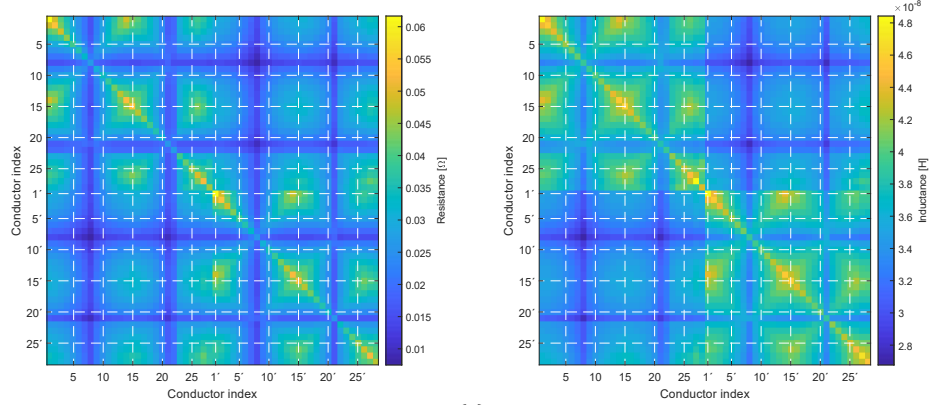
Fig. 3-37 - Impedance matrices for a slot of the e-ACC machine with resistance (left) and inductance (right) terms, (a) 10 kHz, (b) 100 kHz, (c) 1 MHz

3.3.   Equivalent circuit assembly

This section describes the process to implement the winding equivalent circuit. The parameters computed in the electrostatic and magnetodynamic analyses are connected forming pi-equivalent circuits for each conductor. This is achieved by using a SPICE tool, where a nodal approach is utilized to compute the nodes' voltage and current utilizing the Kirchoff´s laws. The most complex feature of the built circuit is the frequency dependency of the resistance and inductance, which will be adressed in detail.

3.3.1. Frequency dependency implementation

The frequency dependency of resistances and inductances is taken into account by using the Laplace transform together with active SPICE elements such as behavioral current and voltage sources. The utilization of pi-equivalent circuits makes possible to implement a single series impedance per-conductor, which eases the circuit implementation. The SPICE elements utilized in the circuit allow the usage of analytical expressions containing the Laplace variable (s). According to the definition of this variable, the frequency dependency can be easily described by using:

$$s = j\omega \xrightarrow{yields} f = \frac{s}{j2\pi}$$

(3-35)

Self-impedances are represented by voltage-dependent current sources with an infinitely large resistance connected in parallel. The parallel resistance is used to ensure stability and solver compliance. The aim of mutual impedances is to represent the voltage drop caused by currents flowing in different conductors. To emulate this phenomenom behavioural voltage sources are utilized, where the source represents the voltage drop caused by the currents flowing in different elements of the circuit. The expressions for the impedance utilizing the Laplace variables are given by the combination of a transfer function ($G(s)$) containing the impedance values and the voltage and current signals from the SPICE software:

$$\begin{cases} G(s) = R(s) + j\,X(s) \\ I_{self} = \dfrac{1}{G(s)}\,V_{self} \\ V_{mutual} = I_{mutual}\,G(s) \end{cases} \qquad \textbf{(3-36)}$$

where I_{self} is the current injected by the voltage dependent current source, V_{self} is the voltage driving this source, V_{mutual} is the voltage drop caused by the current I_{mutual} flowing in a different circuit element.

A simple simulation model is built to check the the validity of the frequency dependency emulation method. It consists of two identical impedances with unitary real and imaginary parts and a unitary mutual imaginary coupling connected in series. The impedance of a circuit can be obtained in many ways in the SPICE simulator. The chosen method is to excite the circuit with a unitary real valued current swept in frequency and to extract the voltage in the node in which the source is connected. Fig. *3-38* shows the two simple circuits and Fig. *3-39* shows the impedance comparison. The impedances match perfectly thus, validating the utilization of Laplace expressions in active sources.
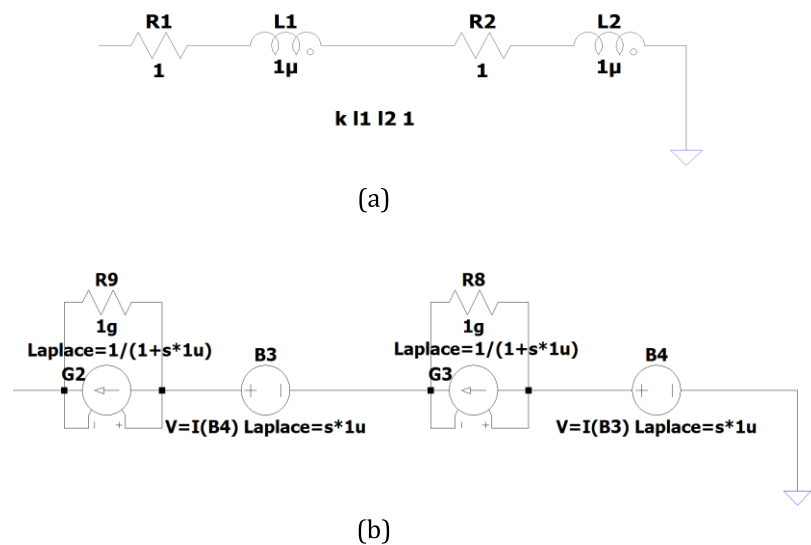
Fig. 3-38 - SPICE simple example to test the circuit implementation methodology, (a) standard expression, (b) proposed methodology
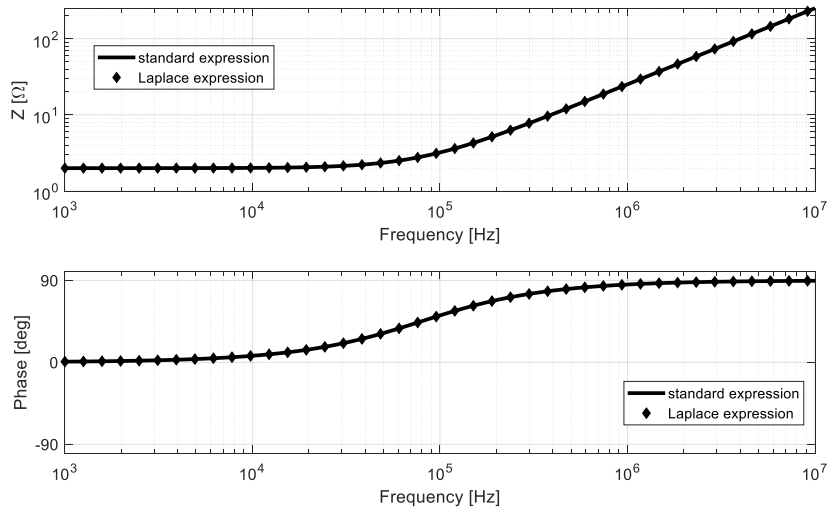
Fig. 3-39 - Calculated impedances by using standard and Laplace circuit elements

The next procedure is related to the impedance response representation utilizing analytical formulae. The proposed approach is based on a curve fitting technique that estimates the parameters for each impedance response. Different analytical formulae can be utilized to describe the impedances behaviour. However, only two expressions are considered as the best candidates for fitting the impedance responses. The first expression is a two term gaussian function of the shape:

$$f(x) = a_1 e^{-\frac{(x-b_1)^2}{2c_1}} + a_2 e^{-\frac{(x-b_2)^2}{2c_2}} \tag{3-37}$$

where a, b and c represent the different parameters of the function. The second expression is a power function with only three different parameters:

$$f(x) = a\,x^b + c \tag{3-38}$$

The curve fitting is performed by using the Matlab curve fitting toolbox. The upper and lower limits for the function parameters are not bounded for the Gaussian formulation and only the c parameter is limited in its lower boundary to avoid negative initial values in equation (3-38). The robustness option is not utilized in order to speed up the

83

iterative computation. The algorithm for optimization is of the trust-region type. Three points per decade are obtained from the FEM solver, which are considered enough for accurate fitting. Fig. *3-40* shows the comparison between the two considered analytical expressions and the FEM data. Both functions provide accurate estimation for both resistance and reactance. The power function involves a reduced number of parameters for the fitting. In addition, the gaussian formulation utilizes more complex arithmetic operators such as exponentials and logarithms, which hinders the computation in the SPICE solver. Thus, the power formulation is preferred as a result of a tradeoff between accuracy, simplicity and method compliance. The major drawback for the power formula is that some missaccuracies are found in some mutual terms. This is caused by the function shape and cannot be eliminated.
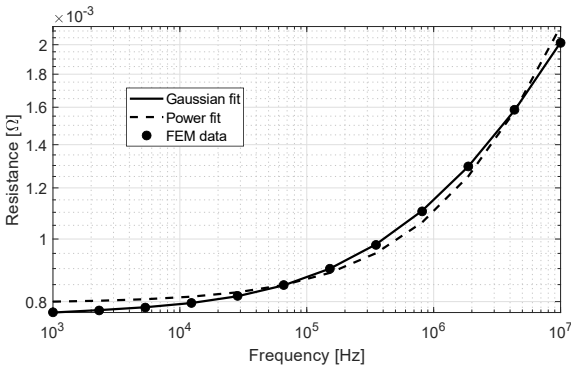
(a)
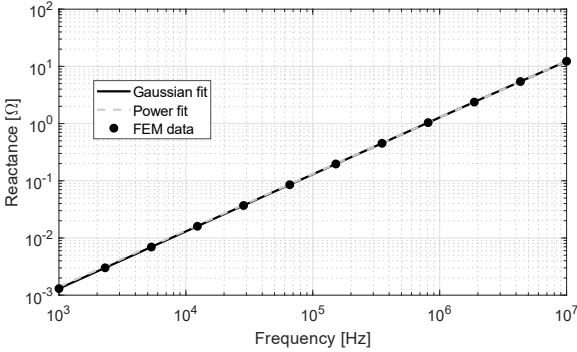
(b)

Fig. 3-40 - Curve fitting method differences, (a) Resistance (R), (b) Reactance (X)

84

The last step for the frequency dependency implementation is to embed the impedance values for each conductor in the Laplace active sources. By combining equations (3-35), (3-36), and (3-38), the expressions for the impedance utilizing Laplace transform and power formulation are obtained:

$$\begin{cases} Z(s) = R(s) + jX(s) \\ R(s) = a_1 \left(\dfrac{s}{j2\pi}\right)^{b_1} + c_1 \\ X(s) = a_2 \left(\dfrac{s}{j2\pi}\right)^{b_2} + c_2 \end{cases}$$

(3-39)

These formulae are implemented in the active sources described previously according to equation (3-36). *Fig. 3-41* shows the comparison between the impedances obtained from the active sources and the FEM simulations. The discrepancies observed in the figure are caused by the function shape. Three parameters for each impedance (i.e., self- and mutual) are obtained from the curve fitting application. These parameters are organized in three matrices. The matrices are organized by using the same logic as for the impedances shown in *Fig. 3-37*.
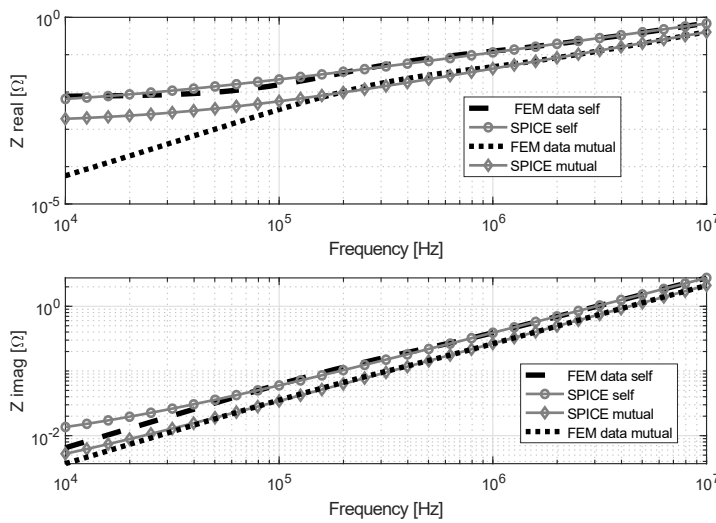
Fig. 3-41 - FEM vs SPICE self- and mutual impedances comparison

85

3.3.2. SPICE equivalent circuit

This subsection addresses the assembly of the equivalent circuit of the stator winding. One pi-equivalent circuit is utilized for each single conductor in the slots. Two single slot conductors form a coil turn and by connecting the different turns in series a coil is built. These coils can be connected in different ways to form the stator winding. For the case study machines, 12 coils are utilized (because of the 12 slots with two layers) with different connection schematics. *Fig. 3-42* shows the coil connections for both studied machines.
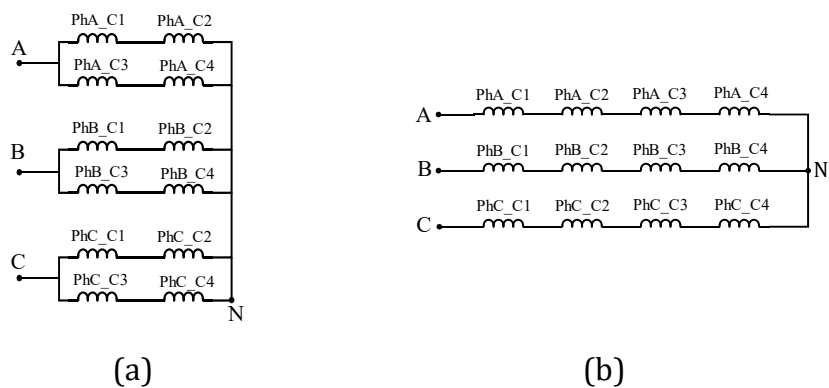
Fig. 3-42 - Stator winding connections, (a) e-PS, (b) e-ACC

The pi-equivalent circuits are connected in series and in parallel following the connection schematic of *Fig. 3-42*. The total number of conductors for each machine depends on the number of turns per coil. Thus, two pi-equivalent circuits per turn connected in series are implemented. A total of 672 (12 times 56 conductors) and 192 (12 times 16 conductors) pi-equivalent sections are utilized for the e-PS and the e-ACC machine respectively. *Fig. 3-43* shows two schematics for a *n* single slot conductors, differenciating between the theoretical and the practical SPICE circuits, the latter including frequency-dependent elements. Note that *G(s)* represents the impedance expression form equation (3-36) and that the infinitely large resistance in parallel with the voltage controlled current source is not included in the schematic due to visualization issues.

86
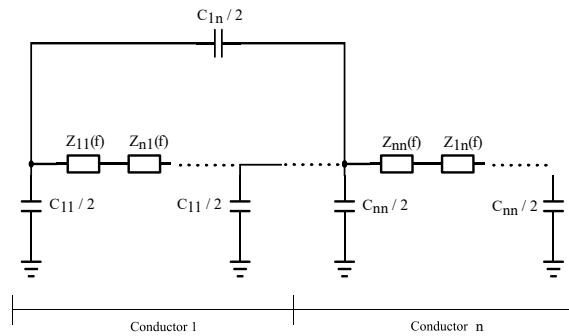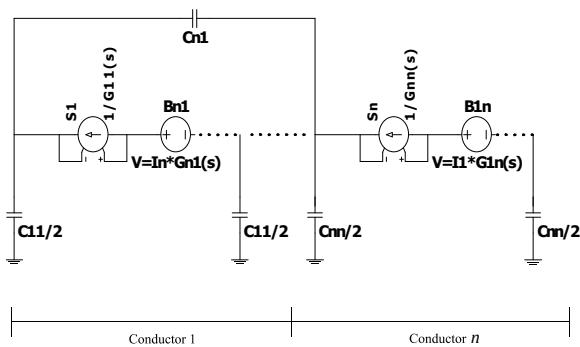
Fig. 3-43 - Equivalent circuit with n-conductors connected in series, (a) Theoretical circtuit, (b) Practical SPICE circuit

The SPICE implementation of such a large number of circuit nodes and elements poses a difficulty related to the graphic interface of the software. In practice, it is not feasible to build every single element and connection by using such graphic interface and thus, alternative methods must be used. The solution for this problem is the usage of SPICE netlists, which are scripted documents (i.e., .cir, edited in Notepad) containing all the information about the circuit elements, their connection, and their parameters. These netlists are built by using Matlab scripts, which set the circuit connections, assign the parameters to each element, automatically launch de simulation, and retrieve the results. An example of some Netlist lines can be consulted in Appendix A.

Interphase terms (i.e., mutual impedances and interturn capacitances) represent a problem related to circuit connection and computational speed. For double layer slots, strong interphase couplings are found, and they must be taken into account. The mutual terms between phases are difficult to be implemented because of the netlist building process, since one coil is built at a time. Thus, it is difficult to reference nodes from coils different from the one which is being built at that time. To solve this issue, interphase terms are lumped together by connecting them to the first node of each coil. In addition, this solution significantly reduces the computational effort of the SPICE solver since a lot of nodes are lumped into a single one.

3.4. Simulation results

This subsection presents the machine impedance simulation results and sums up all the required inputs for the model. The most significant input parameters are listed in TABLE 3-IV. The frequency range is not limited by the SPICE solver but a limitation in accuracy is expected at some tenths of MHz since only one pi-equivalent section per conductor is utilized. In addition, the lack of end-winding data will also have an impact in the accuracy of the results.

TABLE 3-IV - Model inputs for the two case study machines

	Machine 1 (e-PS)	Machine 2 (e-ACC)
Copper conductivity (MS/m)	59.6	59.6
Steel conductivity (MS/m)	2.38	2.38
Lamination thickness (mm)	0.5	0.5
Stack length (mm)	58	40
Magnet remanence (T)	1.345	1.345
BH curve data	M330-50A	M330-50A
Relative permittivity	3.5	3.5
Turns/coil	8	28
Slot wall thickness (mm)	0.6	0.6
Conductor diameter (mm)	2	1
Conductor insulation (% nom.)	2	2
Interphase insulation thickness. (mm)	0.15	-
Winding connection	Fig. 3-42	Fig. 3-42
Cross-section geometry	Fig. 3-1	Fig. 3-1
Conductor distribution and indexes	Fig. 3-7	Fig. 3-8

88

The frequency limits for the results simulations are set between 10 kHz and 30 MHz, with the upper limit corresponding to the CEs test upper frequency. The two modal impedances are obtained by injecting a real valued unitary current in the circuit according to two different connections. The voltage on the connection node is measured, which corresponds to the impedance. The DM circuit connection is made by connecting two different phases while for the CM impedance the connection is made between the machine housing and the three phases in short-circuit. *Fig. 3-44* shows the schematic to obtain the two modal impedances. The simulation results for both case study machines and for both propagation modes are shown in *Fig. 3-45*. The impedance curves clearly differentiate both machines, where higher resonant amplitudes are obtained for the e-PS machine. The amplitude of the DM impedances over their inductive band presents a large variation, where the e-ACC shows higher values up to the resonant point.
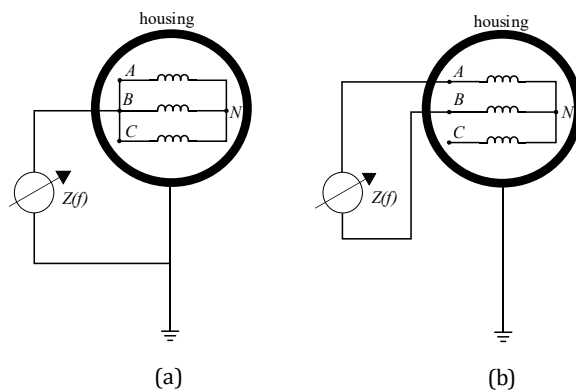
Fig. 3-44 - CM and DM connections for impedance computation, (a) CM, (b) DM

89
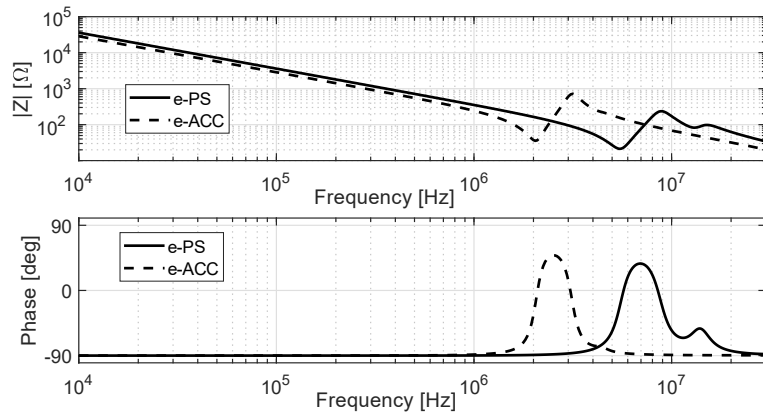
(a)
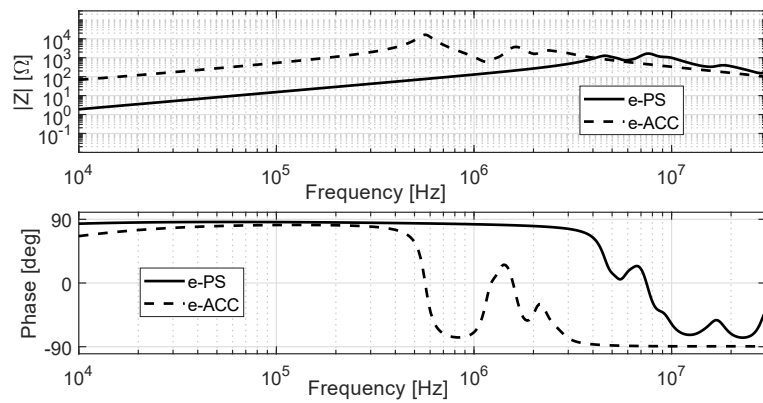
(b)

Fig. 3-45 - Simulation results, impedance absolute value and phase over frequency in the 10 kHz-30MHz range, (a) CM, (b) DM

4. Experimental measurements and model validation

This section describes the experimental procedures performed with the aim of validating the developed model. First, an overview of the impedance measurement methods and basics is provided. All the setups and specifications for both types of equipment are described in this section. Then, compensation methods to counteract the test fixture circuitry are described. Two different types of equipment were utilized to obtain experimental results, an Impedance Analyzer and a LCR meter. In addition, the effects of the machine rotor and the housing on the impedance responses are experimentally explored. Finally, the obtained impedances are interfaced with the simulation results to validate the model.

4.1. Impedance measurement principles and equipment

The impedance of every circuit element is a complex quantity composed by a real and an imaginary part. To find the impedance, at least two values need to be measured, normally current and voltage. The utilized methods to measure impedance can vary depending on several requirements such as test signal frequency, impedance level, accuracy and physical characteristics of the Device Under Test (DUT) [121]. The most common impedance measurement methods are listed below [122]:

- *Bridge method:* It consists of an impedance bridge of the Weathstone type, where one of the bride impedances corresponds to the DUT. The circuit in *Fig. 4-1 (a)* represents the basic composition of this bridge. By manually adjusting the auxiliary impedances (i.e., *Z1, Z2,* and *Z3*), the DUT impedance is found when the current through the detector is null by using $Z_{DUT} = Z1\,(Z2/Z3)$. This is the simplest of the methods and it is not normally used in modern measurement devices.

- *Resonant method:* The circuit for impedance measurement is formed by an adjustable capacitor, voltmeter *Q,* the oscillating signal and two elements reproducing the DUT impedance (i.e., R_x

and L_x). *Fig. 4-1 (b)* shows the circuit schematics. The adjustable or tuning capacitor is regulated to achieve resonance at the testing frequency. From this resonance value and knowing the value of the capacitor and of *Q,* the values of the DUT elements can be estimated. Manual methods are not used in modern devices.

- *I-V method:* The DUT impedance Z_x can be computed from direct current and voltage signals. The current is obtained by measuring the voltage on a known low valued resistance, which in practice is subtituted by a low loss transformer. Depending on the value of the impedance to be measured, variations of the circuit can be found. *Fig. 4-1 (c)* shows the I-V method basic circuit.

- *Radio Frequency (RF) I-V method:* Same principle as the simple I-V method with a variation for application at high frequencies. An impedance-matched measurement circuit together with a coaxial device is used to enable operation at higher frequencies. It can also contain variants to measure high or low impedance. *Fig. 4-1 (d)* shows the basic circuit RF I-V method for low impedance mode.

- *Network analysis method:* The method is based on the computation of incident and reflected signals. By measuring these signals the reflection coefficient (Γ) can be obtained. The coefficient is computed as the ratio of the reflected voltage signal and the incident one. If these signals are acquired, the DUT impedance Z_x can be obtained by using: $Z_x = Z_o \frac{1+\Gamma}{1-\Gamma}$, where Z_0 is the known load impedance. *Fig. 4-1 (e)* shows the basic circuit for the network analysis method.

- *Auto-balancing bridge method:* The working principle of this method is based on equating two currents, I_x and I_r. The first current (I_x) flows through the DUT and the second (I_r) flows through a large resistor (R_r). An operational amplifier is utilized to balance the currents, and the impedance of the DUT is obtained by sensing two voltages (V_x and V_r) and using the expression: $Z_x = R_r \left(\frac{V_x}{V_r}\right)$. *Fig. 4-1 (f)* shows the basic circuit for an auto-balancing bridge.

92
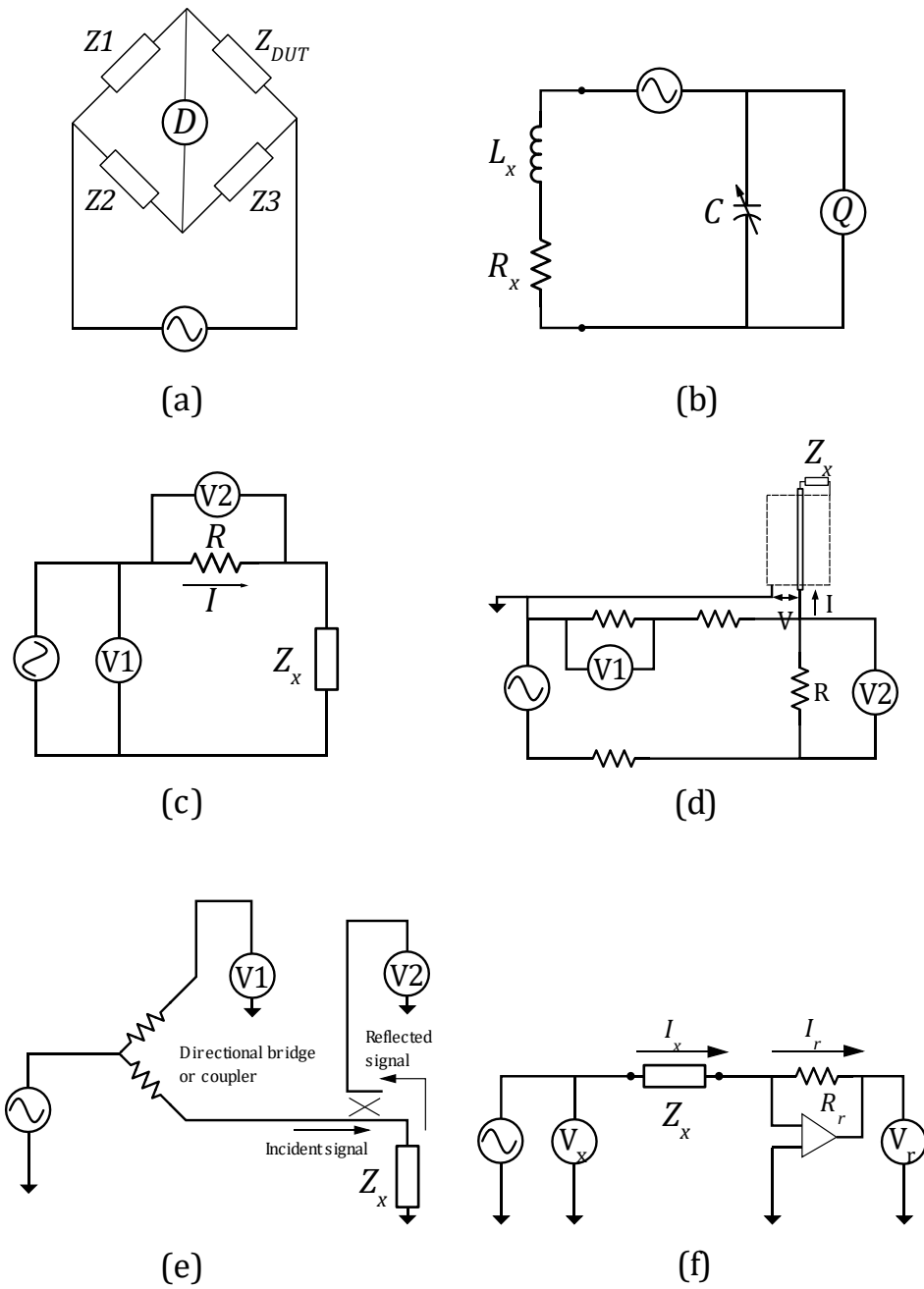
Fig. 4-1 - Impedance measurement method schematics, (a) Bridge method, (b) Resonant method, (c) I-V method, (d) RF I-V method, (e) Network analysis method, (f) Autobalancing bridge method

93

The frequency range represents the most important parameter to choose the most feasible measuring method. In this dissertation, the focus is placed around the CEs frequency band including lower frequencies corresponding to typical switching frequency values (e.g., thenths of kHz). A precision impedance analyzer (Agilent 4294A [123]) utilizing autobalancing bridge method represents the best option for accurate impedance measurement for the frequency range of interest. This equipment covers the frequency spectrum ranging from 40 Hz until 110 MHz. *Fig. 4-2* shows the front view of the Agilent 4294A precision impedance analyzer.
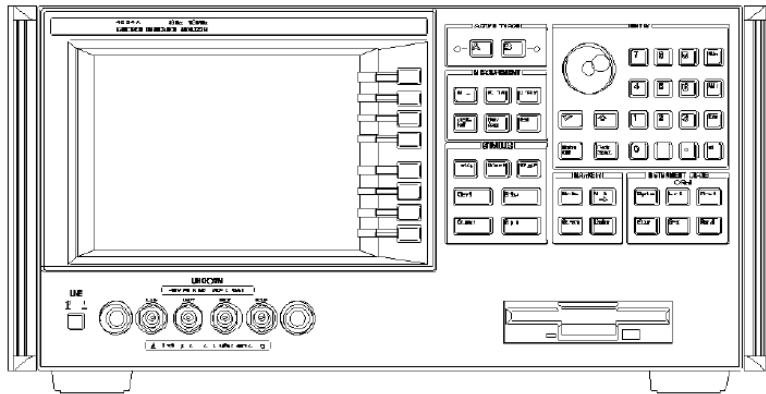
Fig. 4-2 - Agilent4294A impedance analyzer front view drawing *[123]*

The interface between the impedance analyzer and the DUT is the test fixture. This is a key element for accurate impedance determination since its constructive characteristics critically affect the measured impedance. Ideally, compensated test leads are utilized for precision measurement up to 120 MHz. The characteristics of this auxiliary device are known by the impedance analyzer manufacturer beforehand and the compensation of its effect is easy and practical [124]. However, the normative test leads were not available for precision impedance measurement and a different solution was utilized. A test fixture for lead components together with a custom cabling system was utilized to interface the DUT with the impedance analyzer [125]. The utilized cabling consists in simple solid copper conductors surrounded by electrical insulation. *Fig. 4-3* shows the

94

utilized test fixture (16047E) and a standard DM measuring setup for a motor sample.

(a)   (b)

Fig. 4-3 - (a) 16047E lead component test fixture, (b) DM measurement setup with auxiliary cabling

The options and settings of the impedance analyzer are described in [123]. *Fig. 4-4* shows the main view of the impedance

Fig. 4-4 - Impedance analyzer display view

95

analyzer display highlighting the most important information. Both axes are defined in their logarithmic mode. (1) shows the displayed magnitudes of both traces which are the modulus of the impedance in trace A (i.e., yellow trace) and its phase in trace B (i.e., blue trace). In (2) the definition of the axis divisions is provided. In (3) the marker reading is shown and in (4), (5) and (6), the characteristics of the oscillator are displayed. From these last three boxes it is possible to read the initial frequency (4), the amplitude of the sinusoidal sweep (5) and the end frequency (6).

Besides utilizing an impedance analyzer, which is the best solution in the considered frequency range, a different type of equipment was utilized for further validating the machine model. A LCR meter with frequency range 20 Hz – 1 MHz (BK precision 895 [126]) was available to perform the double check even if only frequencies up to 1MHz were available. The auto-balancing bridge method is utilized for this device as well. *Fig. 4-6* shows the front view of the utilized LCR meter.
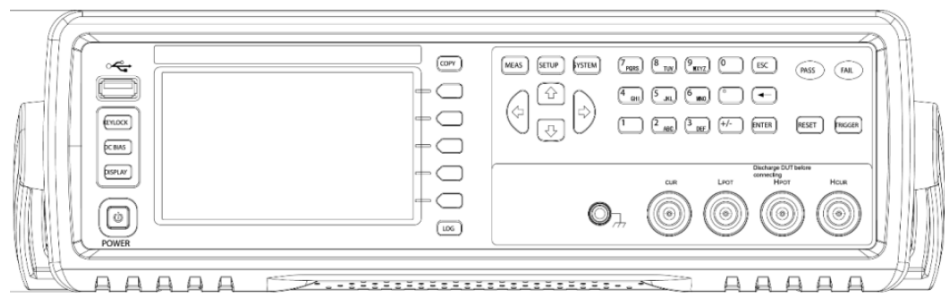
Fig. 4-5 – BK precision 895 LCR meter front view drawing *[126]*

The utilized test fixture for the LCR meter consists of two 4-wired Kelvin clips. The display of the utilized LCR meter is shown in Fig. *4-6*, where (1) shows the oscillator level, the frequency of evaluation and the selected notation, (2) shows the range mode, DC bias level and the speed of measurement, and (3) displays the main results in terms of impedance absolute value and phase.

96
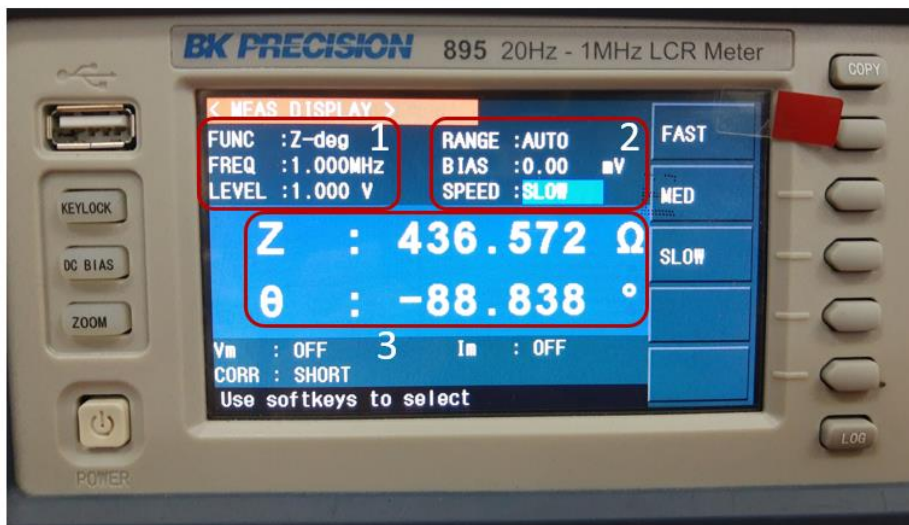
Fig. 4-6 - LCR meter display view

4.2.   Compensation methods

In physical real-world devices, it is common to assume that some error will be present while performing impedance measurement. Some error sources are related to instrument inaccuracies, noise, and residuals in the test fixture and cables. Instrument inaccuracies are corrected by carrying on periodical calibration of the instrument. This is normally done by the equipment manufacturer or associated companies in periods that can range from several months to several years (recommended period is once a year for Agilent4294A). The calibration plane of auto-balancing bridge instruments is at the BNC connectors. To reduce the uncertainty introduced by residuals in the test fixture and cables, the usage of compensation methods is required. The compensation is done by the user before every impedance measurement if the test fixture setup and cabling are modified. *Fig. 4-7* shows a typical configuration for impedance measurement highlighting the methods for error reduction.

97

Instrument callibration plane *Setup compensation plane*

Impedance Analyzer
or
LCR meter

DUT

Test fixture + cabling
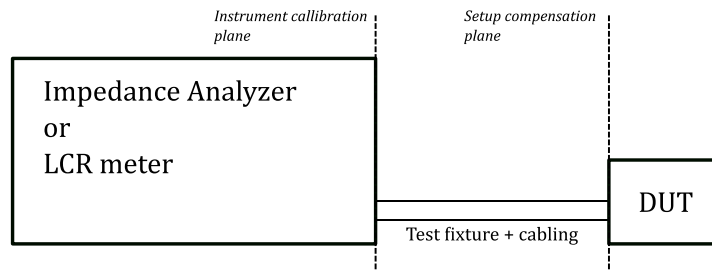
Fig. 4-7 - Error compensation planes for an impedance measurement setup

Three different types of calibration are normally considered for impedance measurement. The first one is called offset correction and it is only performed if single parasitics (i.e., only capacitance or inductance) are measured. The second method is called open/short compensation, which is the most popular compensation technique for low/middle frequency impedance measurement. It is performed by connecting the cable terminals in two different configurations, in open-circuit and shortcircuited. By performing this compensation all the parasitics in the test fixture and cabling devices are measured and taken into account when measuring the DUT. The third method for compensation is called open/short/load. It is the most complete compensation method and typically required for middle/high frequency measurements. This is strictly required when a custom test fixture is utilized. However, a known load over a broad frequency range with standard connections is required to perform such compensation. This is a critical requirement since this compensation load is not always available. In this dissertation, only open/short compensation is utilized due to the absence of a known load within the considered frequency range.

The compensation method utilized in this dissertation is tested to confirm the validity of the results. *Fig. 4-8* shows the differences between a DUT measured with and without applying compensation methods. From the figure it is possible to observe the most affected frequency region by the fixture and cabling parasitics. The frequency

98

band ranging from 10 kHz until 10 MHz it is barely affected by this parasitics and the compensation method extends the accuracy up to approximately 30 MHz. Thus, it is possible to conclude that the open/short compensation provides enough error minimization in the range 10 kHz – 30 MHz.
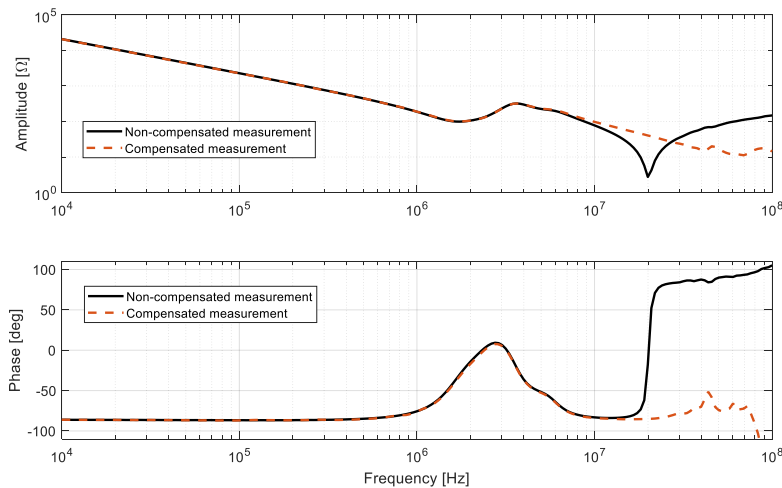
Fig. 4-8 - Open/short compensation differences for the measurement of the CM impedance of the e-ACC machine

4.3.　　Impedance analyzer measurement

This section describes the different configurations and results for the impedance analyzer broadband impedance measurement. The two case study machines were studied experimentally with the same kind of measurement equipment and setup. *Fig. 4-9* shows the two physical motors that are utilized for model validation. The connection between the motor terminals and the cabling system of the impedance analyzer is customized to properly access the machine terminals. These connections must ensure a stable connection in both electrical and mechanical terms. If the contact between the connectors and the machine terminals is not stable, the conditions in which the compensation is performed can vary and a new open/short compensation is required. *Fig. 4-10* shows the machine terminal interface for both case study machines.

99
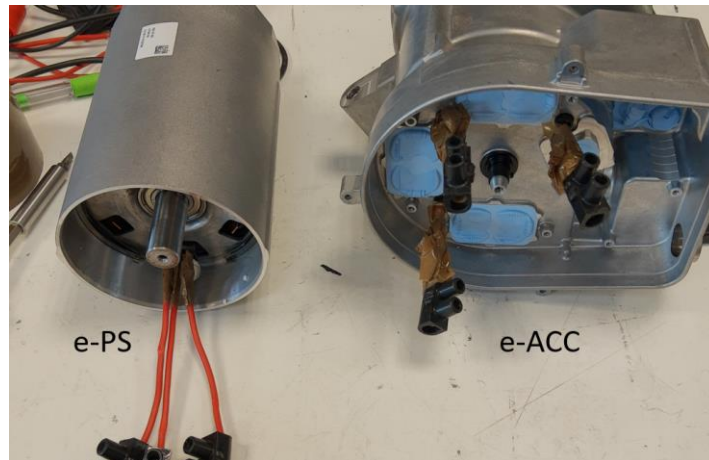
Fig. 4-9 - e-PS and e-ACC machines physical samples

(a)   (b)

Fig. 4-10 - Machine terminal interface detail, (a) e-PS, (b) e-ACC

The connections in both propagation modes are built according to Fig. *3-44*, where the connection for the CM is made between the three phases in short circuit and a grounding point, while the connection for the DM is made between two phases. Auxiliary cabling is utilized to connect the 16047E test fixture with the machine terminal interface. The effect of the parasitics of the auxiliary cabling is compensated as explained in previous sections. Fig. 4-11 shows the auxiliary cabling for

the CM connection in the e-ACC machine. The connection for the DM is simple, with only one section of cables between the test fixture and the machine terminal interface. *Fig. 4-12* the DM auxiliary cabling and the full setup for impedance measurement including the impedance analyzer, the test fixture, auxiliary cabling, motor terminal interface and DUT.
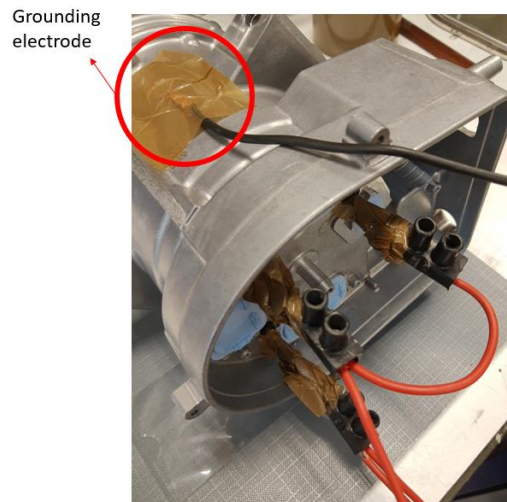
Fig. 4-11 - Auxiliary cabling connection for the CM in the e-ACC machine
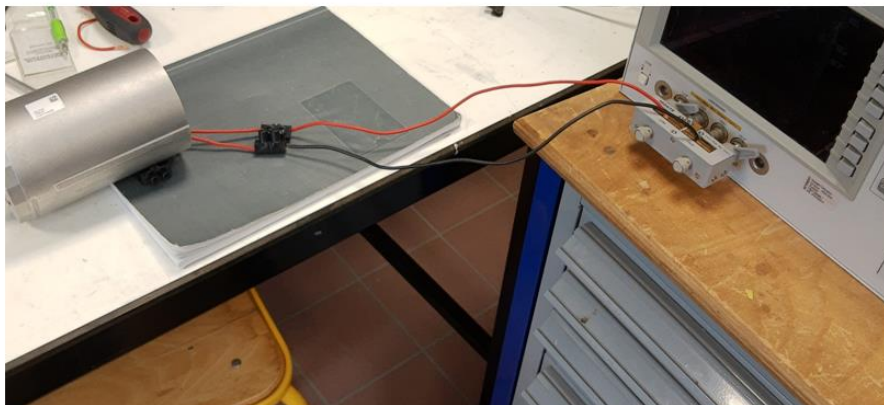
Fig. 4-12 - Full setup including 16047E test fixture, auxiliary cabling, motor terminal interface and e- PS machine for the DM connection

Fig. 4-13 shows the CM and DM measurement results for both machines in the 10 kHz – 100 MHz frequency range. The DM measurement is performed between two arbitrary phases. The parasitics of the auxiliary cabling affect the measurement starting from around 30 MHz even if open/short compensation is performed. For further accuracy, a different type of test fixture must be used, or open/short/load compensation must be done with a valid constant load. However, the resonant points are properly mapped, which represents a valid foundation for model validation together with the impedance amplitudes over the whole frequency range. The selected settings for impedance measurement are shown in TABLE 4-I.

(a)

(b)
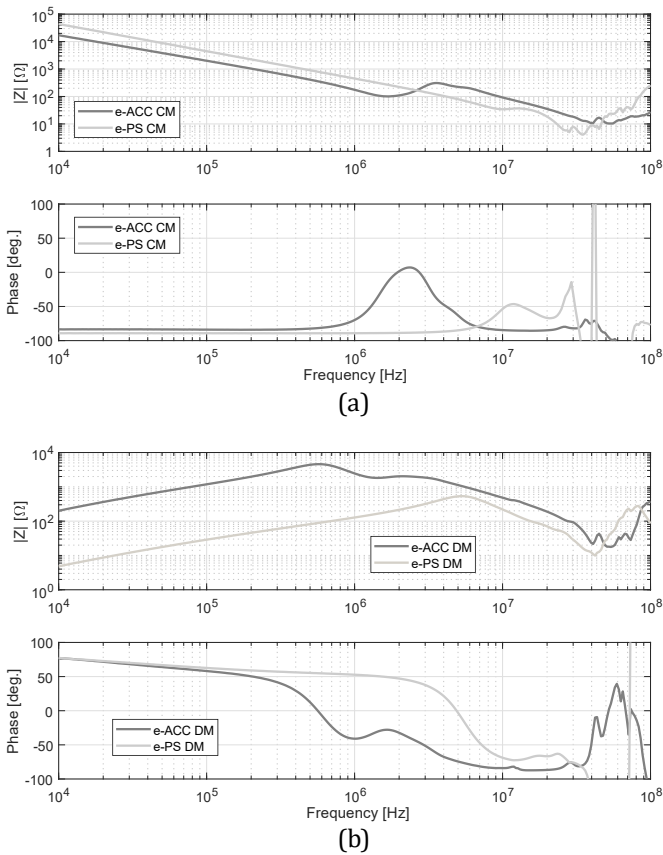
Fig. 4-13 - CM and DM measurement for both case study machines, (a) CM, (b) DM

102

AGILENT4294A impedance analyzer settings	
Measure parameter	IMPEDANCE MAG PHASE
Adapter	NONE
Sweep type	LOG FREQ
Number of points	300
OSC level	500 mV
DC Bias	OFF (0V)
Band Width	1
Trace A format (|Z|)	LOG
Trace B format (φ)	LINEAR

The effect of the grounding point location on the CM impedance is experimentally studied. The e-ACC machine stator is utilized to perform this study since it allows to better define the position of the grounding points, which are defined along the axial and circumferential axis of the stator. Fig. *4-14* shows the grounding point position and Fig. *4-15* presents the results of the study. From the study results it is possible to conclude that the grounding position does not affect the CM impedance measurement in the considered frequency range for both studied machines.

Fig. 4-14 - Grounding point locations in e-ACC stator
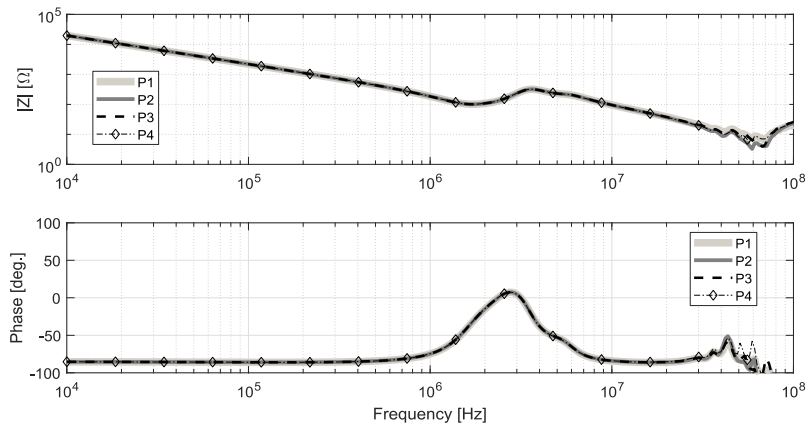
Fig. 4-15 - Grounding point location influence on the CM impedance curves

The DM impedance curves shown in *Fig. 4-13* were obtained for an arbitrary phase combination. A number was assigned to each motor terminal and three different measurements were performed for each phase combination. These measurements were performed at a fixed rotor position. *Fig. 4-16* shows the results from the DM measurement in the three different phase combinations, where it is possible to observe the differences between the impedance curves. These differences are due to the rotor position as it will be demonstrated in following sections.
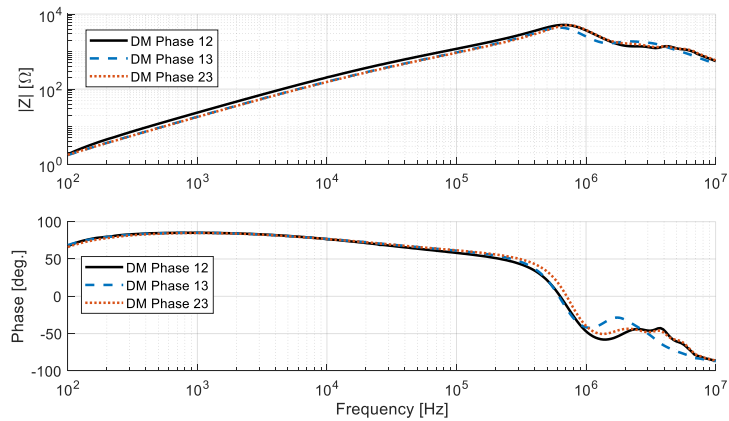
Fig. 4-16 - DM impedance measurement for different phase combinations

104

4.4. LCR meter measurement

This subsection describes the impedance measurement of the e-PS machine by utilizing a LCR meter (BK precision 895) up to 1 MHz. The measurement is performed to double check the impedance analyzer measurement by using a different equipment and measurement setup. The e-ACC machine was not available during the time window in which the LCR meter was utilized and thus, only one machine is used for the double validation.

Fig. 4-17 shows the CM and DM measurement setups where the LCR meter, the four-wired kelvin clamps, the auxiliary cabling and the DUT can be observed. The blue structures serve as a stand to ensure the good connectivity between the clamps and the cabling. The position of the clamps and the length of the auxiliary cabling do not influence the measurement in the considered frequency range. *Fig. 4-18* shows the comparison between the impedance analyzer and LCR meter measurement results. The impedance curves closely match for both modes up to the LCR meter frequency limit. Unfortunately, resonant peaks cannot be double checked because they are located out of the LCR meter frequency range.
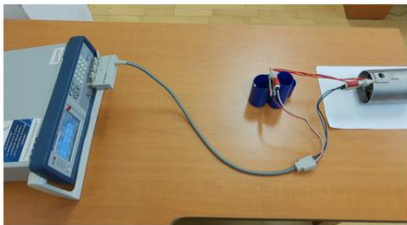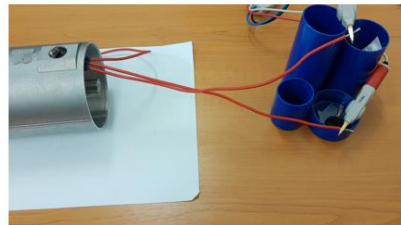
| (a) | (b) |

Fig. 4-17 - LCR meter measuring setup, (a) CM, (b) DM
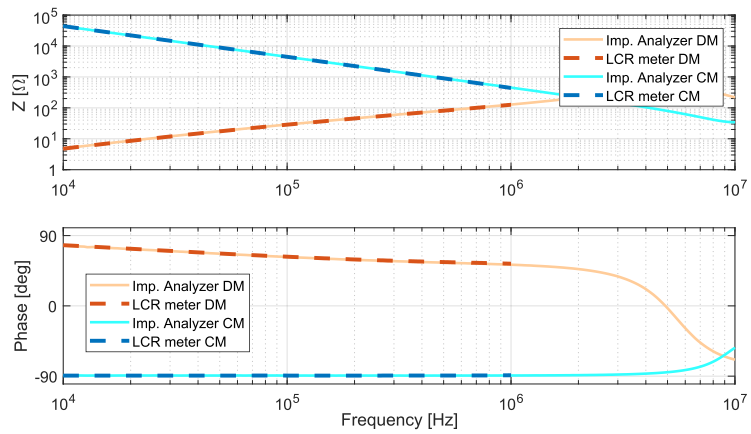
Fig. 4-18 - LCR meter vs Impedance analyzer mesurement results

4.5.   Housing and rotor insertion influence

This subsection is aimed to experimentally study the effect of the housing and the rotor insertion on the high-frequency impedance response. The e-ACC machine was utilized since it was the only one that could be disassembled and assembled in a feasible manner. Three different samples are defined as shown in *Fig. 4-19.* The first sample
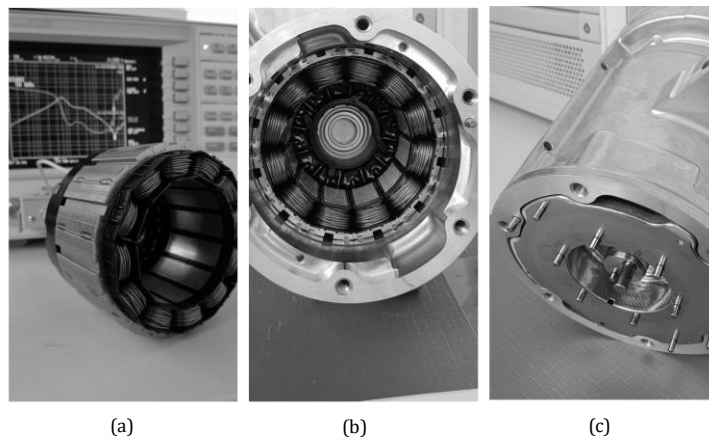
Fig. 4-19 - e-ACC motor samples for housing and rotor insertion influence study, (a) machine stator, (b) stator inserted in housing, (c) full machine

consist of the stator without rotor and housing. The second sample is built by inserting the same stator in a housing structure and the third sample includes the same stator and housing with the rotor and shaft inserted in the full structure. The measurement is performed by using an impedance analyzer.

Fig. 4-20 shows the impedance curve comparison between the different samples. The CM curve shows a slight difference in amplitude between the samples with and without housing. The resonant frequencies of the samples without rotor coincides, while the sample with rotor shows a shift of the resonance towards higher frequencies.
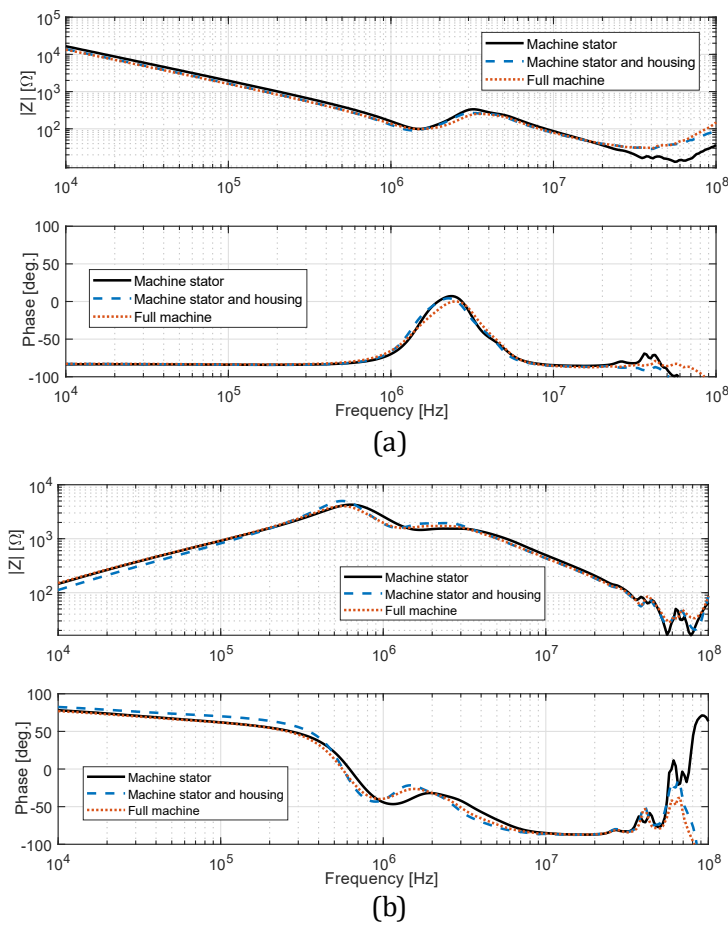
Fig. 4-20 - High-frequency impedance curve comparison between e-ACC machine samples with different constuctive features, (a) CM, (b) DM

Regarding the DM curves, a small difference in amplitude is observed for the sample with housing and without rotor in the lower frequency range (i.e., between 10 kHz and 200 kHz). The resonant frequency is slightly affected by the housing since the machine stator sample presents a minor shift of the resonant and antiresonant frequency points. The main conclusion of the comparison is that the housing and the rotor do not have a critical impact on the impedance response. Thus, the machine stator can be considered as the main contributor to the DM and CM high-frequency impedance curves for the machine under study within the considered frequency range.

4.6.   Rotor position influence

This subsection analyses experimentally the influence of the rotor position on the DM high-frequency impedance curves. As explained in Chapter 3, subsection 2.2, the DC field originated in the PMs excites the stator iron even in standstill conditions. If the rotor d-axis is aligned with the coils of a certain phase, the iron surrounding the slots of that coils is more saturated than for other phases. This will affect the low frequency relative permeability ($\mu_{r,DC}$) and thus, the RL parameters that shape the impedance curves. The study is performed for the e-ACC machine since the effect of the curve variation is more visible than for the e-PS motor.

The test is performed by changing the position of the rotor while measuring the DM impedance between different phase combinations. The rotor of the e-ACC machine is composed by 8 poles, which indicates that the d-axis of the rotor will be aligned with a single coil every 45 degree. It would be enough to sweep the rotor 45 degree to have the full signal periodicity. However, the rotor is spined 90 degree from its initial position in intervals of 15 degree. This is done to extend the data range and to not rely on a single period. The phases in the physical machine are defined arbitrarily as explained in section 4.3. The rotor axis is marked together with the different position angles in the stator. The considered rotor positions are shown in Fig. *4-21*. Note that the location of the rotor is approximated since accurate rotation cannot be achieved by using conventional tools. In addition, the connection of phases to perform the DM impedance measurement will create increased cogging torque, which hinders the positioning at some angles.
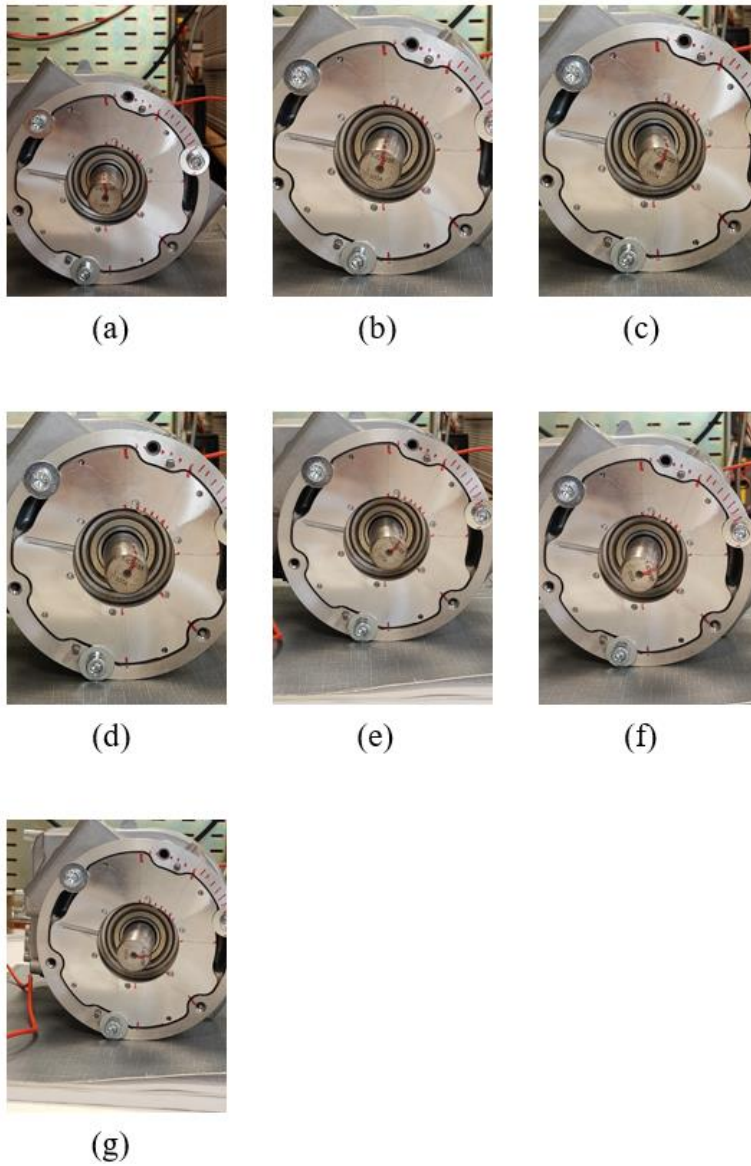
Fig. 4-21 - Considered rotor positions to study its influence on the DM impedance curves, (a) 0º, (b) 15 °, (c) 30 °, (d) 45 °, (e) 60 °, (f) 75 °, (g) 90 °

Fig. 4-22, *Fig. 4-24* and *Fig. 4-23* show the DM impedance measurement results for different phase combinations and angle

positions. *TABLE 4-II* shows the numerical values of the impedance absolute value at 10 kHz for all phase combinations and rotor positions. The figures and the table clearly show an impedance amplitude difference between different rotor positions. This amplitude shift disappears starting from the resonance point at around 560 kHz, which is the same for every phase combination. The different traces corresponding to the different rotor positions are grouped around two different impedance amplitudes, one of them higher than the other. The trace clustering can be better observed in the zoomed-in details provided in the figures. Rotor positions having higher impedance values are shifted 45 mechanical degrees (i.e., 0, 45 and 90 degree for phases 1 and 2, 15 and 60 degree for phases 1 and 3, and 30 and 75 for phases 2 and 3).
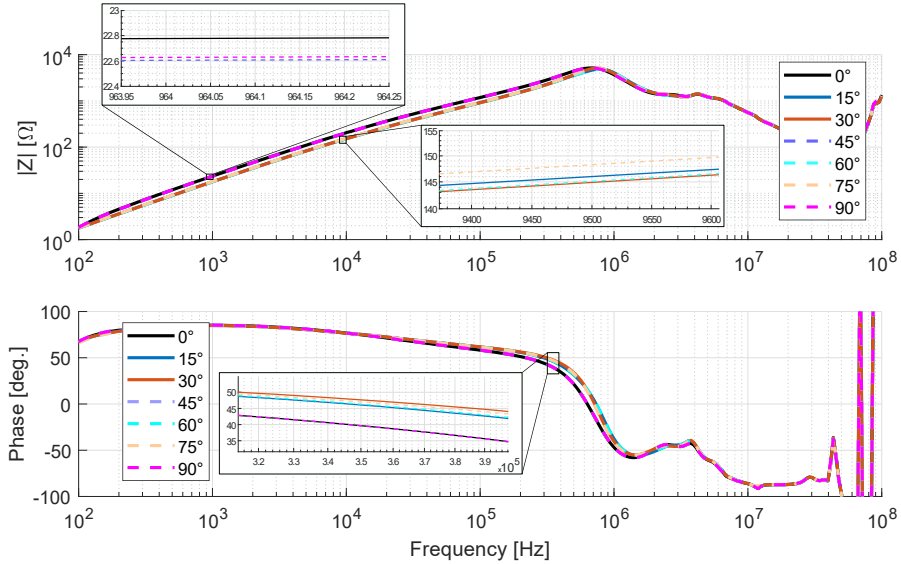
Fig. 4-22 - DM impedance curves between phases 1 and 2 for different rotor positions.
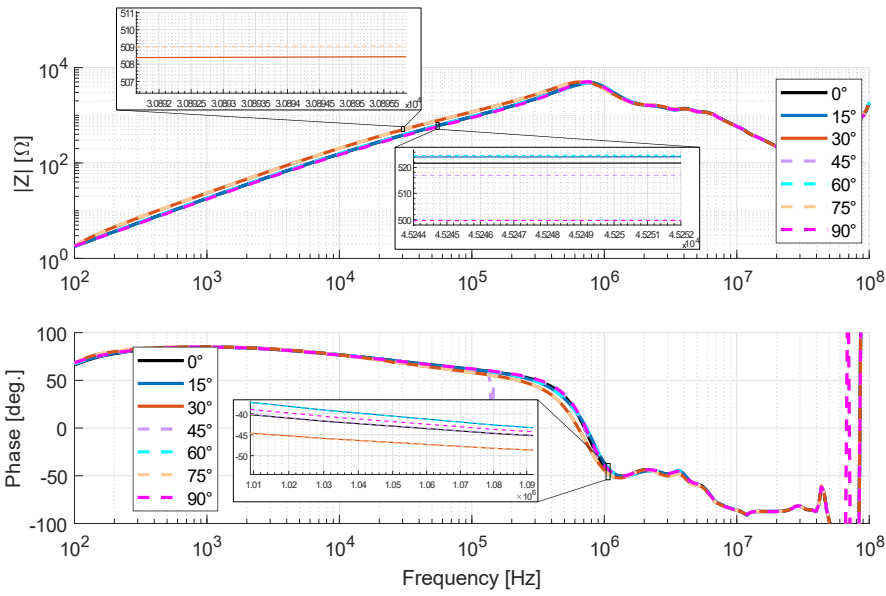
Fig. 4-24 - DM impedance curves between phases 1 and 3 for different rotor positions.
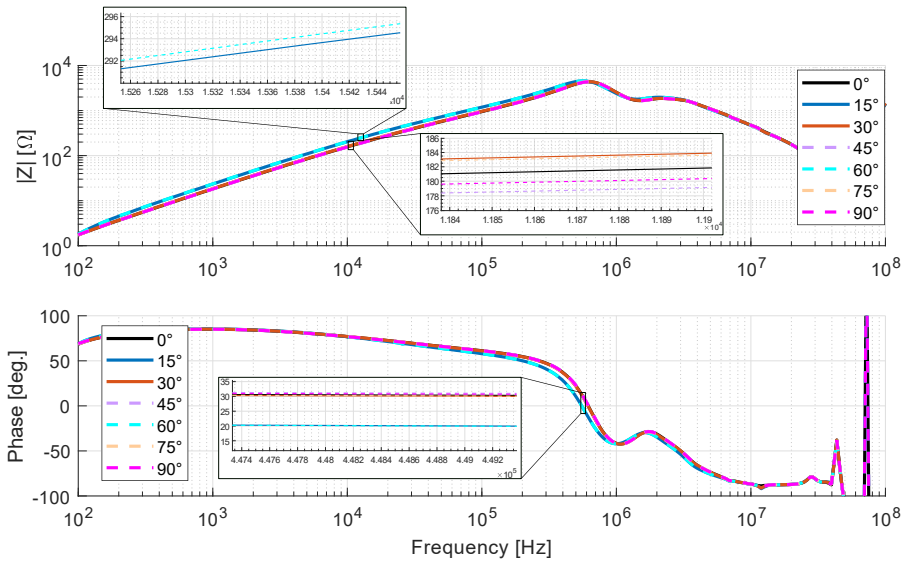
Fig. 4-23 - DM impedance curves between phases 2 and 3 for different rotor positions.

TABLE 4-II – Measured impedance values for different rotor positions and phase connections at 10 kHz

Rotor position [deg.]	Ph12 $|Z|$ [Ω]	Ph13 $|Z|$ [Ω]	Ph23 $|Z|$ [Ω]
0	208.58	159.26	157.08
15	155.03	207.54	157.75
30	153.83	161.12	207.40
45	207.56	156.83	155.84
60	153.94	208.61	157.91
75	157.50	160.93	207.89
90	207.86	157.91	150.97

The 45 mechanical degree shift between higher and lower impedance values in the frequency band before the resonant peak can be physically explained taking into account the machine geometry and the stator winding connection. The geometry description of the concentrated winding for the different phases is shown in *Fig. 4-25*. The initial position in the simulation is set when the d-axis in the rotor is allingned with coil phase A ($\theta = 0°$). *Fig. 4-25* shows the B-field distribution for different rotor positions in the e-ACC machine. The plots for rotor positions ranging from 45 to 90 degree periodically match the observed positions in *Fig. 4-25.*

Since the RL parameters depend on the low-frequency relative permeability, the B-field in the different coil teeth influences the high-frequency impedance. The field is evaluated for each rotor position and for one tooth in each phase. The field sample is taken in the middle of the tooth. Note that the B-field distribution is the same for all the coils of the same phase for a single rotor position. *Fig. 4-26 (a)* shows the absolute value of the B-field for a tooth belonging to the three different phases and for different rotor positions between the initial and a 90 degrees relative position. The DM impedance curves are obtained for different phase connections, with current entering a certain pase and going out trough a different one. Thus, the B-field in different phases must be considered simultaneously to determine the rotor position influence. *Fig. 4-26 (b)* shows the average B-field absolute value experienced by a current flowing through two different phases. The expression to compute this average B-field is given by:
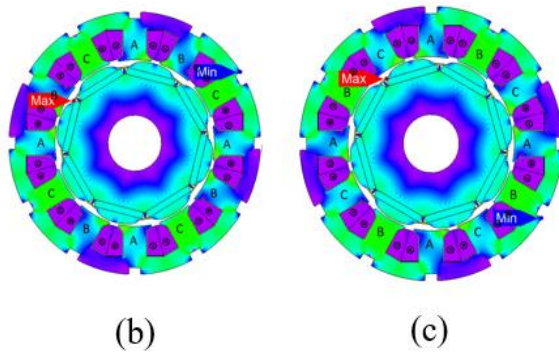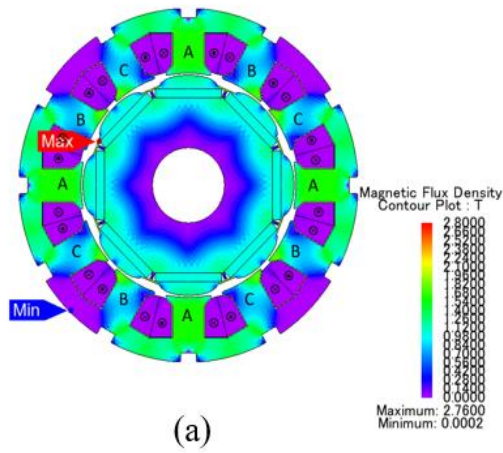
Fig. 4-25 - B-field contour plot and coil distribution for different rotor positions, (a) intial position ($\theta = 0°$), (b) ($\theta = 15°$), (c) ($\theta = 30°$)

$$B_{avg,DM} = \frac{B_{phA} + B_{phB}}{2} \qquad \text{(4-1)}$$

where $B_{avg,DM}$ is the average B-field experienced by the coils involved in a two-phase connection, and B_{phA} and B_{phB} are the fields corresponding to a coil of the phase where current enters and exits the winding respectively. From *Fig. 4-26 (b)* it is possible to observe peak and valley values over the considered mechanical range with a periodicity of 45 degree.

113

(a)

(b)
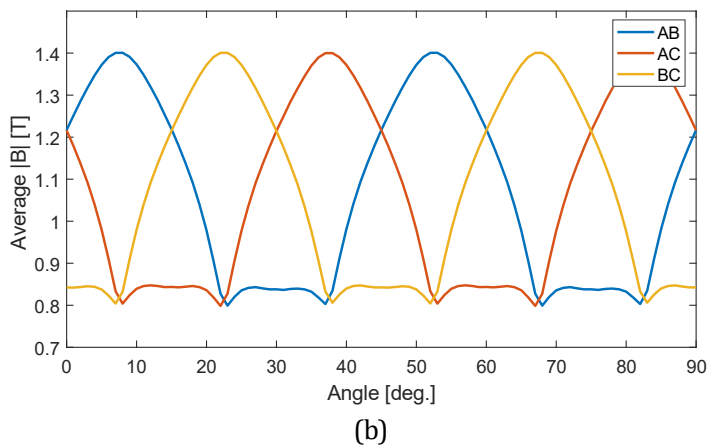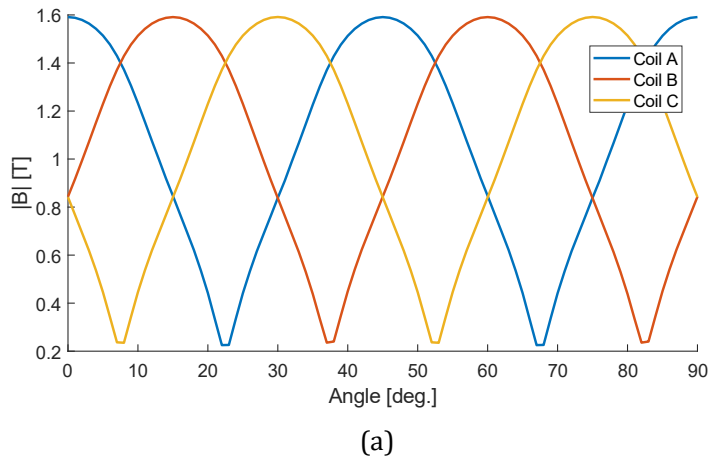
Fig. 4-26 - B-field absolute value depending on the rotor position, (a) Single coil value sample in the middle of a tooth, (b) Average value for different phase connections

The connections between phases during the measurement were done arbitrarily and thus, the correspondence between physical phases 1, 2 ,3 and geometrical phases A, B, C is random. TABLE 4-III shows the numerical values of the average B-field for different rotor positions and different phase connections. These values show the same pattern as the measured impedance, where higher impedance values were found every 45 degree. From the pattern agreement, it is possible to state that low values of the average B-field induce higher impedance amplitude values. The statement coincides with the presented deterministic

114

modelling method where the low-frequency relative permeability is estimated by using the average B-field in the stator at a fixed rotor position. Hence, for higher average B-field values the locus in the BH characteristic of the material will be closer to saturation positions and the permeability value will adopt lower values. For lower permeability values, less inductance and thus, less total impedance. This is true assuming that permeability decreases for increased B-field values, which is the case for the studied machine and its magnetic characteristics. The comparison of both B-field and impedance patterns depending on the rotor position led to the conclusion that the connection between phases AB corresponds to phases 13 in the measured physical machine, and that phases AC and BC correspond to phases 23 and 12 respectively. Another conclusion that can be drafted from these results is that the DM impedance in PMSMs will vary depending on the phase connection and the rotor position even if the measurement is performed in standstill conditions.

TABLE 4-III - Average B-field values for different phase connections

Rotor position [deg.]	Avg. |B| PhAB [T]	Avg. |B| PhAC [T]	Avg. |B| PhBC [T]
0	1.217	1.216	0.842
15	1.219	0.834	1.216
30	0.838	1.215	1.214
45	1.217	1.216	0.842
60	1.219	0.844	1.216
75	0.838	1.215	1.214
90	1.217	1.216	0.842

Regarding the CM impedance curves, the effect of the rotor position is negligible. This can be derived from the results of the average B-field absolute value when all three phases are shortcircuited. *Fig. 4-27* shows the average B-field variation for the CM connection for different rotor positions. The peak-to-peak value for the average B-field is less than 0.1 T versus the 0.4 T of the DM. In addition, the CM curves are mainly capacitive, and less influenced by the RL parameters which depend on the low frequency relative permeability. *Fig. 4-28* shows the CM curve for different rotor positions where it is possible to identify the neglegible variation of both amplitude and phase.
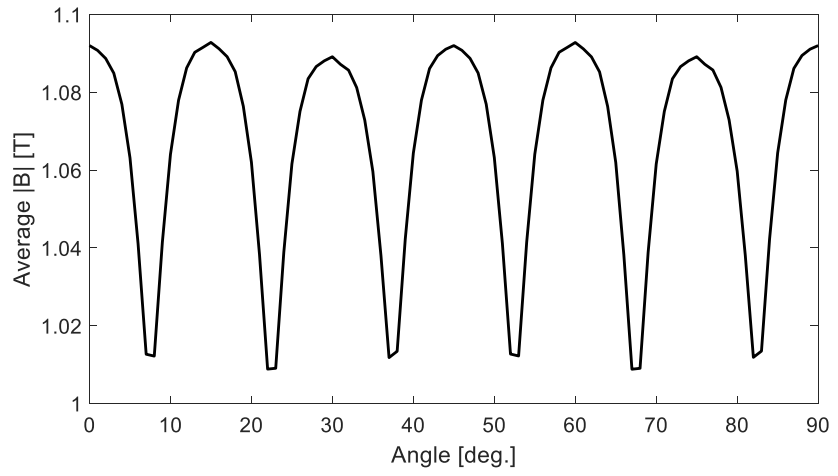
Fig. 4-27 - Average B-field absolute value in CM connection for different rotor positions
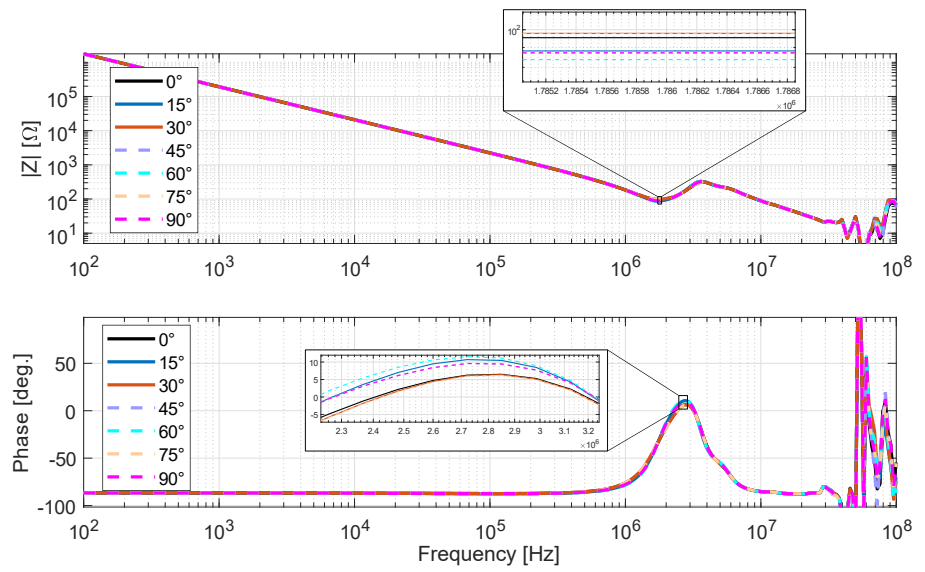
Fig. 4-28 - CM impedance for different rotor positions.

116

4.7.   Model validation results

This subsection compares the experimental and simulation results for both case study machines and both propagation modes. The full machine impedance measurement including housing and rotor are utilized for validation. The rotor position and the phase combination are chosen arbitratily. The maximum frequency for validation is set at 30 MHz since the measurement accuracy starts to decrease from that frequency point on. Both machines were tested by utilizing an impedance analyzer (Agilent4294A), and the same test fixture and auxiliary cabling. The tests were performed in the same laboratory and by using the same impedance analyzer settings for both machines. Fig. *4-29* and Fig*. 4-30* show the result comparison for the e-ACC and e-PS machine respectively.

The first conclusion that can be drafted from the comparison is that the simulated impedances match the general trend for both machines and both modes. This can be justified by the number of resonant points, and the inductive and capacitive behaviour over the different frequency bands. Another inmediate observation is the simulation lack of damping in the resonant points, which means that the resonances are sharper in the simulation than for the experimental measurements. In addition, some amplitude differences in the lower frequency bands (i.e., before the resonant points) can be easily observed for both machines and modes. These differences are more obvious in the DM than in the CM. The resonant points in the DM curves are closely matched while for the CM a disagreement is observed. The disparity is better observed in the e-PS CM curve. The antiresonance point in the e-PS machine DM curve is highly damped and not visible in the experimental results. TABLE 4-IV provides quantitative data about resonance differences in terms of frequency and amplitude. The reference points taken in the table are highlighted in Fig. *4-29* and Fig. *4-30*. The causes of the observed inaccuracies will be closely analyzed in following sections.

In spite of the evident inaccuracies, the presented modelling method manages to map the impedance response trends and their resonant points. In addition, by observing the impedance differences between the two different machines, the simulation results allow to distinguish between the two machines by just observing the impedance

117

results. Thus, it is possible to state that the developed method can predict qualitative trends of the high-frequency impedance response in both propagation modes by utilizing a 2D machine cross-section, the conductor distribution within the slot, the winding connection scheme, and simple material characteristics.
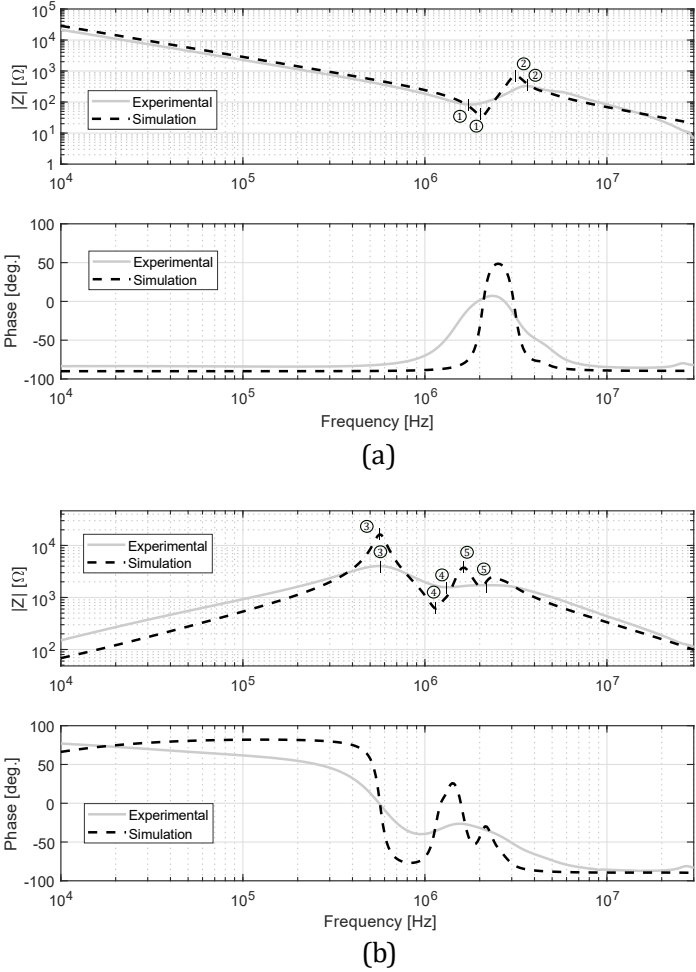
Fig. 4-29 - e-ACC machine experimental vs. simulation results, (a) CM, (b) DM
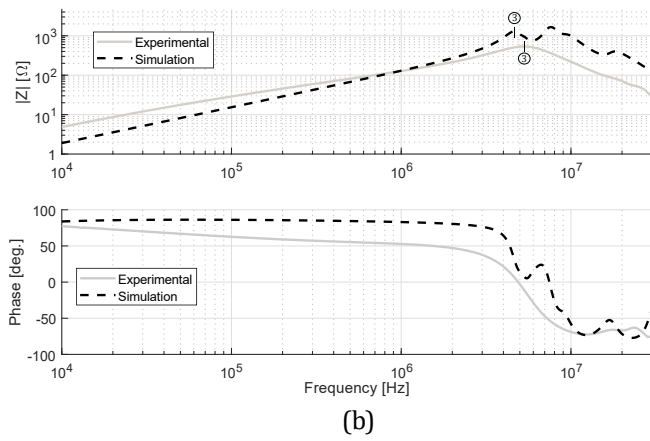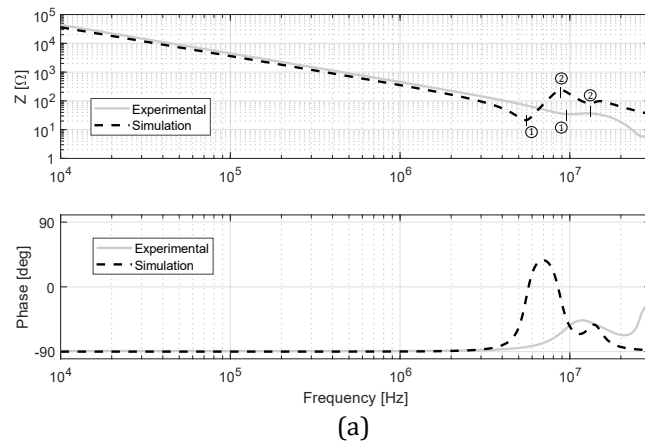
Fig. 4-30 - e-PS machine experimental vs. simulation results, (a) CM, (b) DM

TABLE 4-IV - Simulation vs. experimental resonant point data comparison

Point	Sim. amp [Ω]	Exp. amp [Ω]	Sim. freq [Hz]	Sim. freq [Hz]
e-ACC				
1	35.5	83.5	2.00E+06	1.70E+06
2	686.5	330.1	3.20E+06	3.60E+06
3	15130	4024	5.62E+05	5.48E+05
4	638.4	1575	1.12E+06	1.30E+06
5	3756	1720	1.62E+06	2.23E+06
e-PS				
1	21.38	35.11	5.57E+06	8.51E+06
2	233.7	36.87	1.27E+07	9.12E+06
3	1249	534.6	4.74E+06	5.35E+06

5. Sensitivity analysis of design parameters

This chapter presents a thorough sensitivity analysis of the high-frequency impedance model presented and validated in the present dissertation. Several modelling levels are considered in the analysis. First, the direct impact of the primary parameters (RLC) is presented. Then, the winding connection effect is analyzed by utilizing a simplified model that allows to study the effect of series and parallel coil connection. In third place, the influence of the geometric parameters is studied. Finally, the effect of the material characteristics is closely analyzed. To limit the extent of the analysis, the most influent characteristics are considered and only one case study machine is utilized. The e-ACC machine is chosen for the sensitivity analysis due to the higher number of observable resonant points. The upper frequency limit is set at 10 MHz since the band 10MHz-30MHz does not provide any useful information.

5.1.   Effect of primary parameters (RLC)

This section analyzes the effect of the RLC parameters on the high-frequency impedance curves. The effect of each element is studied separately by keeping the parameters out of the study at their estimated value by using the input data described in Chapter 3. The variation is provided as percentage increments around the estimated value. The variation is set from 0% to 100% in steps of 25% of the estimated value.

5.1.1. Turn-to-ground and inter-turn capacitances

To analyze the effect of the parasitic capacitances, a distinction is made between inter-turn and turn-to-ground capacitances since they are influenced by different geometric parameters and material characteristics. Fig. *5-1* shows the impact of the variation of turn-to-ground parasitic capacitances. The CM impedance curve is more affected by this variation, since its behaviour is mostly capacitive. Two main changes are observed for the CM curve. The amplitude adopts lower values for increased turn-to-ground capacitances. In addition, both curve resonant points are shifted towards lower frequencies. For the DM curve, a shifting of the resonant point in the same direction is

observed. The amplitude in the high-frequency band after the resonance point is also affected, when the phase of the DM impedance equals to -90 degrees.

(a)

(b)
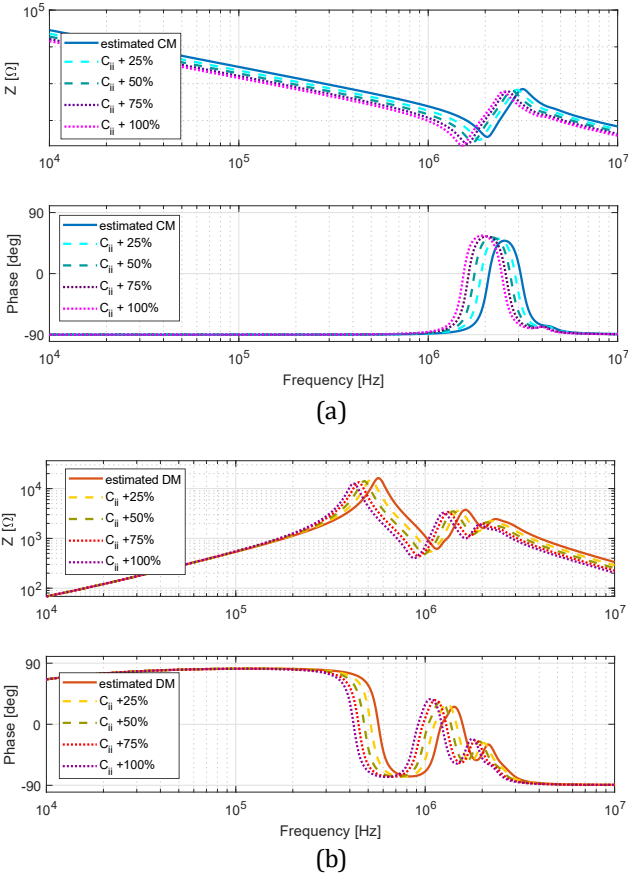
Fig. 5-1 - Impact of the variation of turn-to-ground capacitances, (a) CM, (b) DM

The effect of inter-turn parasitic capacitances is analyzed in Fig. *5-2*. The first conclusion is that their impact in the high-frequency impedance response is weaker than for the turn-to-ground capacitances. The main effect of these inter-turn terms is observed around the anti-resonance point (i.e., the second resonant point), where a light shift towards lower frequencies is observed for increased capacitance values in both modes. Moreover, the amplitude of the impedances after these resonant points slightly decreases for both

modes. From these results it is evident that the inter-turn parasitic capacitances mainly affect the impedance region after the main resonant point.
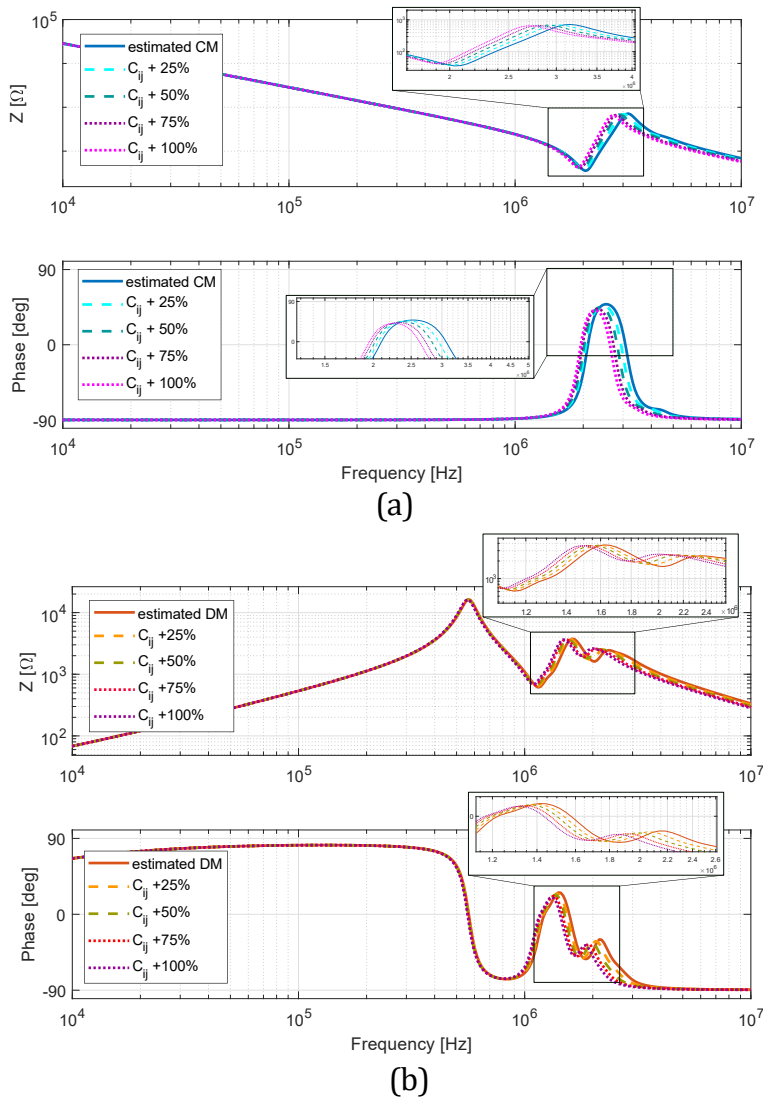
Fig. 5-2 -- Impact of the variation of inter-turn capacitances, (a) CM, (b) DM

5.1.2. Frequency dependent parameters (RL)

The variation of the two frequency dependent parameters is analyzed in this subsection. The effect of the series resistance variation is shown in *Fig. 5-3*. The resistance affects the damping of the resonant points. All amplitudes remain unchanged for the CM while a very light
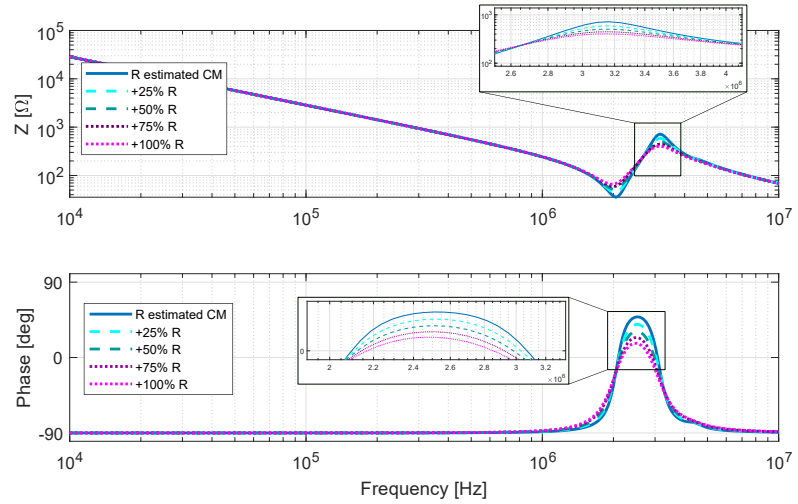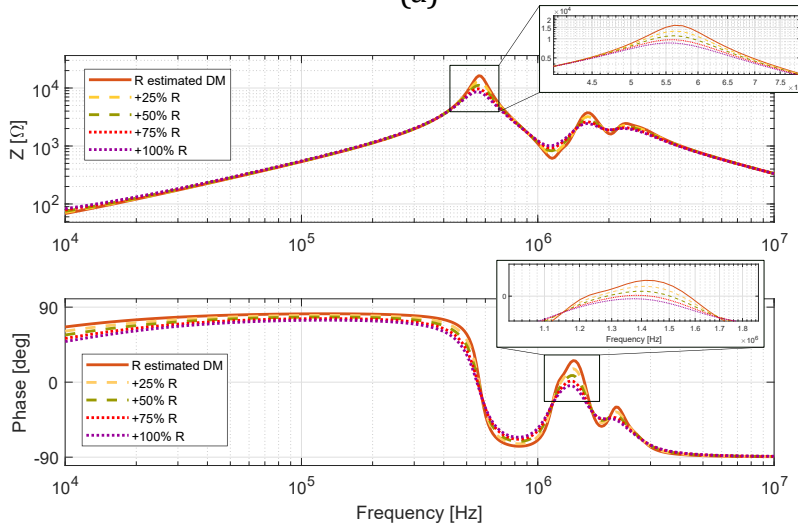
Fig. 5-3 - Impact of the variation of the series resistance, (a) CM, (b) DM

variation takes place in the beginning of the DM curve. The location of all resonant points remains unchanged.

The inductance variation is studied as variation of the series reactance. Both self- and mutual inductances are modified simultaneously. *Fig. 5-4* shows the effect of the reactance variation in both modes. The resonant points of the CM curve are shifted towards lower frequencies for increased values of reactance. The DM curve resonant points are affected similarly. The main effect of the reactance variation is observed in the DM curve amplitude, in the region before the main resonant point. For increased values of reactance, increased amplitude values of the impedance are obtained. Moreover, for increased values of reactance at constant resistance, the damping of the resonances is reduced in both CM and DM.
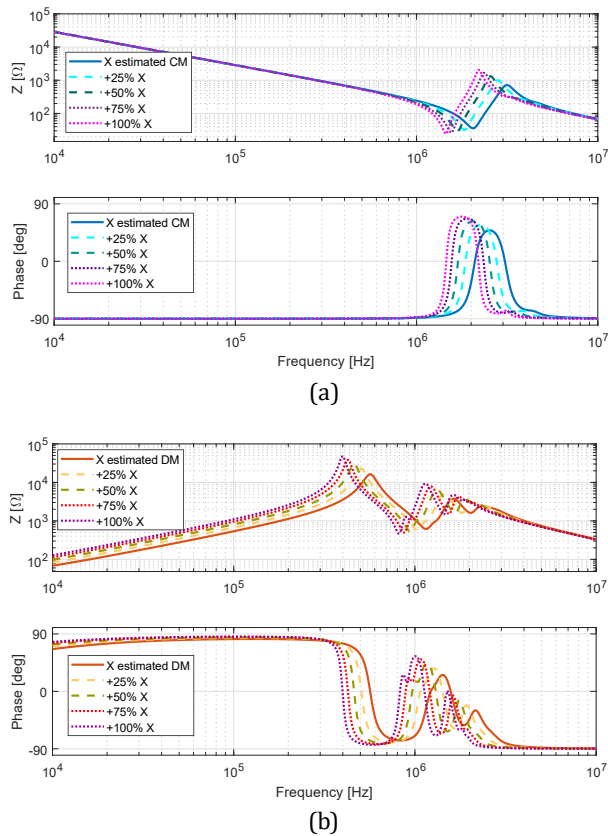
Fig. 5-4 - Impact of the variation of the series reactance, (a) CM, (b) DM

125

5.2. Effect of winding connection

The present subsection presents the detailed analysis of the winding connection influence on the high-frequency impedance response. The different coils in three-phase machines can be distributed or concentrated but, indenpendently of their constructive features, they can be connected in series or parallel. The connection defines the different paths that the input current follows. Hence, the focus is placed on the study of series and parallel connected coils. To this aim, a simplified phase sample is defined, where the effect of the connection is isolated. The utilized parameters in the equivalent circuit of the simplified connection are the same as for the full machine. *Fig. 5-5* describes the original connection of the e-ACC machine and the simplified model to isolate the effect of the connection. The connection for the CM in the simplified sample is made between the input (P1) and the reference ground, while for the DM the connection is made between the input and output (P2) points.

(a)

(b)
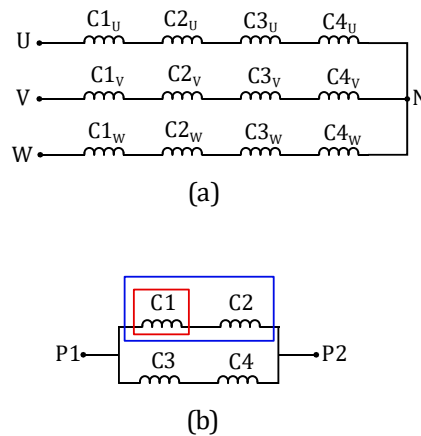
Fig. 5-5 - Different connection schematics, (a) e-ACC machine original connection, (b) simplified connection to isolate the effect or series and parallel connected coils

Fig. 5-6 shows the effect of the connection in the high-frequency impedance curves. Three different simplified connections are displayed. The first corresponds to a single coil (i.e., red square in *Fig. 5-5*) the

second represents two series connected coils (i.e., blue square in *Fig. 5-5*) and the third sample shows the connection of two series branches. It can be observed that the resonant frequencies are shifted when coils are connected in series. The phase is the same between a single branch and two parallel branches connection. The amplitude in both modes is heavily influenced by all connections. In the DM curve, the amplitude for a single branch is higher than for a parallel branch, while for the CM the amplitude decreases when a single branch and two parallel branches are compared. From the analysis of *Fig. 5-6* it is possible to conclude that the connection of the stator winding plays a key role on the high-frequency impedance curves since it affects both the amplitude and the location of the resonant points.
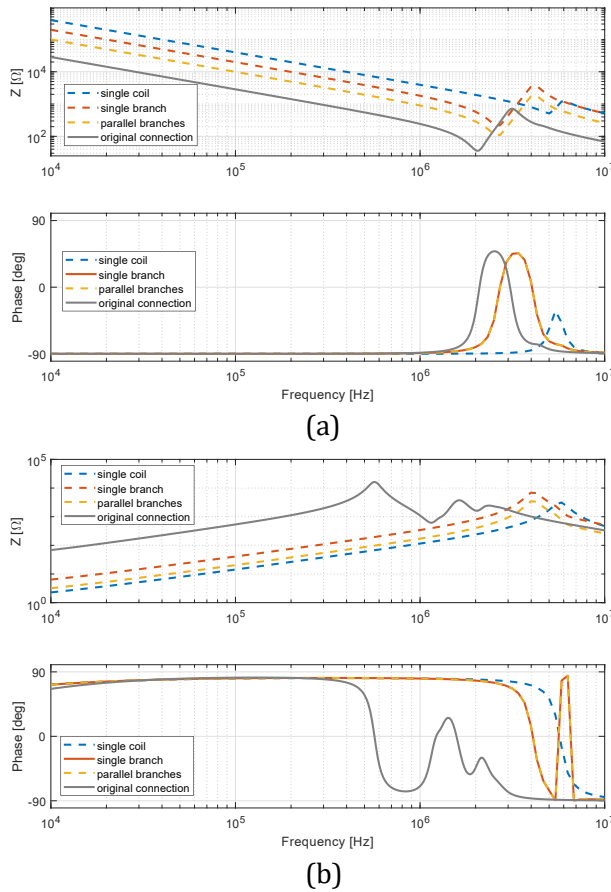
Fig. 5-6 – Impact of the winding connection in the high-frequency impedance curves, (a) CM, (b) DM

5.3.   Effect of geometrical parameters

This section analyzes the influence of geometric parameters mainly focusing on the slot inner geometry. These parameters are selected because of their direct influence in the FEM computation of the equivalent circuit parameters. Thus, the impact on the RLC parameters is analyzed together with the variation of the high-frequency impedance curves.

5.3.1. Stack length

The stack length adds or reduces the axial length of the conductors within the slots. Note that for long stack lengths it may be necessary to use more than a single lumped-pi equivalent circuit section to properly consider the wave propagation in the conductors. In the present study, only one pi-equivalent section has been considered to address the stack length variation impact on the RLC parameters and the impedance curves. In fact, the accuracy of the presented method increases for increased stack lengths since the effect of the end-winding is minimized, which is neglected in the model.

The effect of the stack length directly affects the RLC parameters proportionally.   Instead   of   directly   increase   or   reduce   them
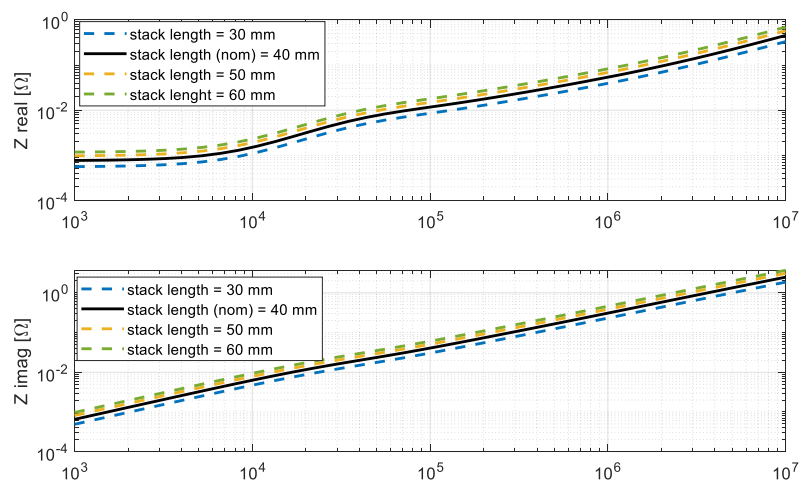
Fig. 5-7 - Stack length variation effect on a conductor self-resistance and self-reactance

128

proportionally, a double check in the FEM domain is performed. *Fig. 5-7* shows the variation of the frequency dependent parameters and TABLE 5-I shows different numerical values for turn-to-ground and inter-turn capacitances. From both Fig. *5-7* and TABLE 5-I it can be deduced that the parameters vary proportionally with the stack length.

TABLE 5-I - Stack lengh influence on parasitic capacitances

Stack length [mm]	$C_{1,1}$ [pF]	$C_{1,2}$ [pF]	$C_{28',28'}$ [pF]
30	3.13	2.47	0.01
40 (nom.)	4.18	3.29	0.011
50	5.22	4.11	0.013
60	6.27	4.93	0.016

(a)

(b)
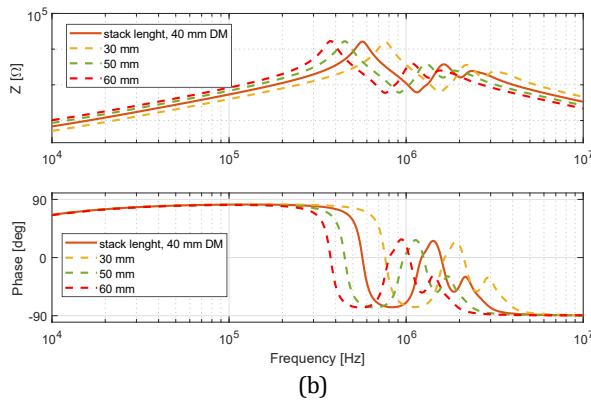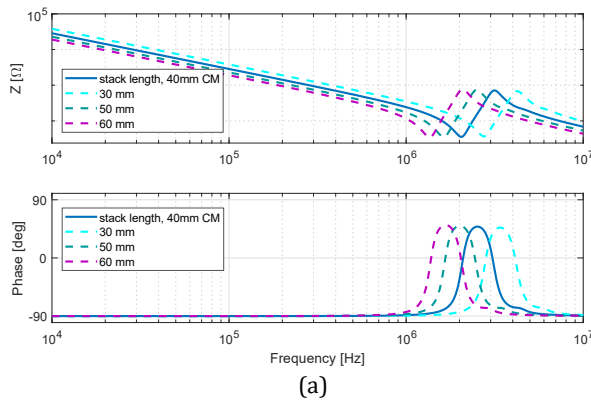
Fig. 5-8 - Impact of the variation of the stack length in the high-frequency impedance curves, (a) CM, (b) DM

129

Fig. 5-8 shows the effect of the stack length variation on the high-frequency impedance curves. The stack length heavily influences the curves in terms of amplitude and resonant point location. The damping of the resonant points does not vary since the resistance, inductance and capacitance change proportionally.

5.3.2. Conductor diameter

The conductor diameter effect is evaluated by keeping the conductor position fixed and only modifying their diameter. Three different sizes are tested by reducing the diameter of the conductors. This is done to avoid layer overlapping. *Fig. 5-9* shows the three evaluated slot geometries. The main drawback of the analysis is the non-realistic air layer that will be created between the different conductors in the slot. However, the isolated effect of the diameter variation is better observed.

(a) (b) (c)
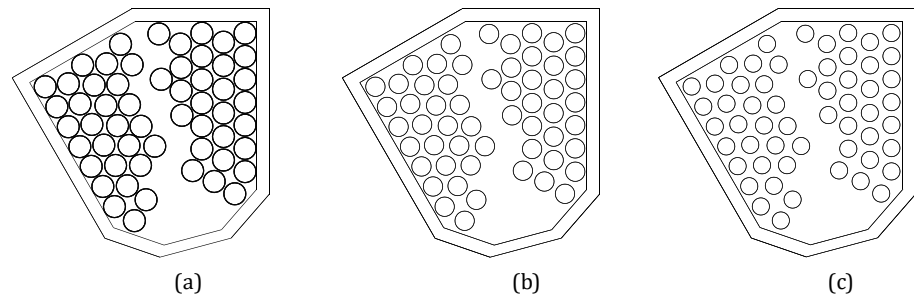
Fig. 5-9 - Three different slot geometries with different conductor diameters, (a) nominal value 1mm, (b) 0.9 mm, (c) 0.8 mm

The effect of the diameter variation on the self- and mutual impedances is shown in *Fig. 5-10*. The mutual resistances in the low frequency band (10 kHz - 100 kHz) is the most affected parameter. In the range between 100 kHz and 10 MHz the self- and mutual resistances slightly decrease for lower diameter values. Self- and mutual reactances follow similar trends, with slightly higher values for decreased diameter values. Note that the variation of the reactance is smaller in the band 10kHz – 100 kHz than in the upper region. The

130

variation in both resistance and reactance follows the expected trend. Small conductor diameters are expected to reduce the effective resistance and to increase the inductance values, which are inversely proportional to the conductor radius.
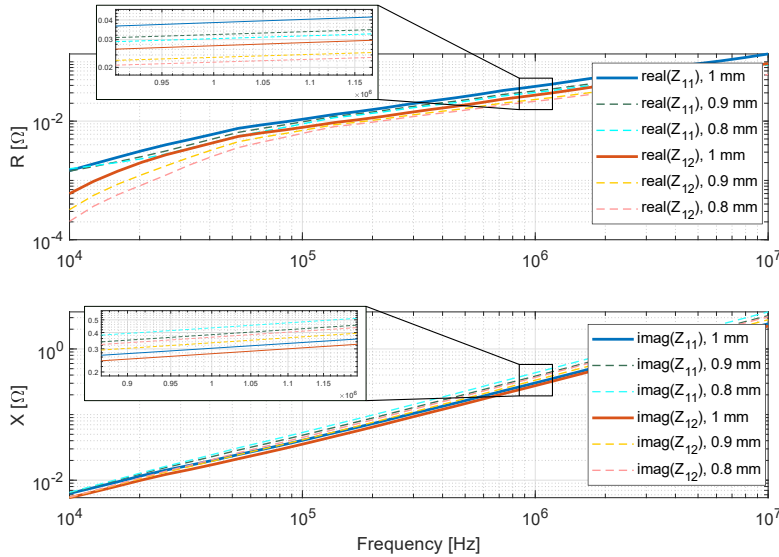
Fig. 5-10 – Conductor diameter variation effect on the self- and mutual resistances and reactances

TABLE 5-II shows the numerical values for different parasitic capacitaces and the three defined conductor diameters. The most affected parameters are the inter-turn coulpings. In addition, turn-to-ground capacitances are affected due to the increased air layer between conductor and insulation. However, the turn-to-ground couplings for conductors not directly facing the slot wall increases. This is caused by the weaker shielding effect that neighboring conductors induce on the electric field distribution.

TABLE 5-II – Conductor diameter influence on parasitic capacitances

Conductor diameter [mm]	$C_{1,1}$ [pF]	$C_{1,2}$ [pF]	$C_{28',28'}$ [pF]
1 mm	4.18	3.29	0.01
0.9 mm	2.51	1.14	0.016
0.8 mm	2.06	0.73	0.022

The effect of the conductor diameter variation on the two impedance curves is shown in *Fig. 5-11*. Both resonant points are shifted towards higher frequencies and with less damping. Regarding amplitude values, only the amplitude of the CM curve is notably affected, while the DM curve amplitude in the frequency range between 10 kHz and 400 kHz remains almost unchanged.

(a)

(b)
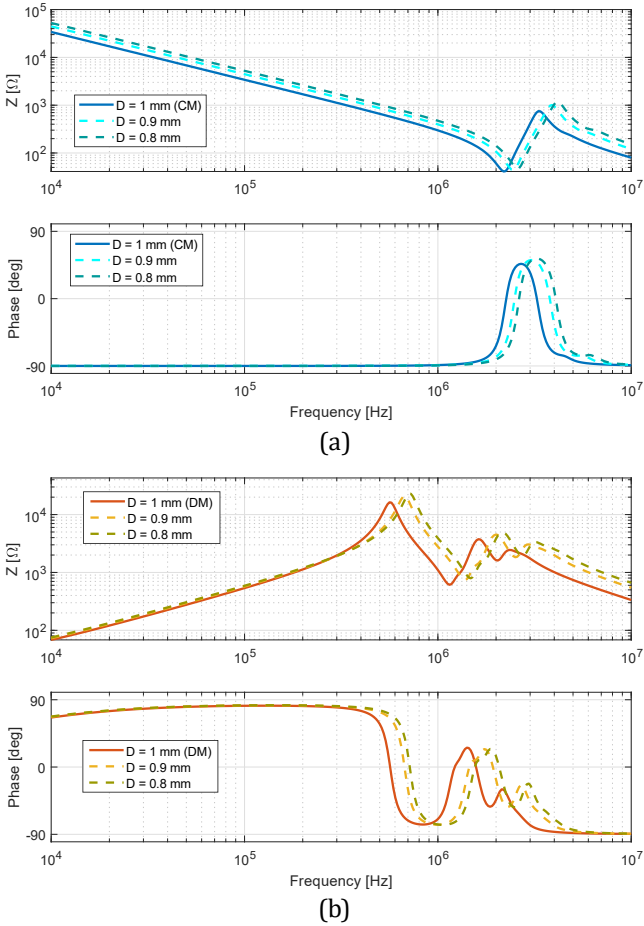
Fig. 5-11 - Impact of the variation of the conductor diameter in the high-frequency impedance curves, (a) CM, (b) DM

132

5.3.3. Insulation material thickness

The effect of the insulation material thickness mainly affects the turn-to-ground capacitances. The conductor distribution for the different insulation geometries is organized to keep the conductors in the same relative position. In this way, the inter-turn terms do not change, and the variation of the turn-to-ground capacitances is only caused by the insulation thickness. Inter-phase terms are affected since conductors from the two layers are closer to each other for increased insulation thickness. The effect on the RL parmeters is ignored in the present study. *Fig. 5-12* shows the three slot geometries considered in this study. The relative permittivity of the material is kept constant.
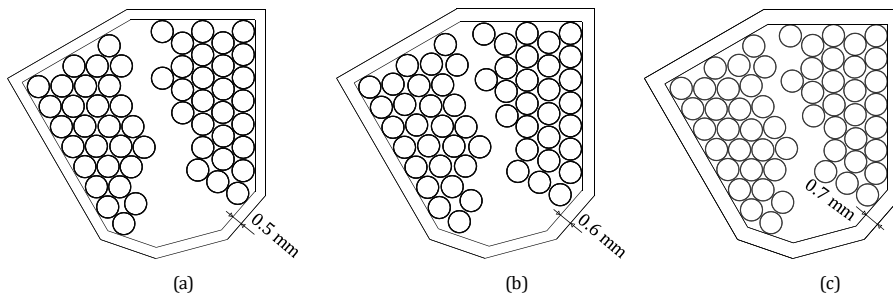
Fig. 5-12 - Three different slot geometries with different slot wall insulation thickness, (a) 0.5 mm, (b) nominal 0.6 mm, (c) 0.7 mm

TABLE 5-III shows the effect of the insulation thickness variation in the turn-to-ground parasitic capacitances. The three analyzed capacitances are selected to show the effect on a conductor facing the slot wall, a conductor surrounded by other conductors and a conductor close to the center of the slot. It can be observed that for increased insulation thickness te capacitance value is reduced for the three studied capacitances.

TABLE 5-III – Insulation thickness influence on turn-to-ground parasitic capacitances

Insulation thickness [mm]	$C_{1,1}$ [pF]	$C_{20,20}$ [pF]	$C_{28,28}$ [pF]
0.5 mm	4.39	0.0028	0.001
0.6 mm	4.18	2.29e-4	7.69e-4
0.7 mm	2.63	6.94e-5	1.37e-5

Fig. 5-13 shows the variation of both CM and DM impedance curves depending on the insulation thickness. The DM curve is barely affected by the change of turn-to-ground capacitances. However, some variations can be observed in the 1MHz – 10 MHz frequency band where the anti-resonace point is located. For the CM curve, amplitude changes correspond to the turn-to-ground capacitance variation. For reduced insulation thickness, the capacitance values increase and thus, the ampltitude of the CM curve is reduced. In addition, the insulation thickness slightly shifts the resonant points towards lower frequencies.
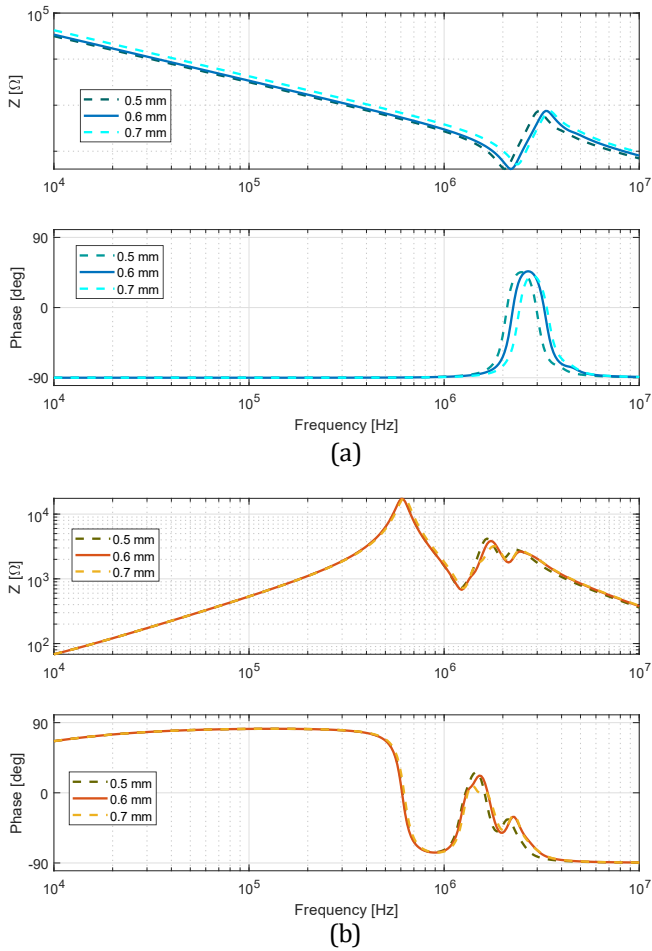
Fig. 5-13 - Impact of the variation of the slot wall insulation thickness in the high-frequency impedance curves, (a) CM, (b) DM

5.3.4. Turns per coil

The number of turns per coil dramatically affects the number of elements and nodes of the equivalent circuit. *Fig. 5-14* shows several slot geometries for different number of turns in a single coil.

(a) (b)

(c) (d)
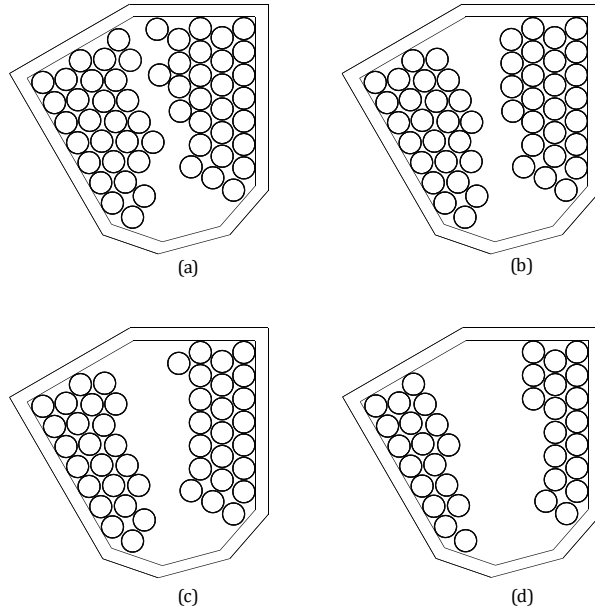
Fig. 5-14 - Four different slot geometries with different turns per coil, (a) nominal 28 turns, (b) 25 turns (c) 20 turns, (d) 15 turns

Fig. 5-15 shows the effect of the number of turns per coil on the CM and DM impedance curves. In the CM curve, a shifting towards higher frequencies of the resonant points can be observed. Moreover, the amplitude all over the considered frequency band increases for lower number of turns. A similar effect is observerved in the DM curve, where the resonant points are also shifted towards higher frequency points. The amplitude of these curves dramatically decreases over the inductive frequency bands and increases when the impedance has capacitive behavior.

135
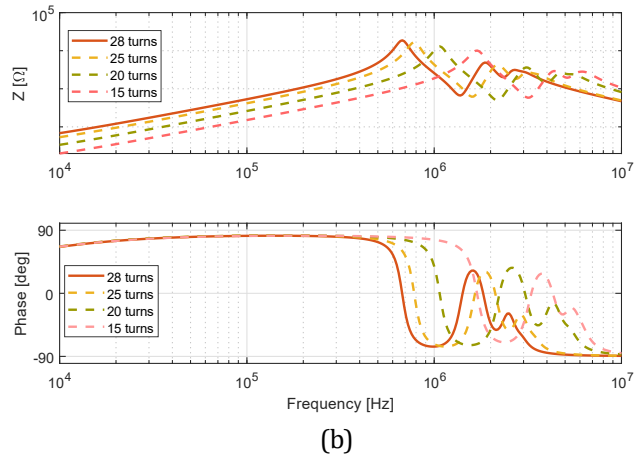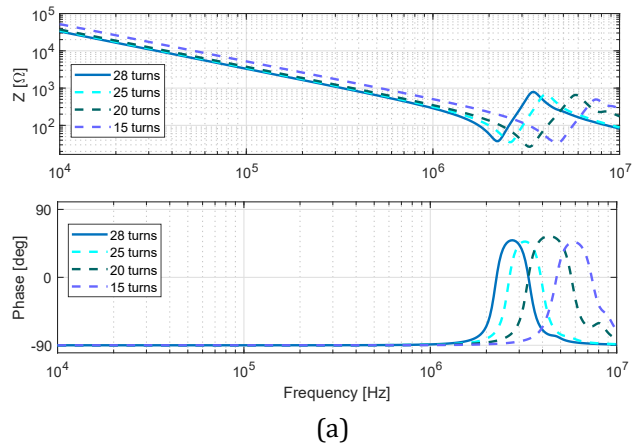
Fig. 5-15 - Impact of the variation of the slot wall insulation thickness in the high-frequency impedance curves, (a) CM, (b) DM

5.4.   Effect of material properties

This section analyses the effect of material chatacteristics on the RLC parameters and on the impedance curves. The materials forming the studied PMSM are the iron laminations, dielectric materials of the insulation elements and the copper forming the winding conductors. The input parameters related to material characteristics are found tabulated in literature tables or provided by the motor manufacturer.

Thus, the material characteristics of the machine constitute a notorious uncertainty while modelling the high-frequency impedance characteristics.

5.4.1. Iron core material

High-frequency small-signal frequency sweep injects low amplitude signals in the stator winding of the machine. The measurement is performed off-line with the motor in standstill conditions. As described in previous sections, the DC field created by the magnets in the rotor affects the iron instantaneous working point even in standstill conditions [119]. The BH characteristic of the iron material data sheet is utilized to estimate the low-frequency permeability value that affects the frequency-dependent complex permeability. Hence, the utilized low-frequency BH characteristic affects directly the RL parameters.

Three different BH characteristics are utilized to perform this analysis. The selected curves belong to the same family and manufacturer of electrical steel with the same lamination thickness. The BH curves of the three selected electrical steel types are shown in *Fig. 5-16.* TABLE 5-V presents the tabulated BH data from 0.7 T to 1.1 T for the three different materials.
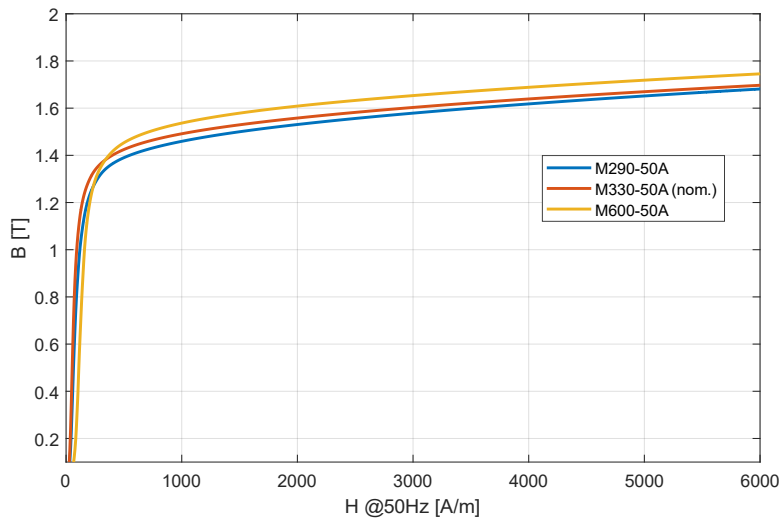
Fig. 5-16 - BH characteristics from three different electrical steel types at 50 Hz

TABLE 5-IV – Low-frequency electrical steel characteristics for three different electrical steel samples

B [T]	H@50Hz [A/m]	μ_r
M330-50A		
0.7	64.1	12415
0.8	71	11208
0.9	79.7	9985
1	91.8	8669
1.1	110	7234
M290-50A		
0.7	79.9	9960
0.8	89.9	8852
0.9	103	7726
1	119	6687
1.1	144	5526
M600-50A		
0.7	127	6266
0.8	136	5851
0.9	147	5413
1	159	5005
1.1	177	4496

The BH curve is the iron material input when evaluating the B-field in a magnetostatic analysis for a fixed rotor position. For a magnet remanence of 1.345 T, the obtained average B-field value in the stator mesh nodes does not critically change. However, the estimated low-frequency permeability described in equation (3-34) varies since different values of the magnetic field strength at 50 Hz (i.e., $H|_{B_{avg}}$) are obtained for the same values of the average B-field. *TABLE 5-V* shows tabulated values for the averaged asbsolute value of the B-field in the stator nodes and the low-frequency relative permeability for the three different electrical steel samples.

TABLE 5-V - Stator average B-field and low-frequency relative permeability values for three different electrical steel samples

Material	Average |B| [T]	$\mu_{r,DC}$
M330-50A	0.9754	8408
M290-50A	0.9810	6885
M600-50A	0.9838	5071

Fig. 5-17 shows the effect of the low-frequency relative permeability on the complex frequency dependent effective permeability obtained by using equation (3-25). Both real and imaginary parts differ in the low-frequency band (i.e., 10Hz-10kHz) and converge towards the same value for increased frequency values. The effect of the electrical steel type on a single conductor impedance is shown in *Fig. 5-18*. For slightly higher real and imaginary effective permeability the reactance increases and the resistance decreases. The variation for both real and imaginary part of the impedance is very light, with an average variation of 3.5% and 1.7% for the real and imaginary parts of the impedance respectively.
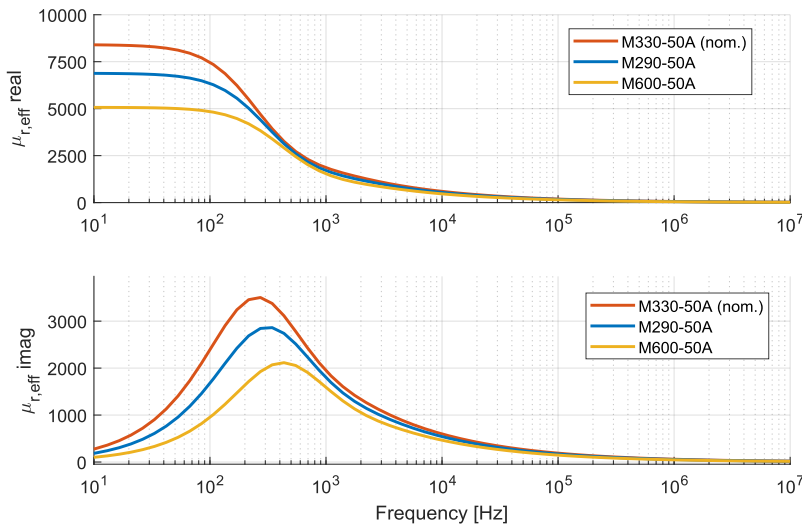
Fig. 5-17 - Effect of different material on the complex frequency dependent effective permeability
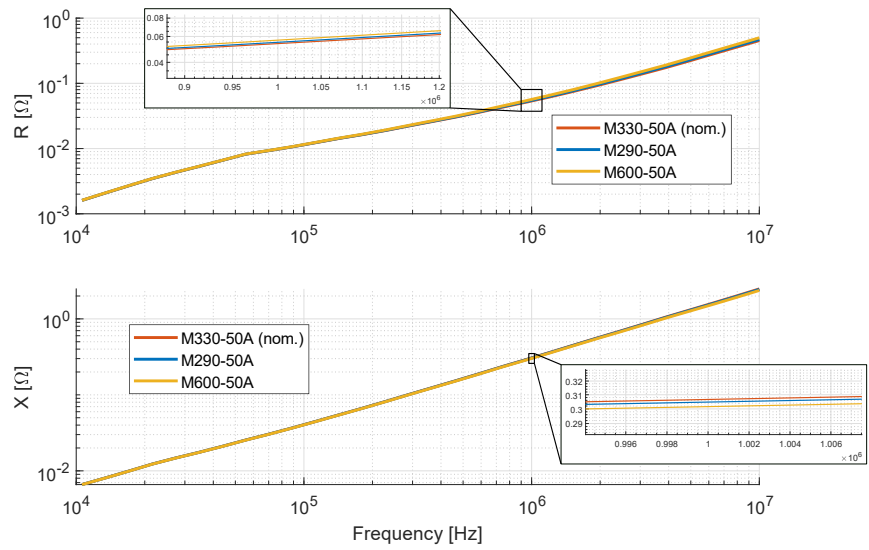
Fig. 5-18 – Self-resistance and reactance variation for different types of electrical steel
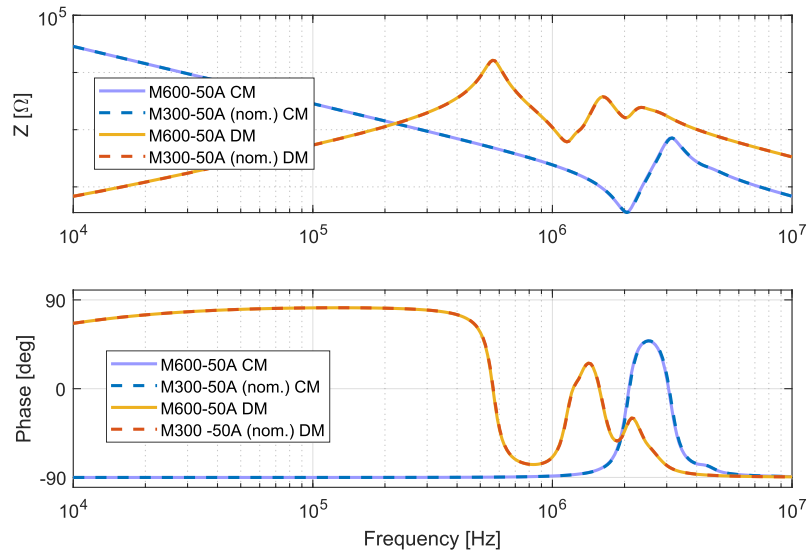
Fig. 5-19 - CM and DM impedance variation for different types of electrical steel

140

The effect of the RL parameter variation on the impedance curves is shown in *Fig. 5-19*. Only one type of electrical steel is considered since the variation of the low-frequency relative permeability has a very small impact on the CM and DM impedance response. The impedance shows negligible variation for the different types of electrical steel.

5.4.2. Magnet remanence

The magnet remanence defines the amplitude of the DC field created by the rotor magnets. Three different magnet remanence values are considered to perform the sensitivity analysis, where 1.345 T is considered the nominal value. The B-field distribution over the stator nodes depends on the magnet characteristics, achieving higher values for increased remanence. *Fig. 5-20* shows the stator B-field distribution for three different values of magnet remanence at a fixed rotor position. TABLE 5-VI shows the averaged absolute value for the B-field over the stator mesh nodes and the equivalent low-frequency relative permeability associated to these B-field values.

TABLE 5-VI - Stator average B-field and low-frequency relative permeability values for three different electrical steel samples

B_r magnet [T]	Average |B| [T]	$\mu_{r,DC}$
1.345	0.9754	8408
1.1	0.8403	10715
1	0.7798	11452

The variation of the RL parameters is similar to the variation shown for different types of electrical steel since the main parameter defining the effect of the magnet remanence is the low-frequency relative permeability. *Fig. 5-21* shows the effect of the magnet remanence variation on a single conductor resistance and reactance. The average variation is approximately 0.6% and 2% for the reactance and the resistance respectively. The variation of the CM and DM high-frequency impedance curves is again negligible and similar to the one observed in *Fig. 5-19*.

141
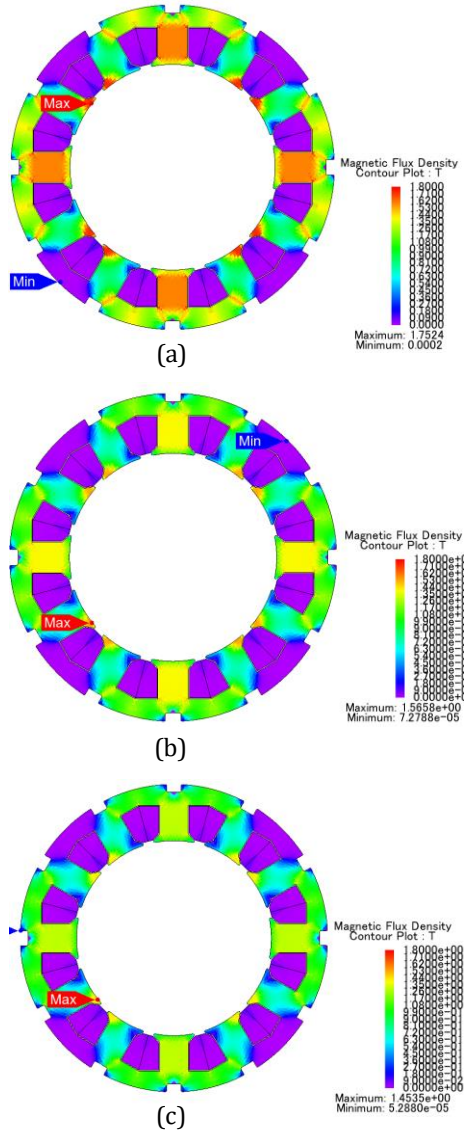
Fig. 5-20 - B-field distribution in the stator iron for different values of the rotor magnets remanence at a fixed rotor position, (a) 1.345 T, (b) 1.1 T, (c) 1T
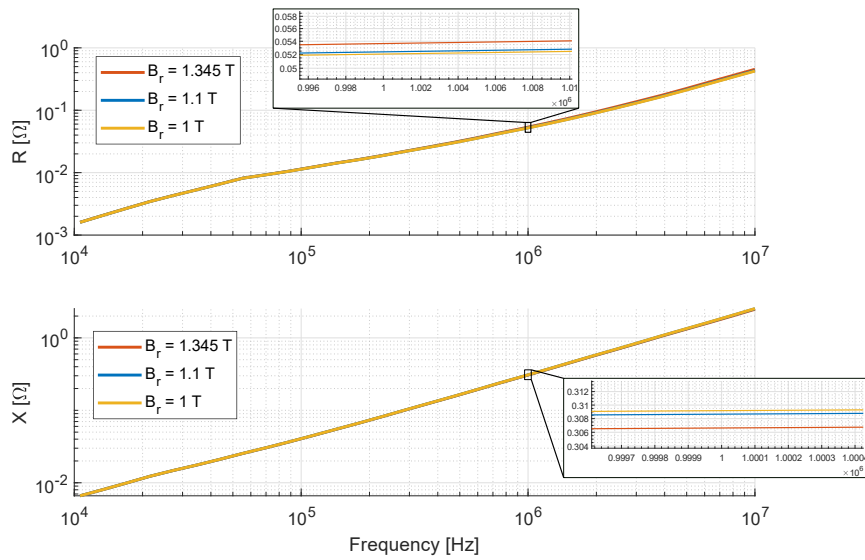
Fig. 5-21 - Self-resistance and reactance variation for different rotor magnet remanence values

5.4.3. Copper conductivity

The copper conductivity value represents an input for the magnetodynamic solver estimating the value of the RL parameters. It has a direct impact on the skin depth defining the current density in the conductors. In addition, the resistance of every conductor directly depends on this value. The nominal value provided by the motor manufacturer is 59.6 MS/m. Two extra values are adopted to perform the sensitivity analysis with a difference of ± 10 MS/m. *Fig. 5-22* shows the variation of the self-resistance and reactance of a single conductor for different values of the copper conductivity. It the zoomed in area it is possible to observe how both resistance and reactance are inversely proportional to the conductivity value. Note that the estimation of the single conductor impedances in this study has been performed with the same mesh dimensions and small innacuracies can appear over the higher frequency regions. The effect of copper conductivity value in the CM and DM curves is shown in Fig. *5-23*. The DM curve is mainly affected, with a slight variation over the inductive area and a small shifting of the resonant points. The only effect observed in the CM curve

143

is a light shift of the main resonant point and a light amplitude difference over the resonance band.
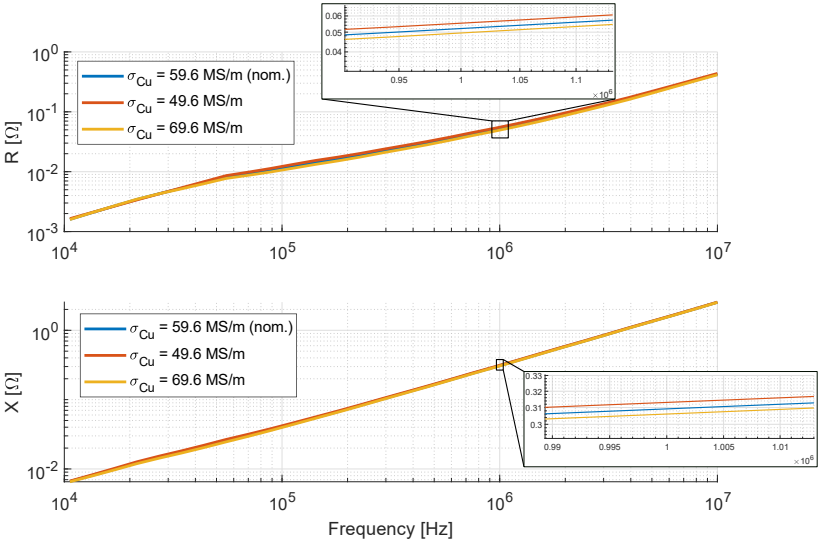
Fig. 5-22 - Self-resistance and reactance variation for different copper conductivity values
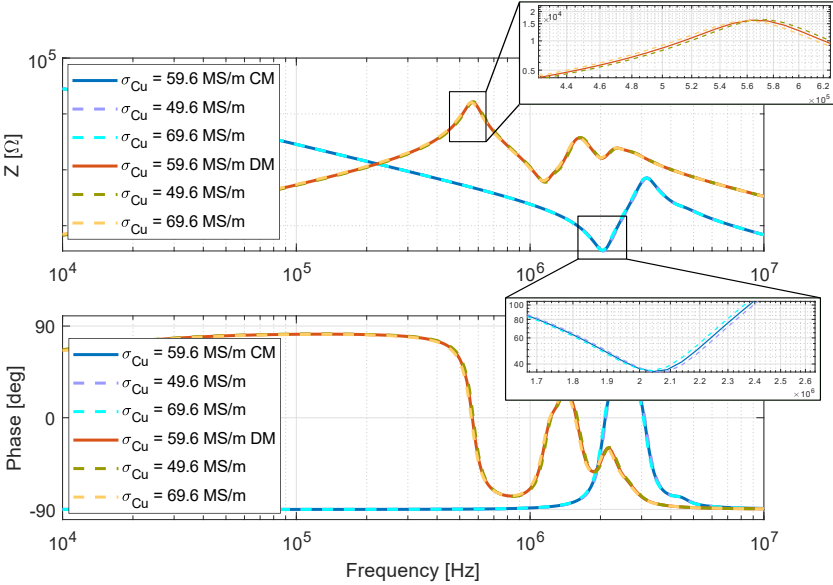
Fig. 5-23 - CM and DM impedance variation for different values of copper conductivity

5.4.4. Insulation material

The insulation material is present in the slot wall insulation and in the coating of the copper conductors for the e-ACC machine. The parameter defining the insulation material characteristics is the relative permittivity (ε_r), which is set at 3.5 by recommendation of the motor manufacturer. The values of the relative permittivity for polymeric materials typically range from 2 to 5. To perform the sensitivity analysis, three values are adopted including the nominal value and the two abovementioned limits. In addition, the variation of the material characteristics of the slot wall insulation thickness and the conductor coating are analyzed separately.

Fig. 5-24 shows six different capacitance matrices where the relative permittivity of the slot wall insulation and conductors coating is changed separately. The scales of the colormaps are adjusted to better highlight the variation of the turn-to-ground capacitances and inter-turn capacitances for each type of insulation. The slot wall insulation material mainly affects the diagonal terms, while the conductor insulation mainly influences inter-turn capacitances. The variation of the turn-to-ground capacitances is better observed for the conductors facing the slot wall (e.g., conductors 1 to 8), while the inter-turn capacitance variation is accentuated for neightbouring conductors (e.g., coupling between conductor 19 and 23). TABLE 5-VII presents numerical values for different matrix entries depending on the type of insulation and their relative permittivity value.

TABLE 5-VII - Capacitance matrix entries for different relative permittivity values

Capacitances [pF]	Slot wall insulation			Conductor insulation		
	ε_r=2	ε_r=3.5	ε_r=5	ε_r=2	ε_r=3.5	ε_r=5
C_{5-5}	1.01	1.56	2.02	1.52	1.56	1.58
$C_{1'-1'}$	2.33	3.57	4.59	3.45	3.57	3.62
$C_{15'-15'}$	1.34	2.02	2.55	1.96	2.02	2.04
C_{19-23}	5.21	5.21	5.21	3.89	5.21	6.17
$C_{1'-2'}$	3.12	3.13	3.14	2.70	3.13	3.36
$C_{10'-20'}$	1.21	1.21	1.21	1.12	1.21	1.25
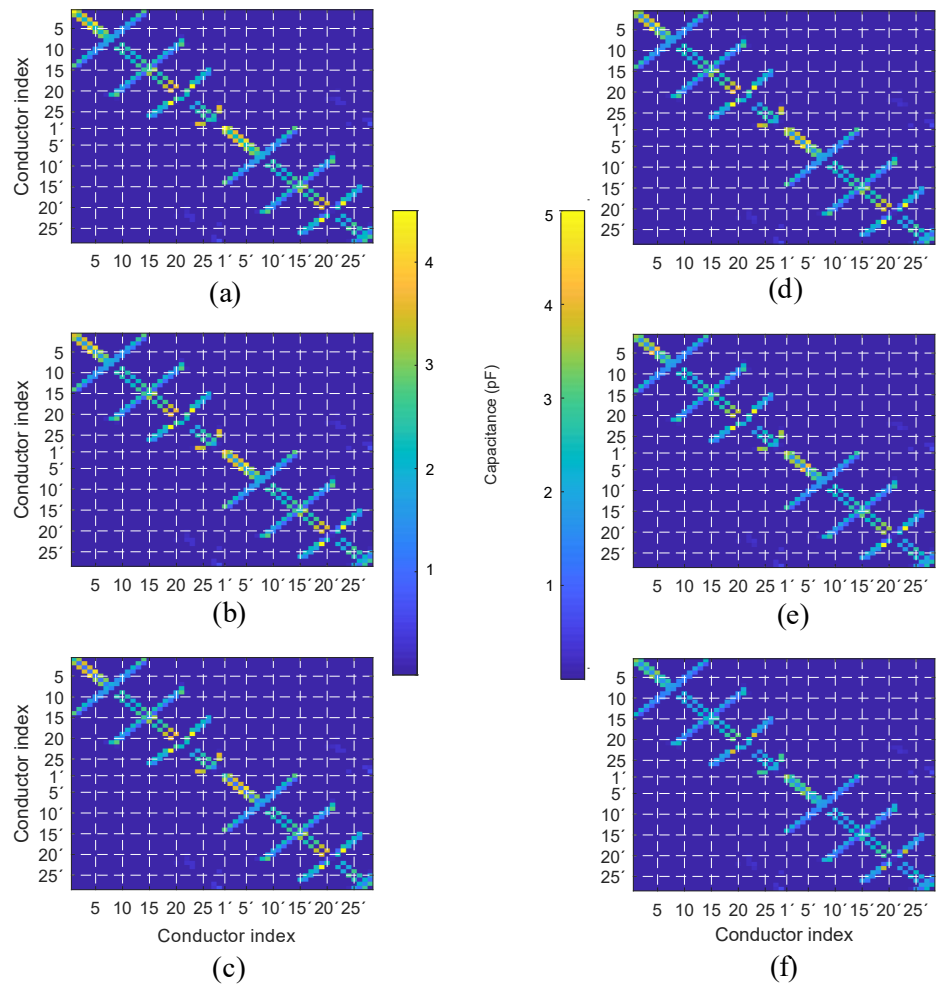
Fig. 5-24 - Capacitance matrices for different values of relative permittivity, slot wall insulation permittivity variation (conductor insulation at ε_r=3.5), (a) ε_r=5, (b) ε_r=3.5, (c) ε_r=2, conductor insulation permittivity variation (slot wall insulation at ε_r=3.5), (d) ε_r=5, (e) ε_r=3.5, (f) ε_r=2

The impact of the relative permittivity variation on the high-frequency impedance curves is shown in *Fig. 5-26* and *Fig. 5-25.* The slot wall insulation permittivity directly affects the amplitude of the curves when they have capacitive behavior. The resonant peaks are shifted

146

towards higher frequencies for reduced relative permittivity values. The damping of both curves is slightly affected. On the other hand, conductor insulation has little influence on the impedance curves both on amplitude and frequency location of the resonant points.
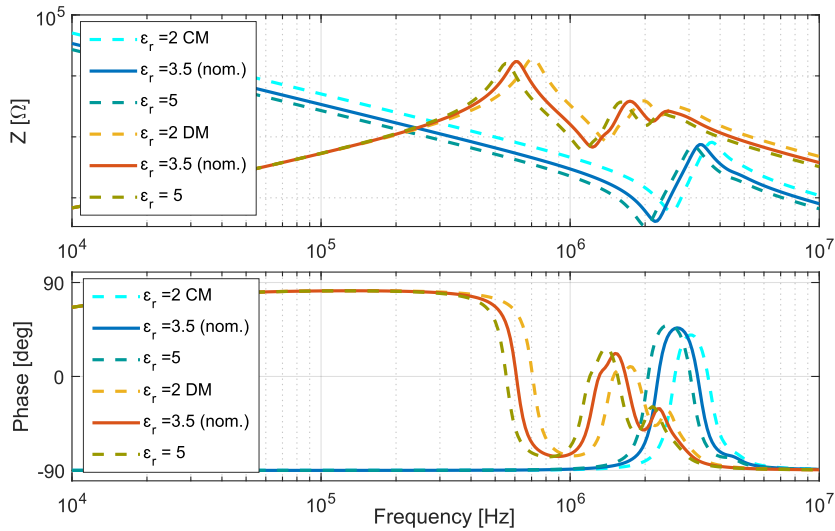
Fig. 5-25 - CM and DM impedance variation for different slot wall insulation relative permittivity values
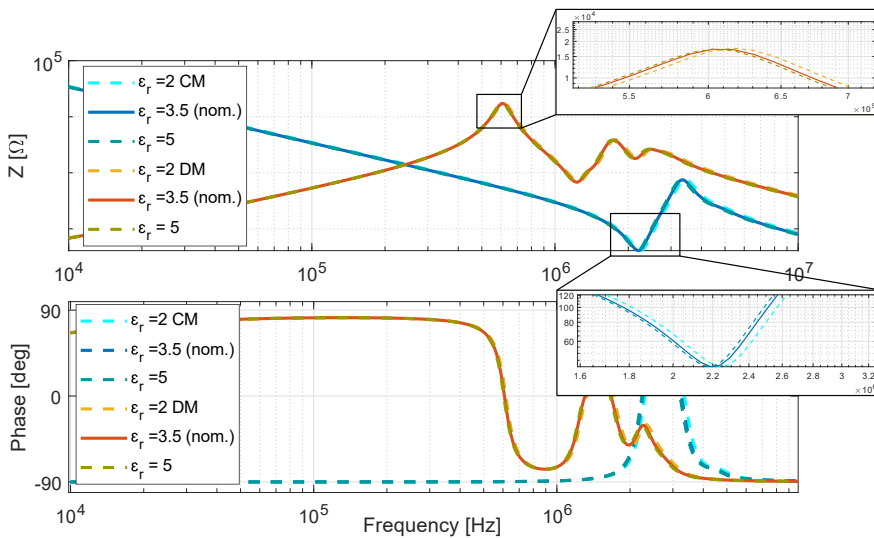
Fig. 5-26 CM and DM impedance variation for different conductor insulation relative permittivity values

6. Closure

The present dissertation aims to fully describe and understand the high-frequency modelling process of rotating electrical machines. In addition, a new deterministic numerical modelling approach conceived to evaluate the impact of early-stage design decisions on the high-frequency impedance response of a PMSM, is proposed and experimentally validated. A sensitivity analysis of input parameters of the model is performed to demonstrate the main applicability of the model, to analyze the most critical model inputs, and to quantify certain model uncertainties. The thesis contribution can be summarized in four major points:

- On the modelling of high-frequency phenomena for rotating electrical machines

- An original high-frequency impedance modelling strategy oriented towards early prediction for PMSMs

- On the effect of housing and rotor in the high-frequency PMSM response

- Identification of critical design parameters and quatification of model uncertainties

6.1. On the modelling of high-frequency phenomena for rotating electrical machines

Chapter 2 provides a thorough literature review of the available high-frequency phenomena modelling methods. According to the parametrization of the model two different modelling trends were identified: test-based and numerical. From an electrical machine manufacturer perspective, the parametrization of the model defines the earliness of the model applicability. Thus, the numerical parameter estimation represents the only available option when machine prototypes are not yet available. A trade-off between accuracy, computational cost and complexity of the input data frames the high-frequency modelling for early-stage prediction.

6.2. An original high-frequency impedance modelling strategy oriented towards early prediction

Chapter 3 presents a novel modelling method for high-frequency impedance prediction. The experimental validation for two different PMSMs is provided in Chapter 4.

The presented modelling method is implemented and validated on two different PMSMs with concentrated winding and double layer slots. The usage of experimental tuning and computationally expensive 3D simulations is avoided to satisfy the design framework. The input data is kept as simple as possible, which consists of 2D machine cross-sections, material characteristics provided by the motor manufacturer, stator winding connections, and the conductor distribution within the slot. Single slot conductors are modelled to consider inter-turn couplings. In addition, several complex high-frequency physical phenomena are considered in the method:

- *Skin and proximitty effects* are considered by adjusting the mesh thickness for each single conductor and for each simulation frequency
- *Eddy currents flowing within single laminations* at high frequencies are accounted by utilizing a homogenized iron core model. This is achieved by estimating a complex frequency-dependent relative permeability, which is modified for each simulation frequecy. Aditionally, the utilization of such homogenization technique allows the usage of a coarse mesh in the iron core, significantly reducing the computational cost.
- *Iron core material characteristics* at high frequencies are included in the homogenized iron core model. The only parameter extracted from the material data sheet is the low frequency relative pemeability ($\mu_{r,DC}$), which is obtained from the BH curve at 50 Hz provided by the manufacturer.
- *Frequency dependency of inductances and resistances* is implemented in the circuit by utilizing Laplace expressions embedded into active circuit elements in the SPICE simulator.

The usage of such expressions is limited to the frequency domain.

The dielectric losses in insulation elements cannot be estimated by utilizing a FEM solver. These have been considered in previous works by using experimental tuning, where the conductance of the turns is measured by using an impedance analyzer [83]. End-winding sections are not modelled to avoid three undesired scenarios. The first one is related to computationally expensive 3D simulations, since this is the common approach to model the end-winding electric and magnetic fields distribution [83], [93], [99]. The second obstacle is linked to the equivalent circuit computational efficiency, since end-winding sections add extra nodes to the linear system of equations to be solved in the SPICE solver. In third place, the end-winding geometry is seldom known with precision in early design stages. The method does not consider randomly wound machines, where the position of the conductors within the slot is not certainly known. However, the available slot area for conductor location is defined by geometric inputs such as fill factor, distance from simetry axis to last conductor, etc. The randomness of the conductor location is not assessed in the developed method.

The method is not intended to only achieve fast computational times but to satisfy the trade-off between accuracy, data simplicity and the simulation computational effort. The simulations are run from a Matlab general script, which calls, launches and retrieves results from the FEM and SPICE software. The device used for simulation is a Dell Precision 7520 with Intel(R) Core (TM) i7-7920HQ CPU (3.10GHz) and 31.19 Gb of usable RAM memory. A total of 12 frequency points between 10kHz and 10 MHZ are simulated for the magnetodynamic FEM analysis, while for the SPICE circuit 100 frequency points per decade are considered. The simulation times when simulating the e-ACC machine are shown in TABLE 6-I. The magnetodynamic FEM analysis represents a bottleneck for computation speed optimization.

TABLE 6-I - e-ACC machine simulation times

Simulation part	Time
Electrostatic FEM	5 min 60 sec
Magnetodynamic FEM	4 h 38 min 40 sec
SPICE solver	3 min 55 sec

151

Regarding accuracy, the method shows large discrepancies in the amplitude for both machines and both modes. A clear lack of damping in the resonant points is observed, where the amplitude of the simulation clearly overcomes the measured one. However, resonant points, and phase and amplitude trends are properly maped. In addition, the two analyzed machines can be differentiated by analyzing their simulation results, where resonant peaks and amplitudes concomitant with each machine can be identified. The possible reasons for modelling inaccuracies are stated below:

- The lack of damping is motivated by the neglected resistive loses such as dielectric loses and small eddy current losses in the laminations. In addition, small errors on the joule losses in the conductors, which are properly taken into account, may be present.

- The neglected end-winding sections add extra overall resistance, reactance and capacitance. Even for a concentrated winding, (i.e., with short end-winding lenght) the effect of such parameters can affect the accuracy of the prediction.

- Inaccuracies in the material characteristics also affect the prediction. The material data is obtained from data sheet values.

- Inaccuracies derived from the motor manufacturing process and advanced development. Some examples can be a conductor missplacement, slot wall insulation irregularities, tolerances, stator welding, etc.

6.3. On the effect of housing and rotor in the high-frequency PMSM response

Chapter 4 fully describes the experimental measurement campaign. Within this chapter, the effect of rotor and housing insertion is experimentally assessed to increase the validation certainty. In addition, the effect of the rotor position is studied experimentally to analyze the influence of the DC magnetic field originated in the rotor magnets. In Chapter 5 the effect of the variation of the different RLC

parameters and the numerical study of the rotor DC field effect are provided.

The housing insertion causes the amplitude to decrease in the CM impedance curve. In addition, the resonances of both CM and DM curves are slightly shifted towards lower frequency locations. These two variations indicate that the capacitance towards ground increases with the housing insertion according to the sensitivity analysis from *Fig. 5-1*. The DM impedance curve shows a light difference in amplitude all over its inductive part for the sample with housing and without rotor. The origin of this effect is uncertain since the inductive DM amplitude coincides for the stator sample and the full machine with housing and rotor.

The effect of the rotor insertion cannot be fully evaluated from *Fig. 4-20* since the rotor position is, a priori, not known. The experimental study of the rotor position is presented in detail in *Fig. 4-22*, *Fig. 4-24*, *Fig. 4-23*. The rotor position mainly affects the inductive amplitude of the DM curves for the different phase combinations. This increase indicates that the reactance of the coils is affected by the saturation in the iron (see *Fig. 5-4*). From the study presented in section 4.6, it is demonstrated that the highest DM amplitudes are obtained for rotor positions where the averaged B-field in the coils of the connected phases is low valued (see

TABLE 4-II, and TABLE 4-III). The DM amplitude variation concords with the numerical study presented in section 5.4.2, where the magnet remanence effect on the impedance response is evaluated. The analysis points out that for reduced averaged B-field in the coils, the reactance of single conductors slightly increases. Therefore, the DM amplitude over their inductive band increases as well. However, the variation of the low-frequency relative permeability depending on the averaged B-field, does not have a significant effect in the numerically predicted impedance response as shown in *Fig. 5-19*.

The contribution of the housing and rotor to the high-frequency impedance response of a PMSM can be summarized as follows:

153

- The housing inserts additional turn-to-ground capacitance, slightly lowering the amplitude in the CM response and slightly shifting the resonant points towards lower frequencies.
- The rotor contribution can be deduced from the DM amplitude over its inductive band (i.e., in this case from 10 kHz to approximately 600 kHz). The rotor position defines the B-field in the iron of the stator coils, which influences the instantaneous working point in the hysteresis charcteristic. Thus, for reduced average B-field in the connected phases, the amplitude of the DM impedance slightly increases. This is supported by the numerical computation of the low-frequency relative permability. However, the utilized numerical model does not properly map this effect since low-frequency relative permeability variation does not significantly affect the impedance curves, while the amplitude difference is obvious for the experimental test.

- The stator winding represents the main contribution to the high-frequency impedance response for both propagation modes. The insertion of the housing and the rotor does not represent a critical variation of the impedance trends and resonant point location for the machine under study.

6.4. Identification of critical design parameters and quatification of model uncertainties

Chapter 5 presents a detailed sensitivity analysis separately studying the effect of the RLC parameters, geometric parameters, stator winding connection, and material properties in the high-frequency impedance response.

The effect of the RLC parameter variation is used as a reference to evaluate possible model inaccuracies and improvements. The connection of the different coils (i.e., series or parallel connection) heavily affects the impedance. It has been demonstrated that the series connection of coils varies both the amplitude of the impedances and the location of resonant points. For parallel connected coils, the resonances are kept at a fixed frequency, while the amplitude is heavily affected.

The shape of the slot will directly affect all the parameters of the equivalent circuit. This feature is not studied because it represents the base input for the model. The impact of the stack length, conductor diameter, slot wall insulation thickness and turns-per-coil is studied. The stack length and the number of turns-per-coil represent the most critical parameter affecting the high-frequency impedance response. A lower impact is observed for the variation of the conductor diameter, while slot wall insulation thickness slightly affects the CM impedance curve, showing a neglegible influence on the DM response.

The most critical material characteristic affecting both impedance curves is the slot wall insulation permittivity, which clearly affects capacitive amplitudes and the location of the resonant points. The copper conductor conductivity does not affect significatively the impedance for values around variations of tenths of MS/m. The magnet remanence and the type of electrical steel affect the estimated low-frequency relative permeability value. The variation affects the effective permeability over the lower frequency band. However, the alteration of such parameter does not significatively affect the impedance curves.

The presented sensitivity analysis identifies several critical design parameters affecting the high-frequency impedance response. These are numbered as follows:

- Stator winding connection
- Stack length
- Number of turns-per-coil
- Conductor diameter
- Slot wall insulation permittivity

6.5. Future work

The numerical estimation of the high-frequency impedance response in rotating electrical machines presents a large number of challenges to be addressed in future research works.

The presented method should be tested in machines without DC field in the rotor such as induction and pure synchronous reluctance machines. The validation for stators with distributed winding should be

155

also performed since they present larger end-winding sections, which may reduce the accuracy of the method. The sensitivity analysis of the design parameters can be addressed from an experimental perspective by building custom machine stator samples with different stack length, turns-per-coil, conductor diameter, etc.

The accuracy of the method can be enhanced trough the development of a reduced end-winding model accurately mapping parasitic capacitances and frequency-dependent RL parameters. The FEM estimation of RLC parameters in coils surrounded by laminated iron cores can be further validated by studying simple coils. The estimation of dielectric losses in the insulation elements without utilizing experimental tuning would also represent an accuracy improvement since the damping in the resonant points would significatively increase. The computation speed could be optimized by further simplifying the estimation of RL parameters in the magnetodynamic FEM solver.

The method shows potential applicability for stator fault prediction since the winding connection affects the impedance response of the machine in both modes. The modelling approach could help on predicting the impedance changes when a short circuit within the winding occurs. Finally, the measurement of the machine impedance on-line instead of in standstill conditions could represent an advantage for the numerical prediction of EMI and for the method applicability in the condition monitoring and fault diagnosis field.

REFERENCES

[1]   "COMMUNICATION FROM THE COMMISSION TO THE EUROPEAN PARLIAMENT, THE EUROPEAN COUNCIL, THE COUNCIL, THE EUROPEAN ECONOMIC AND SOCIAL COMMITTEE AND THE COMMITTEE OF THE REGIONS: THE EUROPEAN GREEN DEAL," 2019.

[2]   H. Du, Z. Chen, B. Peng, F. Southworth, S. Ma and Y. Wang, "What drives CO2 emissions from the transport sector? A linkage analysis," *Energy,* vol. 175, p. 195–204, 2019.

[3]   T. Pardi, "Prospects and contradictions of the electrification of the European automotive industry: the role of European Union policy," *International Journal of Automotive Technology and Management,* 2021.

[4]   J. Barkenbus, "Our electric automotive future: CO2 savings through a disruptive technology," *Policy and Society,* vol. 27, p. 399–410, 2009.

[5]   M. Bellis, "The History of Electric Vehicles Began in 1830," 2021. [Online]. Available: thoughtco.com/history-of-electric-vehicles-1991603. [Accessed October 2021].

[6]   B. Lequesne, "Automotive electrification: The nonhybrid story," *IEEE Transactions on Transportation Electrification,* vol. 1, p. 40–53, 2015.

[7]   M. Ehsani, K. V. Singh, H. O. Bansal and R. T. Mehrjardi, "State of the Art and Trends in Electric and Hybrid Electric Vehicles," IEEE, 2021.

[8]   R. Irle, "EVvolumes.com," September 2021. [Online]. Available: https://www.ev-volumes.com/. [Accessed 2021].

[9]   M. Ehsani, Y. Gao, S. Longo and K. M. Ebrahimi, Modern electric, hybrid electric, and fuel cell vehicles, CRC press, 2018.

[10]   N. Mohan, T. M. Undeland and W. P. Robbins, Power electronics: converters, applications, and design, John wiley & sons, 2003.

[11]   T. Jokinen, V. Hrabovcova and J. Pyrhonen, Design of rotating electrical machines, John Wiley & Sons, 2013.

[12]   T. Herold, S. Böhmer, D. Franck and K. Hameyer, "Data analysis in the production process of electrical drive systems," in *6. Conference on Future Automotive Technology*, 2017.

[13] B. Heller and A. Veverka, Surge phenomena in electrical machines, Iliffe, 1968.

[14] R. J. Kerkman, "Twenty years of PWM AC drives: When secondary issues become primary concerns," in *Proceedings of the 1996 IEEE IECON. 22nd International Conference on Industrial Electronics, Control, and Instrumentation*, 1996.

[15] C. R. Paul, Introduction to electromagnetic compatibility, vol. 184, John Wiley & Sons, 2006.

[16] A. Nagel and R. W. De Doncker, "Analytical approximations of interference spectra generated by power converters," in *IAS'97. Conference Record of the 1997 IEEE Industry Applications Conference Thirty-Second IAS Annual Meeting*, 1997.

[17] E. Persson, "Transient effects in application of PWM inverters to induction motors," *IEEE Transactions on Industry Applications,* vol. 28, p. 1095–1101, 1992.

[18] P. Xie, G. Vakil and C. Gerada, "Electric drive systems with long feeder cables," *IET Electric Power Applications,* vol. 14, p. 16–30, 2020.

[19] R. J. Kerkman, D. Leggate, D. Schlegel and G. Skibinski, "PWM inverters and their influence on motor overvoltage," in *Proceedings of APEC 97-Applied Power Electronics Conference*, 1997.

[20] L. Wang, C. N. M. Ho, F. Canales and J. Jatskevich, "High-frequency cable and motor modeling of long-cable-fed induction motor drive systems," in *2010 IEEE Energy Conversion Congress and Exposition*, 2010.

[21] J. Boyd, "The causes and the control of electrical currents in bearings," *Lubrication Engineering,* vol. 15, p. 28, 1959.

[22] A. B. B. Drives, "Bearing currents in modern AC drive systems," *Technical Guide,* 2011.

[23] T. Hadden, J. W. Jiang, B. Bilgin, Y. Yang, A. Sathyan, H. Dadkhah and A. Emadi, "A review of shaft voltages and bearing currents in EV and HEV motors," in *IECON 2016-42nd Annual Conference of the IEEE Industrial Electronics Society*, 2016.

[24] H. Tischmacher and S. Gattermann, "Bearing currents in converter operation," in *The XIX International Conference on Electrical Machines-ICEM 2010*, 2010.

[25] A. Muetze, Bearing currents in inverter-fed AC-motors, Shaker-Verlag GmbH, 2004.

[26] P. Mäki-Ontto and others, "Modeling and reduction of shaft voltages in AC motors fed by frequency converters," 2006.

[27] G. L. Skibinski, R. J. Kerkman and D. Schlegel, "Introduction to electromagnetic compatibility," *IEEE Industry Applications Magazine,* vol. 5, p. 47–80, 1999.

[28] S. E. S. Committee and others, "Limits and methods of measurement of radio disturbance characteristics of components and modules for the protection of receivers used on board vehicles," *SAE Standard SAE J1113,* vol. 41, 1995.

[29] S. Chen, "Bearing current, EMI and soft switching in induction motor drives: a systematic analysis, design and evaluation," 1995.

[30] H.-K. Yun, Y.-C. Kim, C.-Y. Won, Y.-R. Kim, Y.-S. Kim and S.-W. Choi, "A study on inverter and motor winding for conducted EMI prediction," in *ISIE 2001. 2001 IEEE International Symposium on Industrial Electronics Proceedings (Cat. No. 01TH8570)*, 2001.

[31] M. Moreau, N. Idir and P. Le Moigne, "Modeling of conducted EMI in adjustable speed drives," *IEEE Transactions on Electromagnetic Compatibility,* vol. 51, p. 665–672, 2009.

[32] B. Revol, J. Roudet, J.-L. Schanen and P. Loizelet, "EMI study of three-phase inverter-fed motor drives," *IEEE Transactions on Industry Applications,* vol. 47, p. 223–231, 2010.

[33] G. Spadacini, F. Grassi and S. A. Pignari, "Modelling and Simulation of Conducted Emissions in the Powertrain of Electric Vehicles.," *Progress in Electromagnetics Research B,* vol. 69, 2016.

[34] C. Purcarea, "High-frequency parasitic effects in electric drives with long cables," 2011.

[35] J. M. Erdman, R. J. Kerkman, D. W. Schlegel and G. L. Skibinski, "Effect of PWM inverters on AC motor bearing currents and shaft voltages," *IEEE transactions on Industry Applications,* vol. 32, p. 250–259, 1996.

[36] M. T. Wright, S. J. Yang and K. McLeay, "General theory of fast-fronted interturn voltage distribution in electrical machine windings," in *IEE Proceedings B-Electric Power Applications*, 1983.

[37] J. L. Guardado and K. J. Cornick, "A computer model for calculating steep-fronted surge distribution in machine windings," *IEEE*

Transactions on Energy Conversion, vol. 4, p. 95–101, 1989.

[38] P. G. McLaren and M. H. Abdel-Rahman, "Modeling of large AC motor coils for steep-fronted surge studies," *IEEE Transactions on Industry applications,* vol. 24, p. 422–426, 1988.

[39] A. Consoli, G. Oriti, A. Testa and A. L. Julian, "Induction motor modeling for common mode and differential mode emission evaluation," in *IAS'96. Conference Record of the 1996 IEEE Industry Applications Conference Thirty-First IAS Annual Meeting*, 1996.

[40] G. Grandi, D. Casadei and A. Massarini, "High frequency lumped parameter model for AC motor windings," in *European Conference on Power Electronics and Applications*, 1997.

[41] A. Boglietti and E. Carpaneto, "Induction motor high frequency model," in *Conference Record of the 1999 IEEE Industry Applications Conference. Thirty-Forth IAS Annual Meeting (Cat. No. 99CH36370)*, 1999.

[42] D. Busse, J. Erdman, R. J. Kerkman, D. Schlegel and G. Skibinski, "Bearing currents and their relationship to PWM drives," *IEEE Transactions on Power Electronics,* vol. 12, p. 243–252, 1997.

[43] G. Skibinski, R. Kerkman, D. Leggate, J. Pankau and D. Schlegel, "Reflected wave modeling techniques for PWM AC motor drives," in *APEC'98 Thirteenth Annual Applied Power Electronics Conference and Exposition*, 1998.

[44] L. Ran, S. Gokani, J. Clare, K. J. Bradley and C. Christopoulos, "Conducted electromagnetic emissions in induction motor drive systems. I. Time domain analysis and identification of dominant modes," *IEEE Transactions on Power Electronics,* vol. 13, p. 757–767, 1998.

[45] L. Ran, S. Gokani, J. Clare, K. J. Bradley and C. Christopoulos, "Conducted electromagnetic emissions in induction motor drive systems. II. Frequency domain models," *IEEE Transactions on Power Electronics,* vol. 13, p. 768–776, 1998.

[46] G. Suresh, H. A. Toliyat, D. A. Rendusara and P. N. Enjeti, "Predicting the transient effects of PWM voltage waveform on the stator windings of random wound induction motors," *IEEE Transactions on Power Electronics,* vol. 14, p. 23–30, 1999.

[47] N. Idir, Y. Weens, M. Moreau and J.-J. Franchaud, "High-frequency behavior models of AC motors," *IEEE Transactions on Magnetics,*

vol. 45, p. 133–138, 2009.

[48] K. Jia, G. Bohlin, M. Enohnyaket and R. Thottappillil, "Modelling an AC motor with high accuracy in a wide frequency range," *IET Electric Power Applications,* vol. 7, p. 116–122, 2013.

[49] C. Bi, K. Jia, Y. Wu, L. Dong, H. Li, W. Yao, G. Liu and H. Zhang, "High-frequency electric-motor modelling for conducted CM current prediction in adjustable speed drive system," *IET Power Electronics,* vol. 11, p. 1257–1265, 2018.

[50] B. Gustavsen and A. Semlyen, "Rational approximation of frequency domain responses by vector fitting," *IEEE Transactions on power delivery,* vol. 14, p. 1052–1061, 1999.

[51] B. Gustavsen, "Improving the pole relocating properties of vector fitting," *IEEE Transactions on Power Delivery,* vol. 21, p. 1587–1592, 2006.

[52] D. Deschrijver, M. Mrozowski, T. Dhaene and D. De Zutter, "Macromodeling of multiport systems using a fast implementation of the vector fitting method," *IEEE Microwave and wireless components letters,* vol. 18, p. 383–385, 2008.

[53] I. Stevanović, B. Wunsch and S. Skibin, "Behavioral high-frequency modeling of electrical motors," in *2013 Twenty-Eighth Annual IEEE Applied Power Electronics Conference and Exposition (APEC)*, 2013.

[54] J. Sun and L. Xing, "Parameterization of three-phase electric machine models for EMI simulation," *IEEE Transactions on Power Electronics,* vol. 29, p. 36–41, 2013.

[55] M. Schinkel, S. Weber, S. Guttowski, W. John and H. Reichl, "Efficient HF modeling and model parameterization of induction machines for time and frequency domain simulations," in *Twenty-First Annual IEEE Applied Power Electronics Conference and Exposition, 2006. APEC'06.*, 2006.

[56] B. Mirafzal, G. L. Skibinski and R. M. Tallam, "Determination of parameters in the universal induction motor model," *IEEE Transactions on Industry Applications,* vol. 45, p. 142–151, 2009.

[57] B. Mirafzal, G. L. Skibinski, R. M. Tallam, D. W. Schlegel and R. A. Lukaszewski, "Universal induction motor model with low-to-high frequency-response characteristics," *IEEE Transactions on Industry Applications,* vol. 43, p. 1233–1246, 2007.

[58] M. A. Gries and B. Mirafzal, "Permanent magnet motor-drive frequency response characterization for transient phenomena and conducted EMI analysis," in *2008 Twenty-Third Annual IEEE Applied Power Electronics Conference and Exposition*, 2008.

[59] M. Degano, P. Zanchetta, L. Empringham, E. Lavopa and J. Clare, "HF induction motor modeling using automated experimental impedance measurement matching," *IEEE Transactions on Industrial Electronics,* vol. 59, p. 3789–3796, 2012.

[60] G. Vidmar and D. Miljavec, "A universal high-frequency three-phase electric-motor model suitable for the delta-and star-winding connections," *IEEE transactions on power electronics,* vol. 30, p. 4365–4376, 2014.

[61] M. S. Toulabi, L. Wang, L. Bieber, S. Filizadeh and J. Jatskevich, "A universal high-frequency induction machine model and characterization method for arbitrary stator winding connections," *IEEE Transactions on Energy Conversion,* vol. 34, p. 1164–1177, 2019.

[62] F. Zare, "High frequency model of an electric motor based on measurement results," *Australian Journal of Electrical and Electronics Engineering,* vol. 4, p. 17–24, 2008.

[63] S.-P. Weber, E. Hoene, S. Guttowski, W. John and H. Reichl, "Modeling induction machines for EMC-analysis," in *2004 IEEE 35th Annual Power Electronics Specialists Conference (IEEE Cat. No. 04CH37551)*, 2004.

[64] K. Gulez and A. A. Adam, "High-frequency common-mode modeling of permanent magnet synchronous motors," *IEEE transactions on electromagnetic compatibility,* vol. 50, p. 423–426, 2008.

[65] Y. Ryu, B.-R. Park and K. J. Han, "Estimation of high-frequency parameters of AC machine from transmission line model," *IEEE Transactions on Magnetics,* vol. 51, p. 1–4, 2015.

[66] X. Pan, R. Ehrhard and R. Vick, "An extended high frequency model of permanent magnet synchronous motors in hybrid vehicles," in *10th International Symposium on Electromagnetic Compatibility*, 2011.

[67] X. Wang, W. Liu, D. Zhao, K. Shen and N. Yang, "Conducted EMI modeling of a three-stage starter/generator system for more electric aircraft," in *IECON 2017-43rd Annual Conference of the*

IEEE Industrial Electronics Society, 2017.

[68] X. Ma, R. Liu, B. Zheng and Y. Zhang, "Analysis and calculation of capacitance parameters in induction machines to predict shaft voltage," in *2012 15th International Conference on Electrical Machines and Systems (ICEMS)*, 2012.

[69] V. Kindl, B. Skala, R. Pechanek, M. Byrtus and K. Hruska, "Calculation of induction machine parasitic capacitances using finite element method," in *2016 ELEKTRO*, 2016.

[70] C. Martis, H. Hedesiu and B. Tataranu, "High-frequency model and conductive interferences of a small doubly salient permanent magnet machine," in *2004 IEEE International Conference on Industrial Technology, 2004. IEEE ICIT'04.*, 2004.

[71] O. A. Mohammed, S. Ganu, S. Liu, Z. Liu and N. Abed, "Study of high frequency model of permanent magnet motor," in *IEEE International Conference on Electric Machines and Drives, 2005.*, 2005.

[72] V. Venegas, E. Melgoza, J. L. Guardado, R. Mota and R. Escarela, "A Time-Domain Rotating Machine Model for Switching Overvoltage Studies using Network Synthesis for the Winding Impedance," in *IEEE International Conference on Electric Machines and Drives, 2005.*, 2005.

[73] O. A. Mohammed, S. Ganu, N. Abed, S. Liu and Z. J. I. T. O. M. Liu, "High frequency PM synchronous motor model determined by FE analysis," *IEEE transactions on magnetics,* vol. 42, p. 1291–1294, 2006.

[74] O. Henze, Z. Cay, O. Magdun, H. De Gersem, T. Weiland and A. Binder, "A stator coil model for studying high-frequency effects in induction motors," in *2008 International Symposium on Power Electronics, Electrical Drives, Automation and Motion*, 2008.

[75] K. Maki, H. Funato and L. Shao, "Motor modeling for EMC simulation by 3-D electromagnetic field analysis," in *2009 IEEE International Electric Machines and Drives Conference*, 2009.

[76] H. De Gersem, O. Henze, T. Weiland and A. Binder, "Simulation of wave propagation effects in machine windings," *COMPEL-The international journal for computation and mathematics in electrical and electronic engineering,* 2010.

[77] O. A. Mohammed and S. Ganu, "FE-circuit coupled model of

electric machines for simulation and evaluation of EMI issues in motor drives," *IEEE Transactions on Magnetics,* vol. 46, p. 3389–3392, 2010.

[78] J. Benecke, "Impedance and emission optimization of low-voltage DC motors for EMC compliance," *IEEE Transactions on Industrial Electronics,* vol. 58, p. 3833–3839, 2010.

[79] V. Mihaila, S. Duchesne and D. Roger, "A simulation method to predict the turn-to-turn voltage spikes in a PWM fed motor winding," *IEEE Transactions on Dielectrics and Electrical Insulation,* vol. 18, p. 1609–1615, 2011.

[80] F. Abdallah, EMC analysis of electric drives, Department of Measurement Technology and Industrial Electrical Engineering …, 2012.

[81] I. Rasoanarivo, C. Tyrel, N. Takorabet and F.-M. Sargos, "High frequency modeling of the winding wires of AC machines," in *2013 15th European Conference on Power Electronics and Applications (EPE)*, 2013.

[82] B. Heidler, K. Brune and M. Doppelbauer, "High-frequency model and parameter identification of electrical machines using numerical simulations," in *2015 IEEE International Electric Machines & Drives Conference (IEMDC)*, 2015.

[83] N. Boucenna, F. Costa, S. Hlioui and B. Revol, "Strategy for predictive modeling of the common-mode impedance of the stator coils in AC machines," *IEEE Transactions on Industrial Electronics,* vol. 63, p. 7360–7371, 2016.

[84] C. Jaeger, I. Grinbaum and J. Smajic, "Numerical simulation and measurement of common-mode and circulating bearing currents," in *2016 XXII International Conference on Electrical Machines (ICEM)*, 2016.

[85] M. Toudji, G. Parent, S. Duchesne and P. Dular, "Determination of winding lumped parameter equivalent circuit by means of finite element method," *IEEE Transactions on Magnetics,* vol. 53, p. 1–4, 2017.

[86] N. Radja, S. N. Larbi and others, "Improved RLMC-Circuit HF-Dependent Parameters Using FE-EM Computation Dedicated to Predict Fast Transient Voltage Along Insulated Windings," *IEEE Transactions on Electromagnetic Compatibility,* vol. 61, p. 301–308, 2018.

164

[87] Y. Xie, J. Zhang, F. Leonardi, A. R. Munoz, M. W. Degner and F. Liang, "Modeling and verification of electrical stress in inverter-driven electric machine windings," *IEEE Transactions on Industry Applications,* vol. 55, p. 5818–5829, 2019.

[88] M. Jaritz, N. Stieger, C. Jaeger, M. Schneider, D. Vukovic, S. Blume and J. Smajic, "An improved model for the common mode impedance in inverter-fed ac machines," in *2020 International Conference on Electrical Machines (ICEM)*, 2020.

[89] O. Magdun and A. Binder, "Calculation of roller and ball bearing capacitances and prediction of EDM currents," in *2009 35th Annual Conference of IEEE Industrial Electronics*, 2009.

[90] A. Muetze and A. Binder, "Calculation of motor capacitances for prediction of the voltage across the bearings in machines of inverter-based drive systems," *IEEE Transactions on Industry Applications,* vol. 43, p. 665–672, 2007.

[91] M. Vukotić, D. Miljavec and D. Vončina, "Calculation and measurement of the capacitance between stator frame and slot conductors and its influence on common-mode current," in *2016 10th International Conference on Compatibility, Power Electronics and Power Engineering (CPE-POWERENG)*, 2016.

[92] C. S. Chaves, J. R. Camacho, H. De Paula, M. L. R. Chaves and E. Saraiva, "Capacitances calculation using FEM for transient overvoltage and common mode currents prediction in inverter-driven induction motors," in *2011 IEEE Trondheim PowerTech*, 2011.

[93] K. Vostrov, J. Pyrhönen and J. Ahola, "The role of end-winding in building up parasitic capacitances in induction motors," in *2019 IEEE International Electric Machines & Drives Conference (IEMDC)*, 2019.

[94] J. O. Stockbrügger and B. Ponick, "Analytical determination of the end-winding portion of the winding-to-rotor capacitance for the prediction of bearing voltage in electrical machines," *Electrical Engineering,* vol. 102, p. 2481–2491, 2020.

[95] N. Djukic, L. Encica and J. J. H. Paulides, "Electrical machines: Comparison of existing analytical models and FEM for calculation of turn-to-turn capacitance in formed windings," in *2016 Eleventh International Conference on Ecological Vehicles and Renewable Energies (EVER)*, 2016.

165

[96] L. F. de Freitas Gutierres and G. Cardoso, "Analytical technique for evaluating stray capacitances in multiconductor systems: single-layer air-core inductors," *IEEE Transactions on Power Electronics,* vol. 33, p. 6147–6158, 2017.

[97] V. Venegas, J. L. Guardado, E. Melgoza and M. Hernandez, "A finite element approach for the calculation of electrical machine parameters at high frequencies," in *2007 IEEE Power Engineering Society General Meeting*, 2007.

[98] T. Župan, B. Trkulja, R. Obrist, T. Franz, B. Cranganu-Cretu and J. Smajic, "Transformer windings' RLC parameters calculation and lightning impulse voltage distribution simulation," *IEEE Transactions on Magnetics,* vol. 52, p. 1–4, 2015.

[99] R. S. Ferreira and A. C. Ferreira, "Analysis of End-Windings Influence on the Transient Voltage Distribution in Machine Stator Windings by a Three Phase Model," *IEEE Transactions on Energy Conversion,* vol. 36, p. 2110–2119, 2020.

[100] A. Muetze, H. De Gersem and T. Weiland, "Influence of teeth and cooling ducts on the high-frequency common mode flux of inverter-fed ac machines," in *Fourtieth IAS Annual Meeting. Conference Record of the 2005 Industry Applications Conference, 2005.*, 2005.

[101] T. Kovanen, L. Söderlund and L. Kettunen, "Mechanism behind high-frequency circulating bearing currents in view of motor structures," *IET Science, Measurement & Technology,* vol. 2, p. 233–243, 2008.

[102] N. Boucenna, S. Hlioui, B. Revol and F. Costa, "A detailed analysis of the propagation paths of high-frequency common mode currents in AC motors," in *2013 15th European Conference on Power Electronics and Applications (EPE)*, 2013.

[103] O. Magdun and A. Binder, "An iron core impedance model for calculating high frequency common mode currents and shaft voltages in inverter-fed AC machines," in *International Symposium on Power Electronics Power Electronics, Electrical Drives, Automation and Motion*, 2012.

[104] H. Van Jorks, E. Gjonaj and T. Weiland, "Eddy current analysis of a PWM controlled induction machine," *COMPEL: The International Journal for Computation and Mathematics in Electrical and Electronic Engineering,* 2013.

[105] L. Hanisch, M. Sun and M. Henke, "Novel Modeling Approach for Voltage Distribution within Automotive Electrical Machines," in *2020 International Conference on Electrical Machines (ICEM)*, 2020.

[106] Y. Ryu, M. Yea, J. Kim and K. J. Han, "Stator Impedance Modeling Platform for the Electromagnetic Compatibility Aware Design of 3.7-to 7.5-KW Squirrel-Cage Induction Motors," *IEEE Transactions on Industrial Electronics,* vol. 68, p. 11255–11265, 2020.

[107] C. R. Paul, Analysis of multiconductor transmission lines, John Wiley & Sons, 2007.

[108] E. Bjerkan, "High Frequency Modeling of Power Transformers. Stresses and Diagnostics," 2005.

[109] N. Idir, Y. Weens and J.-J. Franchaud, "Skin effect and dielectric loss models of power cables," *IEEE Transactions on Dielectrics and Electrical Insulation,* vol. 16, p. 147–154, 2009.

[110] W. B. Westphal and A. Sils, Dielectric constant and loss data, vol. 72, Air Force Materials Laboratory, Air Force Systems Command, 1972.

[111] Y. Ryu and K. J. Han, "Improved transmission line model of the stator winding structure of an AC motor considering high-frequency conductor and dielectric effects," in *2017 IEEE International Electric Machines and Drives Conference (IEMDC)*, 2017.

[112] Z. Huang, A. Reinap and M. Alaküla, "Dielectric properties modeling and measurement of single tooth coil insulation system under accelerated degradation test," in *2016 XXII International Conference on Electrical Machines (ICEM)*, 2016.

[113] T. Guillod, R. Färber, F. Krismer, C. M. Franck and J. W. Kolar, "Computation and analysis of dielectric losses in MV power electronic converter insulation," in *2016 IEEE Energy Conversion Congress and Exposition (ECCE)*, 2016.

[114] D. Meeker, "Finite element method magnetics," *FEMM,* vol. 4, p. 162, 2010.

[115] J. Adabi, F. Zare, G. Ledwich and A. Ghosh, "Leakage current and common mode voltage issues in modern AC drive systems," in *2007 Australasian Universities Power Engineering Conference*, 2007.

167

[116] B. Ellis and R. Smith, Polymers: a property database, CRC press, 2008.

[117] J. Lammeraner and M. Štafl, Eddy currents, CRC Press, 1966.

[118] Q. Tang, Investigation of magnetic properties of electrical steel and transformer core at high flux densities, The University of Manchester (United Kingdom), 2015.

[119] D. Roger, E. Napieralska-Juszczak and A. Henneton, "High frequency extension of non-linear models of laminated cores," *COMPEL-The international journal for computation and mathematics in electrical and electronic engineering,* 2006.

[120] A. B. Surahammars Burks, "M330-50A data sheet," 2009.

[121] G. Amorese, "LCR/impedance measurement basics," in *1997 Back to Basics Seminar, HEWLETT PACKARD (HP)*, 1997.

[122] *Impedance measurement handbook,* Keysight Technologies, 2015.

[123] "Agilent 4294A Precision Impedance Analyzer, Operation Manual," 2003.

[124] "Keysight 16048G/H Test Leads, operation and service manual," 2015.

[125] "Keysight Technologies, Accessories Catalog for Impedance Measurements," 2015.

[126] "BK precision 894/895, 500kHz/1MHz LCR Meter, User manual," 2017.

LIST OF FIGURES

171

172

174

175

LIST OF TABLES

176

APPENDICES

Appendix A. SPICE netlist example and syntax

This appendix is intended to exemplify the SPICE netlists with frequency dependent impedances. The main content of the netlist implementation and the development of the utilized formulation can be found in Chapter 3, Sections 3.3.1 and 3.3.2. *Fig. A-0-1* shows the different syntax for the elements forming the equivalent circuit. A netlist example for the DM connection of the e-ACC machine is described below.

Fig. A-0-1 – SPICE syntax for netlist implementation

Netlist example

```
I1 N001 N002 AC 1 0 %Current Injection for the DM mode (between nodes 1-2)
G1 N005 N001 N005 N001
laplace=1/((8.9092e08*((abs(S)/6.2831)^0.95657)+(0.001))+((1.1147e06*(abs(S)
/6.2831)^0.90697+(0.0014734))*sqrt(-1))) %Self-impedance C1
C11 N001 0 1.7634e-12
C12 N032 0 1.7634e-12 % Ground capacitances in pi-equivalent circuit
R1 N001 N005 10000000000 % Infinitely large parallel resistance
B3-1 N005 N006 V=I(B1-3)*1
laplace=(2.7e08*((abs(S)/6.2831)^1.0242)+(0.001))+((8.8396e07*(abs(S)/6.2831
)^0.91692+(0.0010587))*sqrt(-1)) %Mutual impedance between conductors 1-3
B5-1 N006 N007 V=I(B1-5)*1
laplace=(1.0632e08*((abs(S)/6.2831)^1.0775)+(0.001))+((7.8956e07*(abs(S)/6.2
831)^0.9207+(0.00054746))*sqrt(-1)) %Mutual impedance between conductors 1-5
B7-1 N007 N008 V=I(B1-7)*1
laplace=(4.5132e09*((abs(S)/6.2831)^1.127)+(0.00099999))+((6.9341e-
07*(abs(S)/6.2831)^0.92639+(0.00028425))*sqrt(-1))
.
.
.
B55-1 N031 N032 V=I(B1-55)*1
laplace=(5.4682e-09*((abs(S)/6.2831)^1.1139)+(0.00099946))+((5.9546e-
07*(abs(S)/6.2831)^0.93609+(0.00045126))*sqrt(-1))
C1-3 N001 N060 3.348e-12 %Mutual capacitance between conductors 1-3
C1-5 N001 N116 2.6917e-15 %Mutual capacitance between conductors 1-5
C1-7 N001 N172 3.9442e-17
.
.
.
C1-55 N001 N1516 7.3959e-23
G2 N033 N032 N033 N032 %New conductor, condurctor 2
laplace=1/((8.5872e08*((abs(S)/6.2831)^0.95884)+(0.001))+((1.1082e-
06*(abs(S)/6.2831)^0.90754+(0.0014645))*sqrt(-1)))
C21 N032 0 1.8108e-12
C22 N060 0 1.8108e-12
R2 N032 N033 10000000000
.
.
.
B52-56 N1570 N1571 V=I(B56-52)*1
laplace=(9.7432e-09*((abs(S)/6.2831)^1.0827)+(0.001))+((7.3472e-
07*(abs(S)/6.2831)^0.92627+(0.00067))*sqrt(-1))
B54-56 N1571 N1572 V=I(B56-54)*1
laplace=(2.5427e-08*((abs(S)/6.2831)^1.0229)+(0.00099965))+((7.5603e-
07*(abs(S)/6.2831)^0.92623+(0.00074424))*sqrt(-1))
C_ph1-ph_5 N001 N002 3.0641e-12 %Inter-phase lumped capacitance
B_ph5-ph_1 N1572 N1573 V=I(B227-225)*1 %Inter-phase lumped impedance
laplace=1/((2.3917e-11*((abs(S)/6.2831)^3.4094)+(0.13851))+((6.9417e-
12*(abs(S)/6.2831)^3.6966+(0.19927))*sqrt(-1)))
G57 N1574 N1573 N1574 N1573 %Beggining of coil 2, conductor 57
laplace=1/((8.9092e-08*((abs(S)/6.2831)^0.95657)+(0.001))+((1.1147e-
06*(abs(S)/6.2831)^0.90697+(0.0014734))*sqrt(-1)))
C571 N1573 0 1.7634e-12
C572 N1601 0 1.7634e-12
.
.
.
B220-224 N6277 N6278 V=I(B224-220)*1
```

180

```
laplace=(9.7432e-09*((abs(S)/6.2831)^1.0827)+(0.001))+((7.3472e-
07*(abs(S)/6.2831)^0.92627+(0.00067))*sqrt(-1))
B222-224 N6278 N6279 V=I(B224-222)*1
laplace=(2.5427e-08*((abs(S)/6.2831)^1.0229)+(0.00099965))+((7.5603e-
07*(abs(S)/6.2831)^0.92623+(0.00074424))*sqrt(-1))
C_ph4-ph_8 N4711 N10987 3.0641e-12
B_ph8-ph_4 N6279 N6280 V=I(B395-393)*1
laplace=1/((2.3917e-11*((abs(S)/6.2831)^3.4094)+(0.13851))+((6.9417e-
12*(abs(S)/6.2831)^3.6966+(0.19927))*sqrt(-1)))
G225 N6281 N002 N6281 N002 %New phase connected to N002, cond. 225
laplace=1/((8.9092e-08*((abs(S)/6.2831)^0.95657)+(0.001))+((1.1147e-
06*(abs(S)/6.2831)^0.90697+(0.0014734))*sqrt(-1)))
C2251 N002 0 1.7634e-12
C2252 N6308 0 1.7634e-12
.
.
.
B446-448 N12554 N12555 V=I(B448-446)*1
laplace=(2.5427e-08*((abs(S)/6.2831)^1.0229)+(0.00099965))+((7.5603e-
07*(abs(S)/6.2831)^0.92623+(0.00074424))*sqrt(-1))
C_ph8-ph_12 N10987 N17263 3.0641e-12
B_ph12-ph_8 N12555 N6280 V=I(B619-617)*1
laplace=1/((2.3917e-11*((abs(S)/6.2831)^3.4094)+(0.13851))+((6.9417e-
12*(abs(S)/6.2831)^3.6966+(0.19927))*sqrt(-1)))
G449 N12556 N003 N12556 N003 %New phase connected to N003, cond 449
laplace=1/((8.9092e-08*((abs(S)/6.2831)^0.95657)+(0.001))+((1.1147e-
06*(abs(S)/6.2831)^0.90697+(0.0014734))*sqrt(-1)))
C4491 N003 0 1.7634e-12
C4492 N12583 0 1.7634e-12
.
.
.
B668-672 N18828 N18829 V=I(B672-668)*1
laplace=(9.7432e-09*((abs(S)/6.2831)^1.0827)+(0.001))+((7.3472e-
07*(abs(S)/6.2831)^0.92627+(0.00067))*sqrt(-1))
B670-672 N18829 N18830 V=I(B672-670)*1 %Total number of nodes:18830
laplace=(2.5427e-08*((abs(S)/6.2831)^1.0229)+(0.00099965))+((7.5603e-
07*(abs(S)/6.2831)^0.92623+(0.00074424))*sqrt(-1))
C_ph12-ph_1 N17263 N001 3.0641e-12
B_ph1-ph_12 N18830 N6280 V=I(B3-1)*1
laplace=1/((2.3917e-11*((abs(S)/6.2831)^3.4094)+(0.13851))+((6.9417e-
12*(abs(S)/6.2831)^3.6966+(0.19927))*sqrt(-1)))
.ac dec 100 10000 10000000 %.ac analysis with 100 points per decade between
.options topologycheck=0     10000 Hz and 10000000Hz
.save V(N001) %Saving value of the input voltage in node N001
.backanno
.end %end command
```

181

LIST OF PUBLICATIONS

Indexed conference proceedings

1. Sarrió, J. E. R., Ciceo, S., Martis, C., & Chauvicourt, F. (2019, October). Comparative study between PMSM models used for NVH system-level simulation. In 2019 Electric Vehicles International Conference (EV) (pp. 1-5). IEEE.

2. Sarrió, J. E. R., Martis, C., & Chauvicourt, F. (2020, October). Numerical computation of parasitic slot capacitances in electrical machines. In 2020 International Conference and Exposition on Electrical And Power Engineering (EPE) (pp. 146-150). IEEE.

3. Ruiz-Sarrió, J. E., Chauvicourt, F., Gyselinck, J., & Martis, C. (2021, May). High-Frequency Modelling of Electrical Machine Windings Using Numerical Methods. In 2021 IEEE International Electric Machines & Drives Conference (IEMDC) (pp. 1-7). IEEE.

4. Ruiz-Sarrió, J. E., Chauvicourt, F., & Martis, C. (2022, March). Sensitivity Analysis of a Numerical High-Frequency Impedance Model for Rotating Electrical Machines, ICEM2022, Valencia, Spain, (*Accepted for oral presentation. May 30, 2022*)

Indexed journals

5. Ruiz-Sarrió, J. E., Chauvicourt, F., Gyselinck, J., & Martis, C. (2021, December). Impedance Modelling Oriented Towards the Early Prediction of High-Frequency Response for Permanent Magnet Synchronous Machines, IEEE Transactions on Industrial Electronics, (*Accepted for final publication, June 18, 2022*)